MASTER THESIS

FATIGUE IN CAST METALS

A GENERALIZED ALGORITHM FOR MULTIAXIAL LOADING

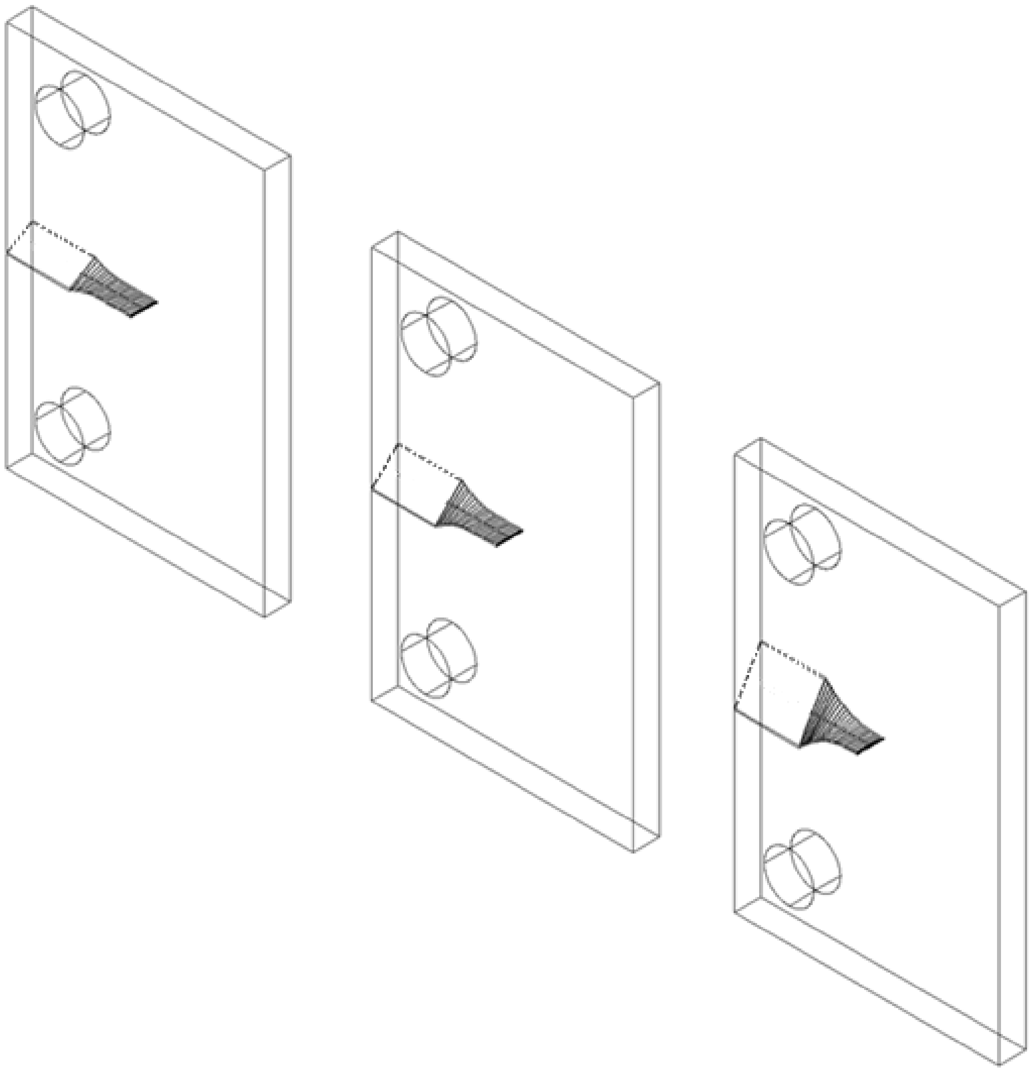

BM4-1

Erik Bouvin Pedersen & Morten Eggert Nielsen
M.Sc. in Structural and Civil Engineering
Aalborg University Esbjerg
4. August 2014

AALBORG UNIVERSITY
STUDENT REPORT

Aalborg University Esbjerg
Niels Bohrs Vej 8
6700 Esbjerg

Title:
Fatigue in cast metals - A generalized algorithm for multiaxial loading

Synopsis:

A fatigue crack growth algorithm for multiaxial variable loading was proposed.
Crack growth models Paris' law, Forman eq. and NASGRO was evaluated relatively to each other. For the tested case studies Paris' law was preferred.
Test and validation of numerically determined $K_I$magnitdues. In both 2D and 3D the accuracy was within 2% of analytical solutions.
In a case study of a plane problem, the crack propagation criterion of Richard was proven to be equal, to the maximum tangential stress criterion.
Numerical mixed mode I+II crack direction, showed fluactuating results, whereas the numerical mixed mode I+III showed good results.
Finally, a case study of mode I+III crack growth, led to too conservative results.
The deviations noticed in the crack direction case studies, may haven been caused by inaccurate K_{II} magnitudes.
The fatigue crack growth deviations were expected to show too conservative crack growth rates, because plasticity induced crack closure was not implemented.

Project period:
3-2-2014 - 4-8-2014

Project group:
Group BM4-1

Members:
Erik Bouvin Pedersen
Morten Eggert Nielsen

Supervisor:
Lars Damkilde

Assistant Supervisor:
Ronnie Refstrup Pedersen

No. printed Copies: 3

No. of Pages: 107

No. of Appendix Pages: 3

Total no. of pages: 110

Table Of Contents

0.1 Preface

The thesis work was carried out as a part of the M.Sc. in Structural and Civil Engineering at Aalborg University Esbjerg, under supervision of Prof. L. Damkilde.

The reader is assumed to have basic knowledge within the fields of continuum mechanics, fracture mechanics and finite element method.

References are made by **[Author]** and in the PDF version, it is linking to the position within the bibliography.

The attached DVD include the following:

- Matlab codes
  - Computational framework for fatigue crack growth algorithm
  - Fatigue crack growth addon for variable amplitude cycle counting
- ANSYS
  - APDL
    - Numerical validation of stress intensity factors
  - Workbench
    - Crack tip plastic zone analysis (Elastic-plastic analysis)
    - Transformation matrix (A method for determining the transfer function)
- Appendix - Script

Erik Bouvin Pedersen ______________________________

Morten Eggert Nielsen ______________________________

Introduction 1

1.1 Problem description

During the latest decades, offshore wind energy has been a main topic within the renewable energy section. Offshore wind energy is one of the most expensive, based on the levelized cost of energy.

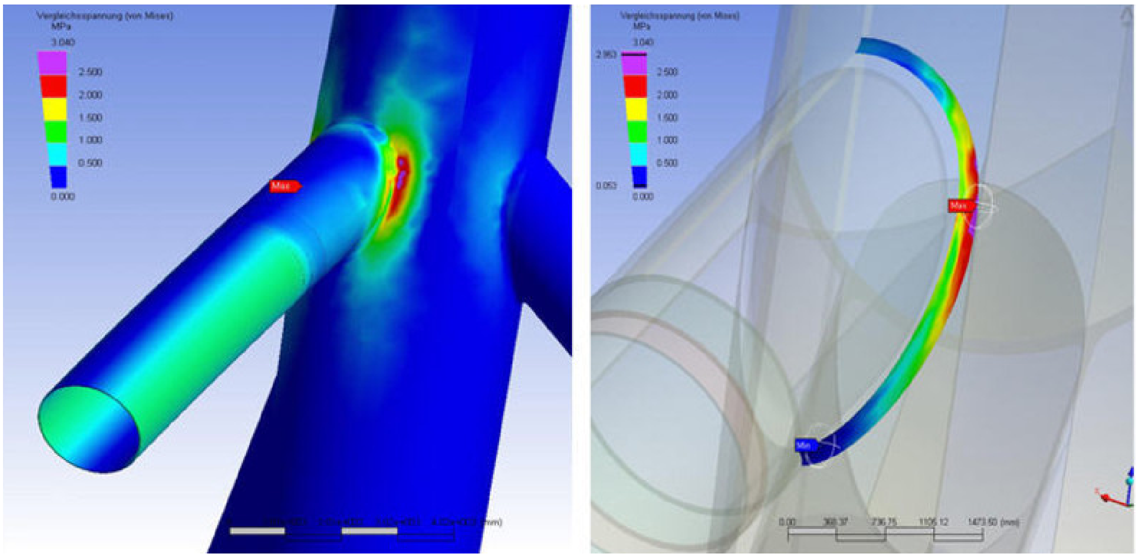

Figure 1.1. Optimization of stress gradients in cast nodes in comparison to welded nodes.

In search for cost-efficiency, the offshore structures are innovatively revised by the designers, trying to develop new cost optimized designs. Therefore, advantages and opportunities, related to cast members, are of great interest to the industry. This may offer possibilities of new methods for manufacturing and commissioning.

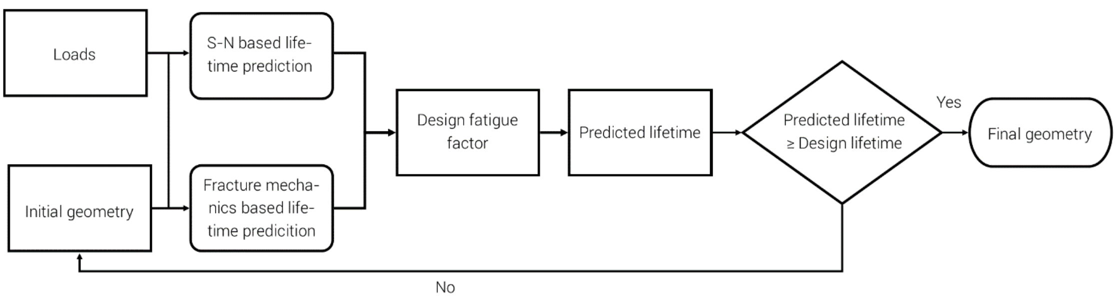

Figure 1.2. Fatigue limit state design verification process based on either S-N curves or fracture mechanics.

Certifying bodies, e.g. DNV, allow for the use of fracture mechanics instead of S-N based lifetime prediction, as sketched in figure 1.2. [DNV-RP-C203]

As casting defects are an inherent part of cast components, the crack initiation may assumed to be over, making fracture mechanics analyses preferable over the S-N method.

Hence, this thesis investigates and tests the possibilities within fatigue analysis based on linear-elastic fracture mechanics, in a generalized loading environment. For this, a general algorithm for lifetime estimation of multiaxially variable loaded cast metals is proposed and tested.

1.2 Literature review

The key references for the thesis are listed below:

- Crack growth models
  Three different crack growth models are tested and evaluated in relation to each other. The three models are Paris' law [M.P.Gomez & E.Anderson 1961] , Forman equation [E.Kearney & Engle 1967] and the NASGRO [G. & R. 1992].

- Crack propagation direction
  The plane maximum tangential stress criterion proposed by Erdogan and Sih [F. Erdogan 1963] is tested relatively to the three-dimensional criterion of Richard [H.A. Richard M. Fulland 2005].

- Mixed mode fracture and fatigue crack growth
  The fracture criterion of Richard is used to define an equivalent mode I stress intensity factor.

- Case study: mixed mode I + II [M 1990]
  A simply supported, centrally loaded beam, with different initial edge cracks positioned away from the beam center. The off center crack position induces mixed mode I + II behaviour.

- Case study mixed mode I + III [Omidvar 2013]
  A numerical and experimental study of fatigue crack growth under mixed mode I + III loading of a modified CT specimens with inclined initial edge cracks. The inclinations induce mixed mode I + III behaviour.

1.3 Thesis objectives

Based on linear-elastic fracture mechanics, a generalized algorithm for lifetime estimations of multiaxially variable loaded cast metal components is proposed. The proposed algorithm is schematized in figure 1.3.

The thesis objectives are outlined below:

- Consider important aspects in relation to cast metals and discuss methods for assesment of acceptable casting defects and initial cracks.
- Consider important theoretical aspects of linear-elastic fracture mechanics
- Test the influence of mean stress level using appropriate crack growth models
- Test and validate a numerical method for calculating stress intensity factors for various cracks
- Test and evaluate crack propagation direction criterions
- Test and evaluate mixed mode fracture criterions
- Test and evaluate mixed mode fatigue crack growth

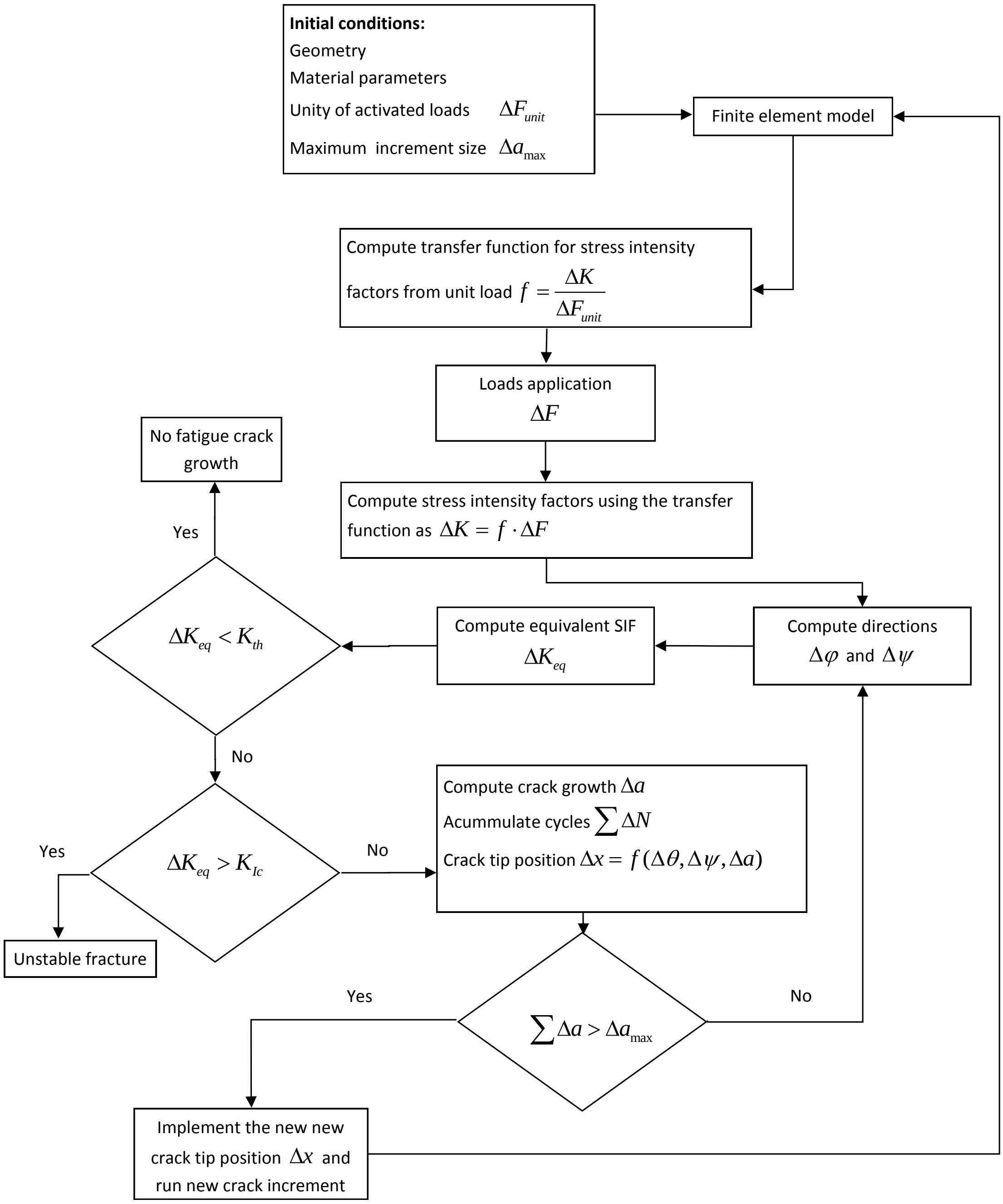

Figure 1.3. Proposed generalized algorithm for multiaxial loading.

Cast metals - Failure and defects 2

2.1 Cast metals and material properties

Cast metal is a generic term covering metals such as iron, steel and aluminum. Cast iron and cast steel are promising material in offshore structures, as they have desirable material properties and costs. Cast iron and cast steel are broad terms, which cover many materials. Cast iron has a carbon content above 2% where cast steel has a carbon content below 2%. The materials are similar, but have distinctive mechanical properties. This section will explain the primary characteristics and differences between cast irons and cast steels.

Production characteristics

Cast iron generally has 30% to 40% lower production cost compared to cast steel. The lower cost has origin in lower melting temperatures, better machinability and lower shrinkage. The melting point of cast iron is $300° - 350°$ lower than cast steel, which reduces cost in the melting process. The high carbon content in cast iron act lubricating, making cast iron more wear resistant, making cast iron more machinable. The high carbon content also reduces shrinkage giving shrinkage of about 1% compared to 4% of cast steel. The lower shrinkage makes precision casting a simpler process. The high carbon content is not purely positive for production characteristics, as it decreases the weldability of cast iron compared to cast steel.

Mechanical characteristics

Cast iron has better vibration damping than cast steel, which is desirable in dynamically loaded structures. Cast iron has, as previously mentioned, high content of free carbon. The high carbon content leads to lower fatigue performance, fracture toughness and ductility.

The effect of carbon on the fatigue performance varies greatly among different types of cast iron, as illustrated on figure 2.1.

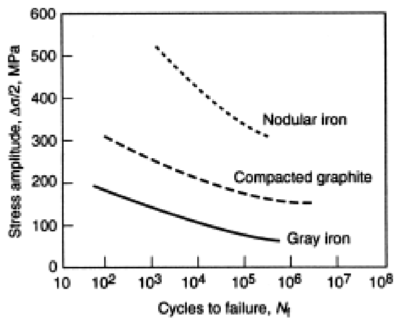

Figure 2.1. Fatigue performance of different types of cast iron.

The differences of fatigue performance can be explained by studying the microstructure of different types of cast iron. The microstructure of cast irons is illustrated on figure 2.2.

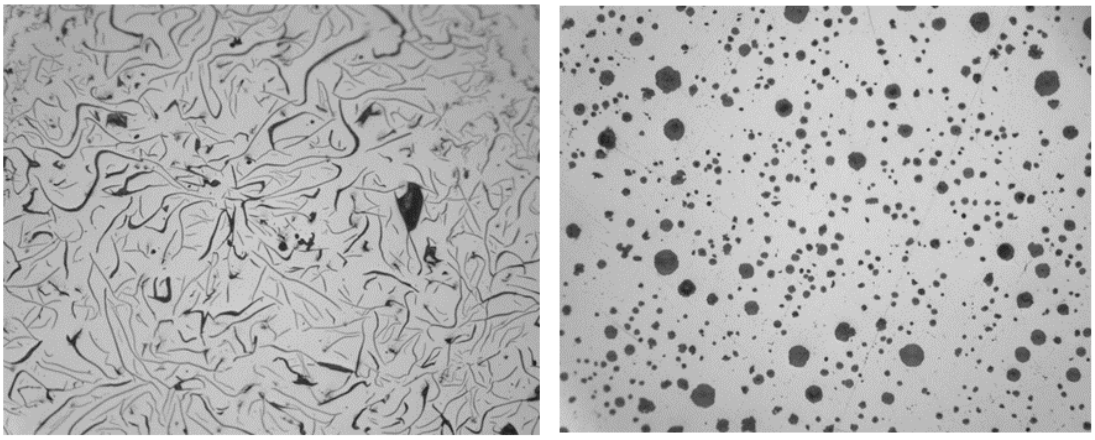

Figure 2.2. Microstructure of gray iron(left) and nodular iron(right).

From figure 2.2 it can be seen that for grey cast iron the carbon accumulates in large flakes, where nodular iron it gathers into small spheres. The large flakes acts as notches and decrease the fatigue performance and fracture toughness. The large flakes also make grey iron less notch sensitive. Even though gray iron has lower fracture toughness, it does not decrease with temperature, which is illustrated on figure 2.3.

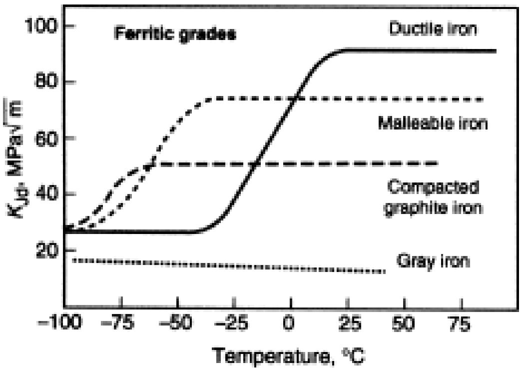

Figure 2.3. Fracture toughness varying with temperature.

The ductility also varies among different types of cast iron, gray iron has Charpy V-notch energy between 1-6 J where ductile iron has between 14-24 J.

Cast iron and cast steel are also affected differently by loading. Retarding effects, which are desirable in fatigue, have been observed in cast steels when subjected to overloads. This is not observed to the same extend in cast iron.[Biermann 2007]

2.2 Crack growth and fracture mechanisms in metals

In this thesis, the emphasized failure mechanism is fracture, caused by fatigue crack growth. Relevant fracture mechanical aspects are briefly presented.

The fracture may act ductile or brittle depending on the material, geometry and loading. Ahead of fracture, crack growth may be present, leading to change in geometry and thereby change in capacity.

In the following the concept of crack growth mechanisms are introduced along with mechanical descriptions of fracture mechanisms.

2.2.1 Crack growth mechanisms

Several crack growth mechanisms are able to occur in cast metallic structures. The main focus in this thesis is fatigue crack growth, why only attention is paid to this concept.

2.2.1.1 Fatigue

Repetitive loading of initial flawed/cracked members may lead to failure. At stress levels far below the ultimate material strength the crack may initiate, and by stable fracture, grow into a considerable size. Over time the crack may cause failure induced by unstable fracture. The concept of fatigue crack growth is seen in figure 2.4.

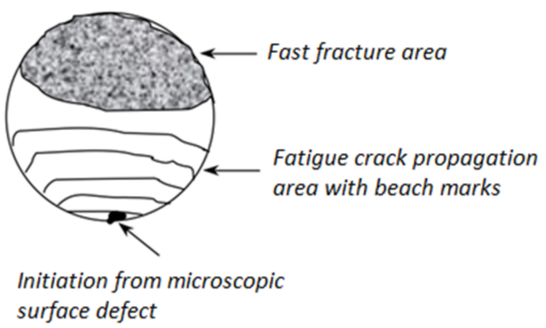

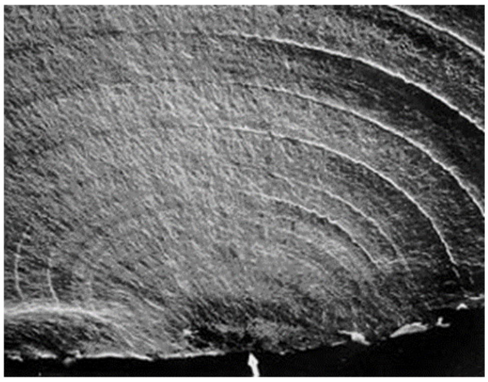

Figure 2.4. Macroscopic fracture surface characterics: crack initiation, fatigue crack growth (with beach marks induced by noncontinuous loading) and lastly fast fracture(either ductile or brittle).

The three different situations, stated in figure 2.4, is often referred to as region I (crack initiation), II(stable fracture) and III(unstable fracture), an is the governing mechanisms considered in this thesis.

Fatigue cracks in cast metals, may initiate at the surface where stress concentrations exist due to rapid changes in geometry or surface flaws, but can also initiate within a member due to e.g. inclusions or porosities. [Maahn 2009] Dealing with relatively large casted components flaws of a size, which can be found by NDT methods(0.05-0.5mm), is reasonable to assume, as they often exist in several locations at/within the component. [Maahn 2009] Usually cracks initiates as a shear fracture with a direction of 45° with the maximum principal stress direction, but directs towards 90°.

As the crack reaches a considerable size, the crack grows by stable fracture. The crack growth depends on number of applied load cycles and crack growth rate, where the crack growth rate is a function of material, amplitude and stress level. The direction of crack growth is still approximately perpendicular to the maximum prinpical stress.[Maahn 2009]

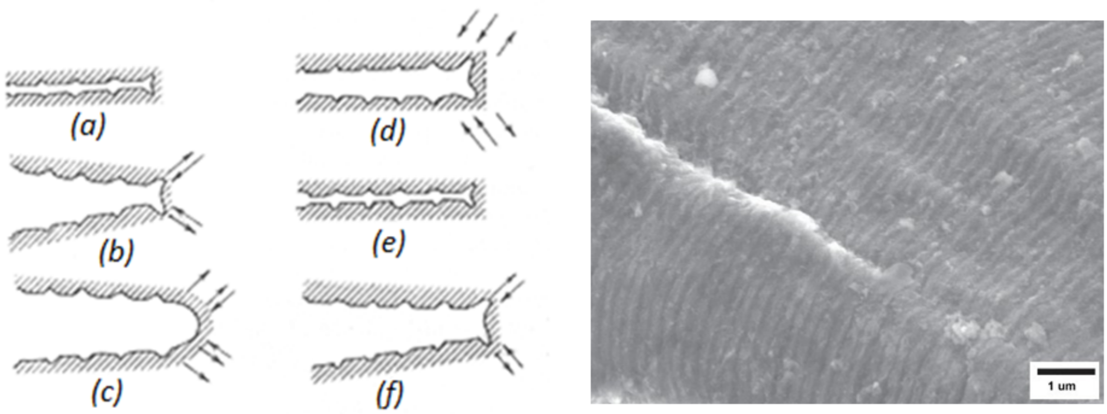

Figure 2.5. Fatigue crack growth may induce striations, due to the shear slip planes at the crack-tip. The generation of striations is illustrated in steps from a to f.

Microscopic parallel lines, called striations(see figure 2.5), may develop e.g. in between the beach marks in figure 2.4. At every load cycle a new striation is developed. The distance between the striations is a measure of the crack growth rate, if load cycle periods are known. The distinction of striations, increase with deformation capacity of the fatigue loaded material.

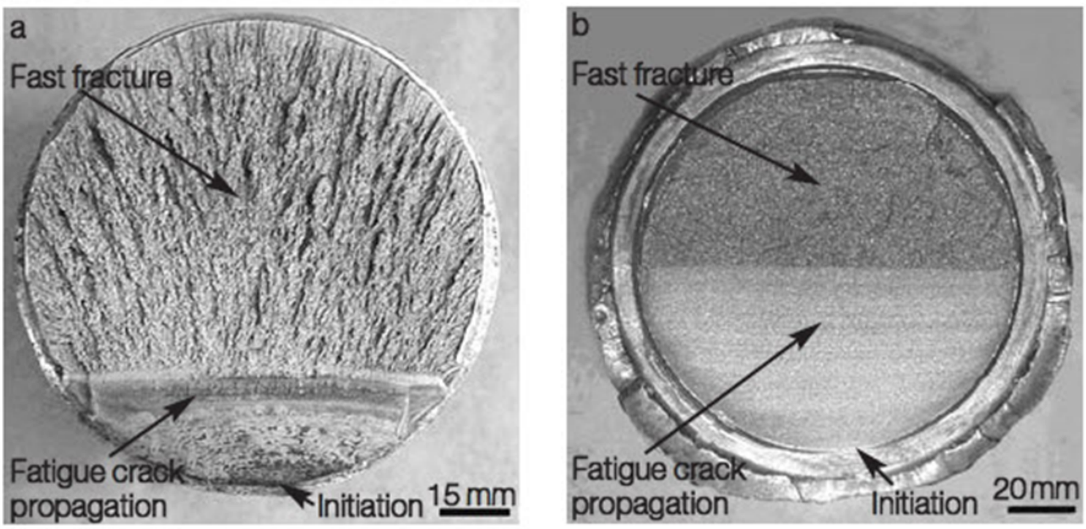

Figure 2.6. Fatigue crack propagation for a) high and b) low applied stress level.

At a point the crack reaches a critical size, where unstable fracture begins, which inevitable fails by a fast final fracture. The fracture mechanism of the final fracture is governed by the level of stresses and is illustrated in figure 2.6. At high stress levels (a), the specimen fails by fracture after relatively short fatigue crack growth. At low stress levels (b), the specimen fails by fracture after relatively long fatigue crack growth. Dependent on the ultimate yield strength, and fracture toughness of the remaining material, the final fracture will either be ductile or brittle.

The brittle and ductile fracture mechanisms are introduced in the following section.

2.2.2 Fracture mechanisms

As explained previously, failure may occur due to ductile or brittle fracture. Both fracture mechnisms can be either transgranular or intergranular. The main focus is to describe the transgranular fracture mechanisms, as the stable fracture may be described as a form of incremental transgranular brittle fracture.

2.2.2.1 Ductile fracture

Ductile fracture only occur for ductile materials. The ductility enables redistribution of localized stress and do not introduce any immediate critical effect because of plastic deformation and hardening. Hence, the energy is consumed in the area of localized stresses, i.e. at a crack-tip.

The two types of ductile fracture is presented in individual sections, where transgranular ductile fracture is emphasized.

Transgranular ductile fracture

The development of ductile fracture is illustrated in figure 2.7 along with a fractography of a ductile fracture surface. At the fractography dimples are noticed and even inclusions within the dimples may be present. The dimpled fracture surface is a microscopic characteristic of ductile fractures.

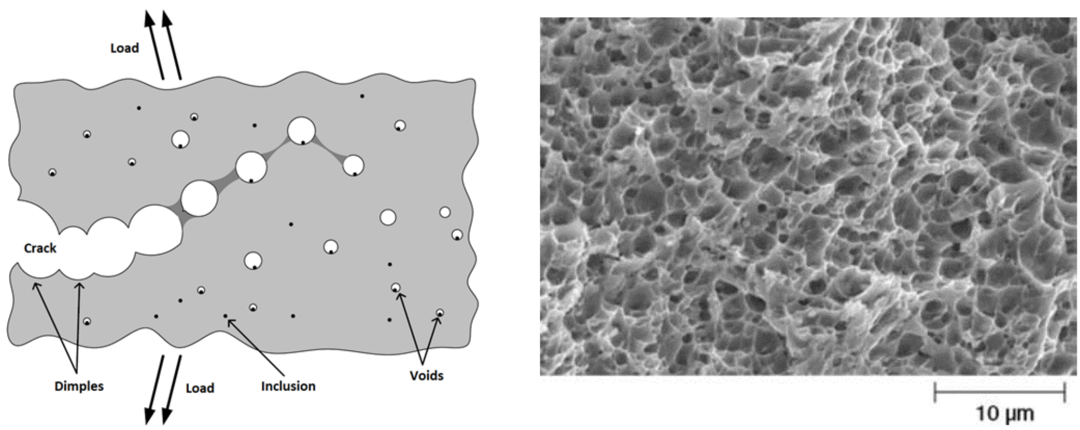

Figure 2.7. Ductile fracture mechanism and fractography of ductile fractured low-alloy steel casting.[International 2009]

The ductile fracture may be described in the following steps:

1. Void nucleation (debonding of inclusions and matrix material)
2. Void growth
3. Matrix necking
4. Relatively large final fracture

The voids are generated because of the debonding between included particles and the matrix material. Growth of the voids, caused by decreased effective area between voids, leads to necking of the matrix material. In the end the effective area is fully yielding and fractures at 45° against the load direction.

Intergranular ductile fracture

At relative high temperatures the grain boundaries become weaker than the actual grains. Thus, at relative high temperatures grain boundaries, and especially if skewed 45° in relation to the loading direction, intergranular creep can occur. This may in the end lead to intergranular ductile fracture.

2.2.2.2 Brittle fracture

As for ductile fractures, brittle fracture can occur transgranular or intergranular. Brittle fracture occur by cleavage of the grains(transgranular) or in between the grains(intergranular).

Brittle intergranular fracture

The transgranular cleavage propagates grainwise through preferred crystalographic planes, which not neccesarily is equal to the slip planes. At each grain boundary, the propagation direction is redirected based on the new preferred crystalographic plane, which is illustrated in figure 2.8.

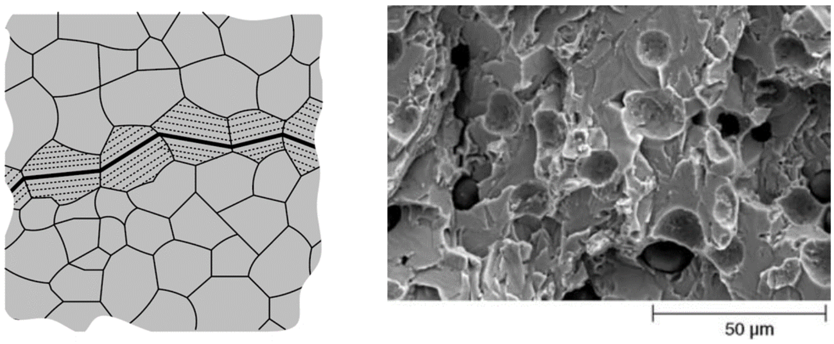

Figure 2.8. Brittle transgranular fracture path (full line), preferred crystalographic planes (dotted lines) and fractography of ductile iron, exposed to transgranular brittle fracture.[International 2009]

In modeling of crack simulation, the grains preferred crystalographic planes are not explicitly needed. As the grain size of cast metals are significantly smaller than the component dimensions, the governing direction is approximately perpendicular to the maximum principal stress direction.

Brittle intergranular fracture

Brittle intergranular fracture can occur if the cast metal is improperly heat treated and film of brittle material components may arise. However, this is a rather rare event.

2.3 Casting defects and residual stresses

Casting defects are a complex and component individual problem. Today's manufacturers have the capabilities of casting components in quality almost equal to non-cast components.[International 2009] However, the quality is inevitably connected to the manufacturing costs, why casting defects are often accepted in order to obtain the most cost-effective casting.

In practice the level and types of accepted casting defects are stated explicitly in a contract, in relation to a known society's casting defect classification, as illustrated in figure 2.3.

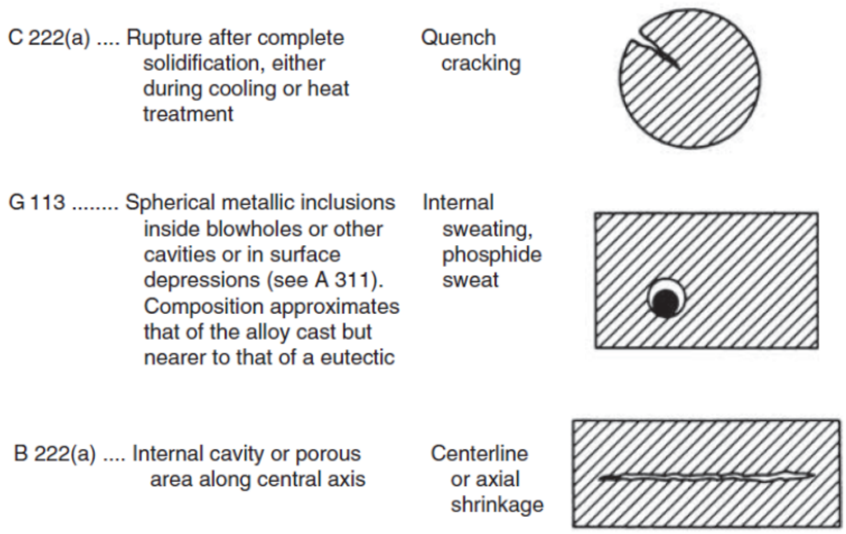

Because of the present casting defects casted components must not only be designed properly in accordance to structural requirements, but also the accepted casting defects.

In addition to casting defects, residual stresses also effect the fatigue strength of casted components. Omitting the residual tensile stresses in lifetime predictions, lead to non-conservative results. Thus, residual stresses, and how the component's load spectrum effects these, is also important to include in the design considerations.

Beside theoretical and practical knowledge about casting procedures, numerical methods are available for simulation of castings. By this any given cast geometry may be tested and evaluated for the most severe defects.

Method for defining acceptable casting defects

The possibility of influencing casting defects, in a favorable manner, should be considered previous to the manufacturing of the casted component/member. A combination of important aspects should be considered, in order to find the most cost-efficient acceptable casting defects, expressed as an inital crack. In figure 2.9 the most important considerations are illustrated.

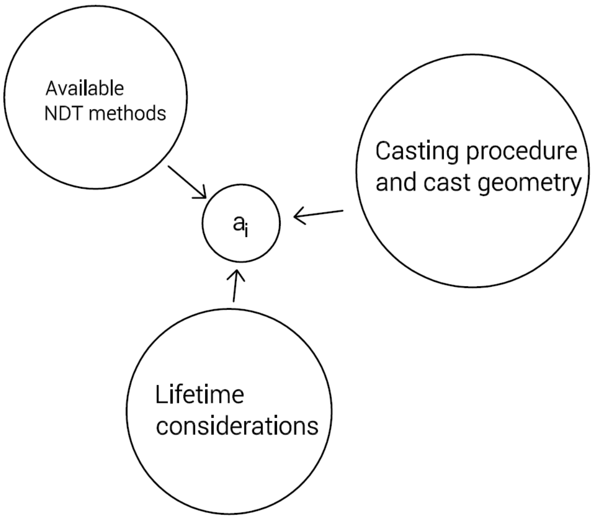

Figure 2.9. Important considerations regarding the accepted casting defects.

Available NDT methods

Casting defects may be interpreted as initial cracks of a size equal to the accepted, or assumed equal to the size possible to find by non-destructive testing (NDT) methods. This size is often between 0.05-0.5mm [Maahn 2009].

Casting procedure and cast geometry

In collaboration with manufacturers, the quality capabilities and expected difficulties must be clarified in relation to casting of a given geometry.

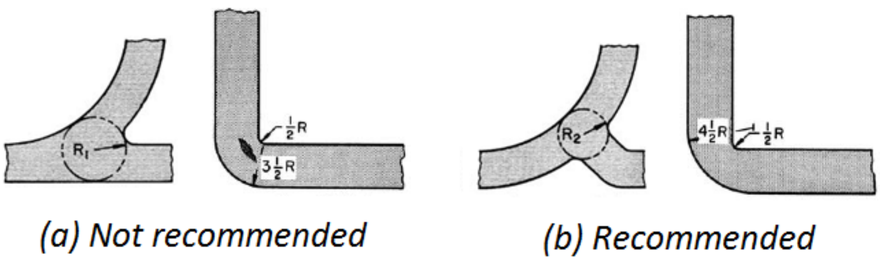

Figure 2.10. Design recommendations - Revised T- to Y-junctions which reduce mass by 26% and improvement of L-junction design in relation to casting defects. [International 2009]

In order to evaluate the most cost-efficient solution, geometry specific advantages must be discussed with an expert, in relation to the structural requirements.

Lifetime considerations

The structural designer must verify that the casted component/member has the capacity to fulfill its structural requirements. The structural verification principle either follow the fail safe or the safe life principle.

In structural components where the fail safe principle is not applicable, the safe fail principle is applied. In corrosive environments safe, as offshore, either scheduled NDT inspections, replacements on regular basis or design for unlimited lifetime may be considered.

In order to schedule the NDT inspections, replacements or even design for unlimited lifetime, the impact of the accepted casting defects must be considered. Based on fracture mechanics and the structural lifetime requirements, an theoretical acceptable crack may be determined.

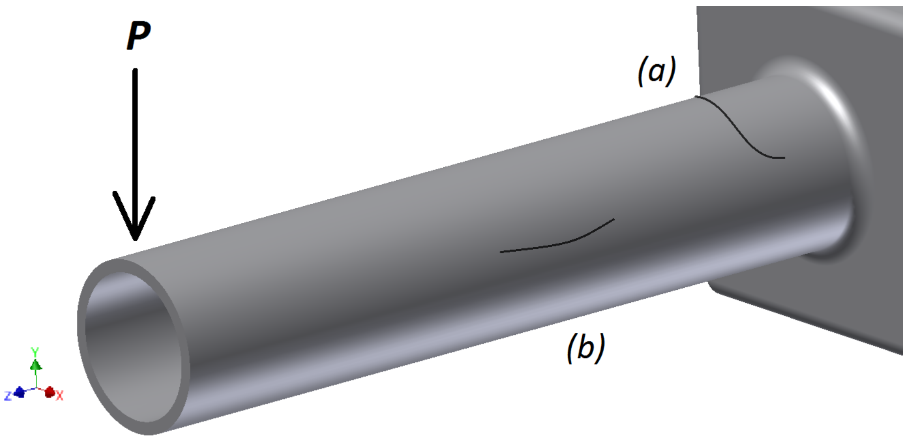

Figure 2.11. The importance of the defect shape, location and orientation in a fracture mechanical analysis. For the cantilever beamwith almost equal crack lengths, crack (a) is more critical than (b), due to its location and orientation.

As illustrated in figure 2.11, important geometrical defect parameters are needed in order to carry out the analyses based on fracture mechanics.

Next to the structural principle, obviously the cast component fatigue life should be balanced in relation to adjacent structural components. Different methods have been suggested for balanced fatigue life methods in relation to casted joints in offshore structures [Dong & Li 2013].

Initial crack

An structural and economical optimum for the accepted initial crack should be determined based on the considerations stated above and illustrated in figure 2.9.

Linear-elastic fracture mechanics 3

3.1 Application of linear-elastic fracture mechancis

Stress/strain-based approaches and fracture mechanics have been proposed for estimation of structural fatigue life behavior. For structures containing flaws/cracks fracture mechanics has its advantages. As described thoroughly in 2.3 cast metals contain casting defects. Hence, a fracture mechanical approach is emphasized in this thesis. In fracture mechanics there are two primary methods; linear-elastic fracture mechanics (LEFM) and elastic-plastic fracture mechanics (EPFM). In figure 3.1 the scope of LEFM and EPFM is schematized.

In the early days of fracture mechanics, it was only intended for brittle materials. However, as knowledge about fracture was developed, fracture mechanics became applicable for ductile materials too. In appropriate circumstances ductile materials also exhibit brittle fracture. Hence, as knowledge about fracture was developed, fracture mechanics became applicable for ductile material under linear-elastic as well elasto-plastic conditions.

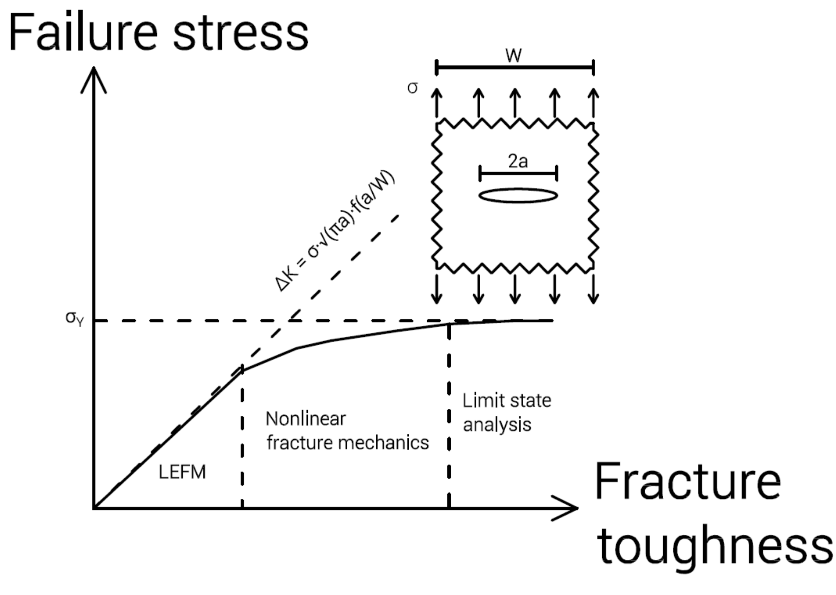

Figure 3.1. An example of application regions of LEFM for a fracture problem. [Anderson 2005]

Materials with relatively low fracture toughness, loaded primarily in the linear-elastic region ($\sigma < 0.8\sigma_Y$), are well suited for LEFM (Figure 3.1). Material with intermediate fracture toughness which experiences plasticity violates the assumption of LEFM and EPFM is better suited.

Materials with high fracture toughness are not suited for fracture mechanics while they exhibit very ductile failure mechanisms and a simple limit load analysis is sufficient.

The focus of this thesis is cast iron/steel structures exposed to high cycle fatigue loading for which the working stress is far below the yield stress the vast majority of the time. Hence, by looking at figure 3.1 LEFM shows to be applicable for the investigated problem in this thesis.

3.2 Energy approach

In strength or fatigue analysis of structures containing flaws, the application of fracture mechanics is often required. Fracture mechanics offers the possibility to take internal or external flaws into consideration. Fracture mechanics have been developed by experience from spectacular failures in the 20th century and research from around 2nd World War until present day.

The fundamentals of fracture mechanics will be explained briefly and attention will be drawn to important aspects in context to fracture in cast metals.

3.2.1 From brittle to ductile materials

Griffith introduced the energy balance approach to describe the requirement for a crack to form or grow in brittle materials. The energy balance is mathematically stated as:

$$\frac{dE}{dA} = \frac{d\Pi}{dA} + \frac{dW_s}{dA} = 0 \tag{3.1}$$

Where:

$\Pi = U - W_{ext}$	Potential energy from external forces and internal strain
$U = \int\limits_V U_0 dV$	Strain energy (general formulation)
$U_0 = \int \sigma_{ij} d\varepsilon_{ij}$	Strain energy density
$W_{ext} = F_i \cdot u_i$	Work done by external forces
$W_s = f(\gamma)$	Energy required for the formation of two new surfaces
$\gamma = \gamma_s$	Surface energy before any subjection to plastic deformations
A	Crack area

The change in total energy equals the summation of change in potential energy and surface energy. At the point where the change in total energy is zero, unstable fracture occurs. A graphical representation of the development from incremental crack growth to catastrophically failure is seen in figure 3.2. The catastrophic failure occurs when (3.1) is true.

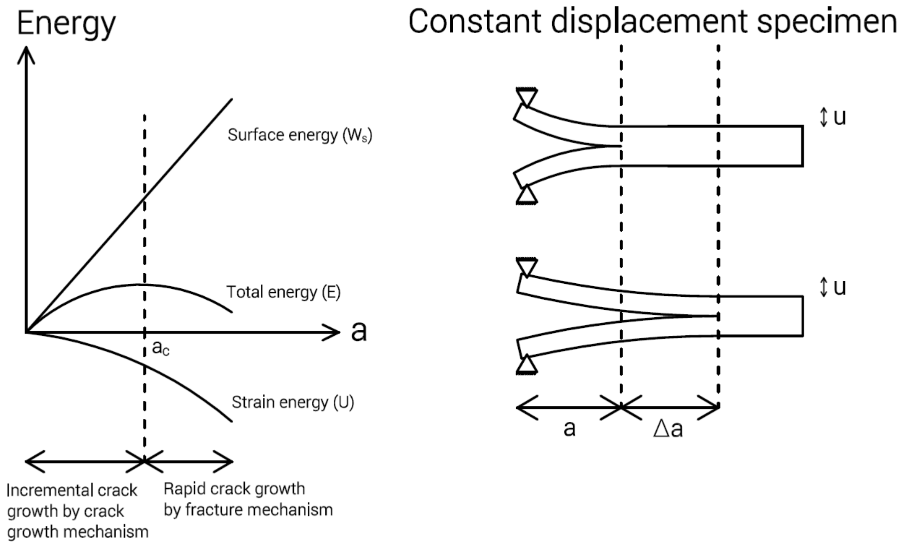

Figure 3.2. Schematized energy balance of test specimen applied a constant displacement where all energies are reset before crack growth.

Later knowledge about ductile materials ability to fail in a brittle manner was established. Irwin [Anderson 2005] extended Griffith's energy balance approach to include ductile materials as they also can exhibit brittle fracture near the crack tip.

This was implemented by including the surface energy, caused by plastic deformation near the crack surfaces. By adding an extra term to the previously mentioned surface energy, ductile materials are included:

$$\gamma = \gamma_s + \gamma_p \tag{3.2}$$

For brittle material $\gamma \approx \gamma_s$ and for ductile materials $\gamma \approx \gamma_p$ is the case. Thus, fracture mechanics can be applicable to ductile cast metals under the conditions that they exhibit brittle fracture behaviour.

3.2.2 Relation between K and G

On basis of Griffith's work an extensive near crack tip stress field research, Irwin [Anderson 2005] successively established the practical relation between the stress intensity factor and the energy release rate, as stated in (3.3), for linear-elastic materials loaded in plane.

$$G = \frac{K^2}{E'} \tag{3.3}$$

Where:

$G = -\frac{\partial \Pi}{\partial A}$	Energy release rate
$K = \sigma \cdot \sqrt{\pi a} \cdot \alpha$	Stress intensity factor
α	Boundary correction factor
$E' = \begin{cases} E \text{ (plane stress)} \\ \frac{E}{1-v^2} \text{ (plane strain)} \end{cases}$	Modulus of elasticity
ν	Poisson's ratio

This conceptual step was further developed, as the energy release rate was later to be proven equal to the J-integral in LEFM:

$$G = J \tag{3.4}$$

Where:

J	J-integral

The J-integral is well implemented in numerical solutions which makes it a powerful tool in fracture mechanics. The critical energy release rate is $G_c = \frac{K_c^2}{E'}$ where K_c is defined as fracture toughness of the material. A further discussion and the mathematical formulation of the J-integral is given in connection with numerical validation in 4.1.

Energy release rate

Energy release rate is an important concept in the understanding and simulation of stable fracture. The energy release rate is equal to the change in dissipated energy per unit crack surface.

Because of the relation in (3.3) the stress intensity factor is utilized as the driving parameter in linear-elastic fracture mechanics. For physical interpretation, figure 3.3 graphically represents the relation between given energy release rate and the material resistance for a given crack.

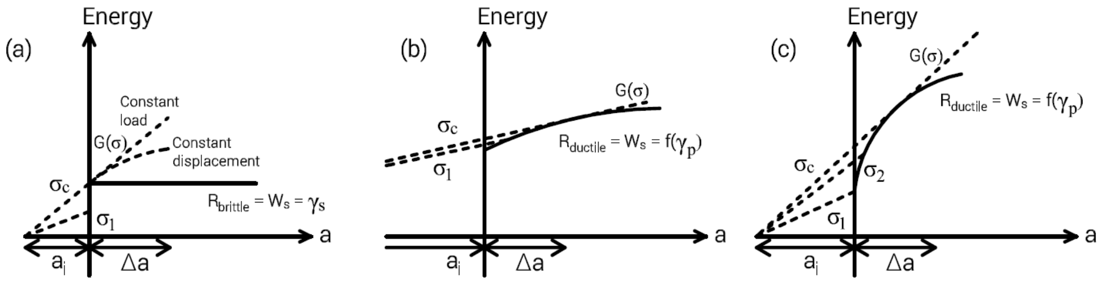

Figure 3.3. Resistance (R) and driving force (G) curves for (a) brittle material, (b) ductile material in plane strain and (c) ductile material in plane stress. At $G_i = R_i$ the crack grows incrementally by stable fracture. However, if $\frac{\partial G_i}{\partial a_i} < \frac{\partial R_i}{\partial a_i}$ the crack resistance increases faster than the crack driving force as the crack grows. Thus, no further crack growth occurs. Once $\frac{\partial G_i}{\partial a_i} = \frac{\partial R_i}{\partial a_i}$ instability occurs and the crack develops rapidly by unstable fracture. [Anderson 2005]

Expectedly, unstable fracture of the brittle material is observed in figure 3.3 (a). Similarity is noticed in plane strain conditions for the ductile material. In figure 3.3 (b) the resistance curve increases slightly which only shortly introduces stable fracture before unstable fracture. Comparatively to the plane strain, the stable fracture is significant under plane stress conditions as seen in figure 3.3 (c).

Hence, in design the difference between the fracture process under plane strain and plane stress conditions has to be considered. This concept will be discussed further in 3.4.2.

3.3 Stress intensity factors

Before Irwin introduced the relation in (3.3) a great effort was made, to describe the stress distributions in the vicinity of cracks.

3.3.1 Application of photoelasticity

In figure 3.4 photoelasticity is utilized to visualize the impact of different discontinuities in a plate.

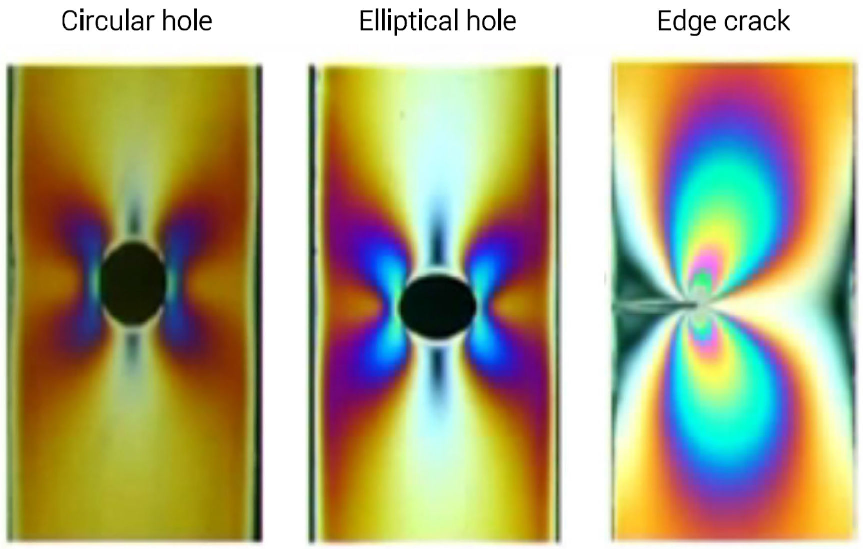

Figure 3.4. Photoelastic plots of isochromatic fringes for different geometries. An isochromatic fringe is a contour of constant stress equal to $\sigma_1 - \sigma_2$ under plane conditions.

The application of photoelasticity was very important in the derivation of the stress field solutions, as photoelastic experiments as seen in figure 3.4 was used as benchmarks for the analytical solutions.

3.3.2 Stress field solutions

Mainly Westergaard, Irwin and R.J. Sanford contributed with conceptual steps in the progress towards a stress field solution. However, it was Williams who came up with a solution which was validated experimentally.

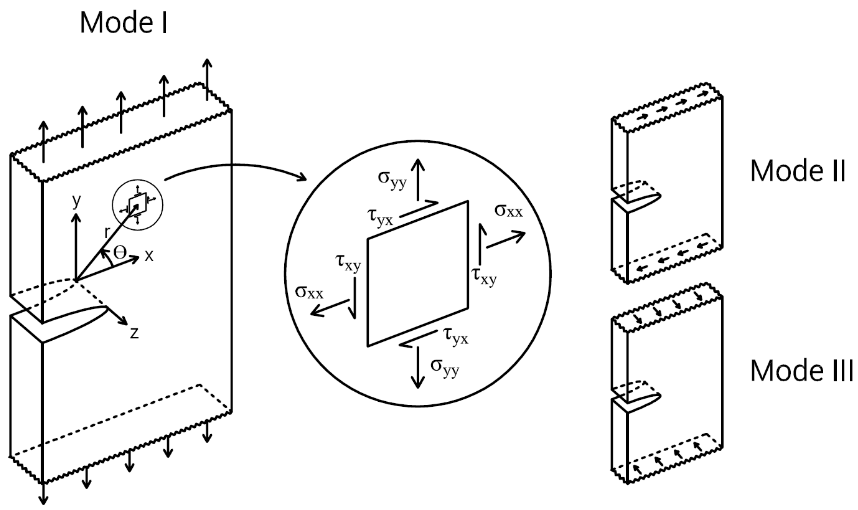

Figure 3.5. Definition of polar coordinate system for the plane stress, near crack-tip stress field solutions in (3.5). Corresponding fracture modes; mode I - opening mode, mode II - sliding and mode III - tearing.

For concise formulation of this section, mathematical derivation of the stress field solutions is omitted, and reference is made to literature, e.g. [Williams 1956], [Anderson 2005].

The near crack-tip stress, strain and displacement field solutions for a linear-elastic isotropic material, loaded in mode I and II are listed in (3.5) and graphically represented in figure 3.5.

$$
\begin{aligned}
\sigma_{ij} &= \frac{K_I}{\sqrt{2\pi r}} f^{I}_{ij}(\theta) + \frac{K_{II}}{\sqrt{2\pi r}} f^{II}_{ij}(\theta) + \frac{K_{III}}{\sqrt{2\pi r}} f^{III}_{ij}(\theta) \\
u_{ij} &= \frac{K_I}{2\mu}\sqrt{\frac{r}{2\pi}} g_j^{I}(\theta,\nu) + \frac{K_{II}}{2\mu}\sqrt{\frac{r}{2\pi}} g_j^{II}(\theta,\nu) + \frac{2K_{III}}{\mu} g_j^{III}(\theta,\nu) \\
\varepsilon_{ij} &= \frac{1}{2}\left(u_{i,j} + u_{j,i}\right)
\end{aligned}
\tag{3.5}
$$

As expected the stress intensity factor controls the amplitude of stress which the crack-tips are exposed to. The singular term $\frac{1}{\sqrt{r}} \to \infty$ as the solution approaches the crack-tip. However, when the solution goes away from the crack-tip $\frac{1}{\sqrt{r}} \to 0$. Thus, the solutions in (3.5) are only valid in the proximity of the crack-tip. Limitations of linear-elastic fracture mechanics, induced by the plastic zone size, are discussed in 3.5.4.

3.3.3 Geometry dependence

The boundary correction factor α is introduced in order to take the geometrical influence on stress intensities into account. The following section discusses some different aspects of the geometry dependence.

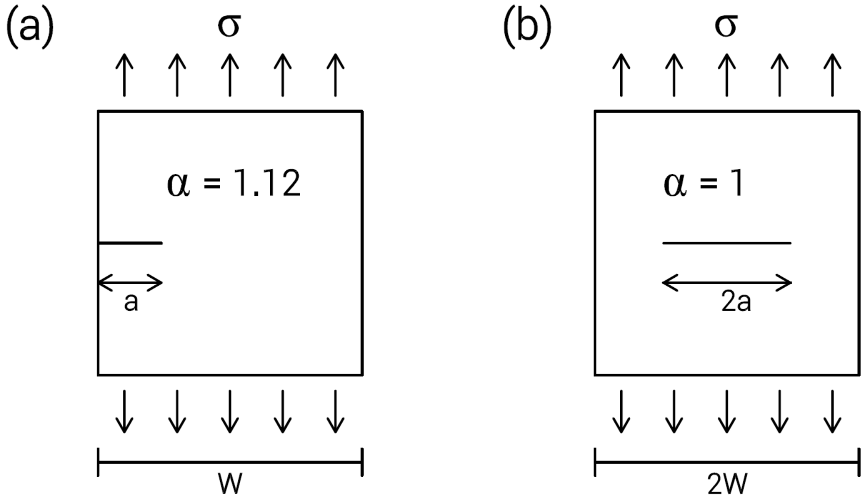

Figure 3.6. Different two dimensional crack problems; (a) edge crack and (b) center crack with$a = 2mm$, $W = 100mm$ and $\sigma = 100MPa$. For analytical solution see "APP 1".xx

Expectedly figure 3.6a is the most critical case. The presence of a free surface near the crack decreases stiffness in the proximity of the edge crack. Hence, the geometrical factor increases and thereby the stress intensity increases. Therefore, generally are cracks near free surfaces often more critical than internal cracks.

An elliptical embedded crack is considered in figure 3.7. The crack shape influence on the stress intensity factor is discussed in the following.

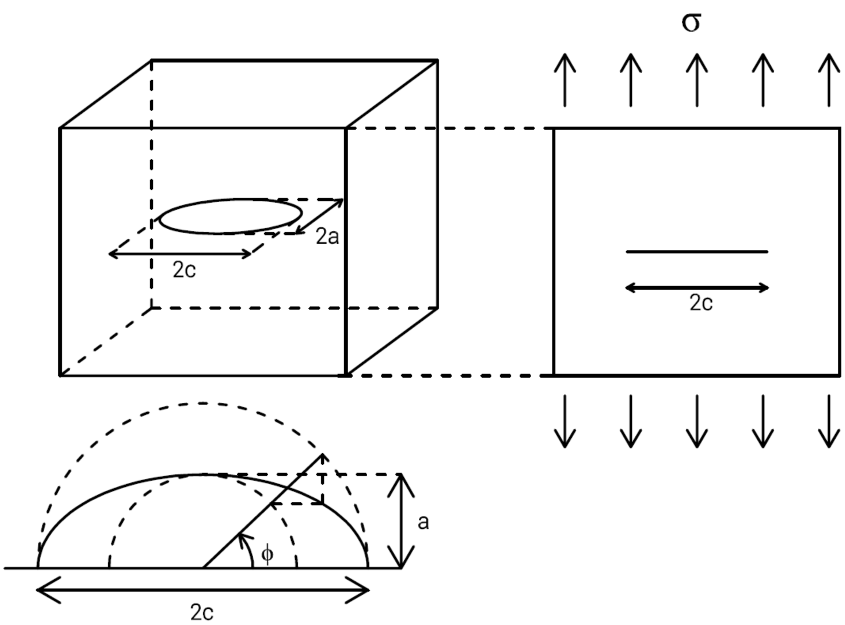

Figure 3.7. Geometry definitions of an elliptical crack embedded in an infinite body. For analytical solution see "APP. 1".xx

A normalized stress intensity factor is evaluated by means of the analytical solutions given in "APP. 1"xx, see figure 3.8. The normalized stress intensity factor depicts the influence of the $\frac{a}{c}$ ratio or crack shape.

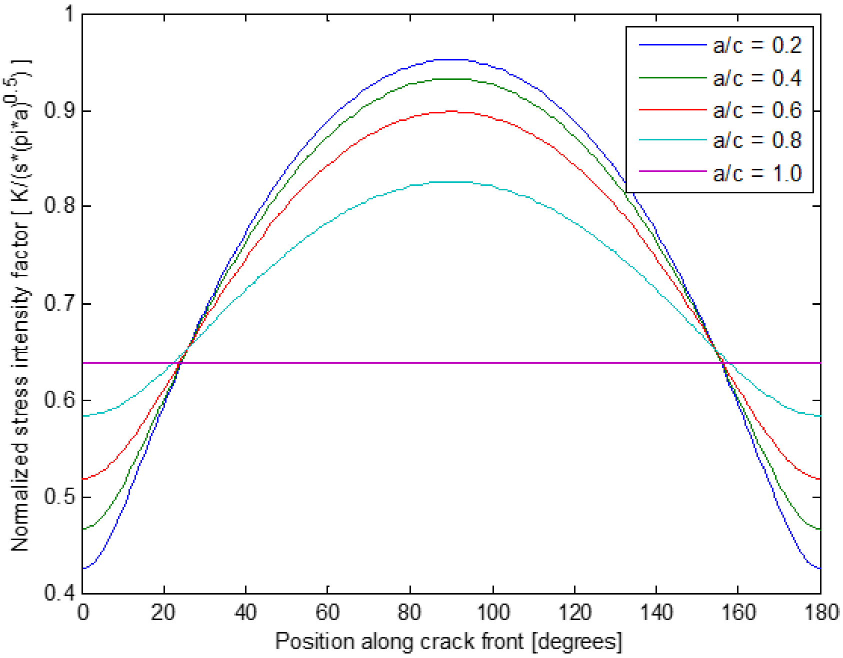

Figure 3.8. Graphical representation of the crack shape influence on the stress intensity factors.

The circular embedded crack $\frac{a}{c} = 1.0$ is constant along the crack front. As the ellipse forms and narrows in, the normalized stress intensities peak at 90° and keep increasing with decreasing $\frac{a}{c}$ ratio. Therefore, two concepts are observed: A crack will tend to grow towards a circular shape; and the narrower or sharp the crack is the more critical.

The crack problem, evaluated above, was embedded in an infinite body. Hence, no boundary corrections were introduced. However, for surface flaws boundary corrections are introduced and are evaluated in the following.

Surface cracks can be in the proximity of more than one surface, which can cause more critical crack geometry. For the analytical solution of a semi-elliptical surface crack subjected to tensile and bending stresses, see "APP. 1"xx.

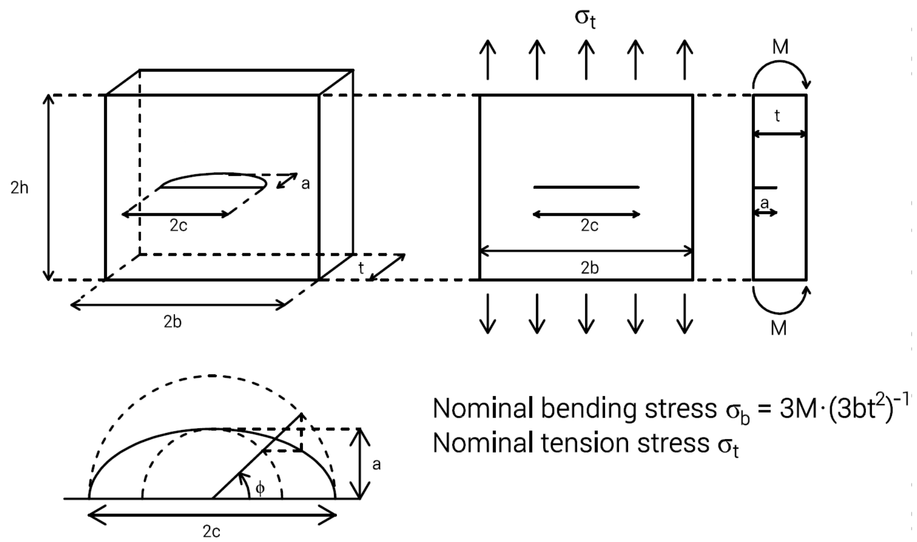

Figure 3.9. Geometry definitions of semi-elliptical surface crack. For analytical solution see "APP. 1".

Before the influence of crack shape was evaluated by considering a normalized stress intensity factor for different $\frac{a}{c}$ ratios. Now, instead the $\frac{a}{t}$ ratio (see figure 3.9) is tested. Normalized stress intensity factors are calculated for different $\frac{a}{t}$ ratios in figure 3.10.

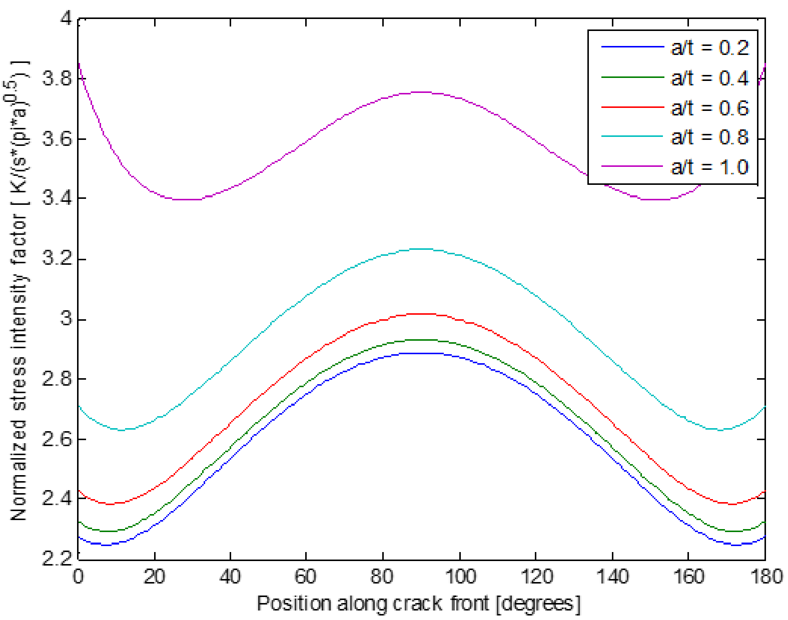

Figure 3.10. Graphical representation of the thickness influence on the stress intensity factors.

In figure 3.10 it is noticed that the normalized stress intensity factors increase as the surface crack depth approaches the plate thickness.

Considering $\frac{a}{t} = 1.0$ the normalized stress intensity factors for $\phi = \begin{cases} 0^\circ \\ 180^\circ \end{cases}$ are almost equal to $\phi = 90^\circ$ which means the crack tends to grow equally.

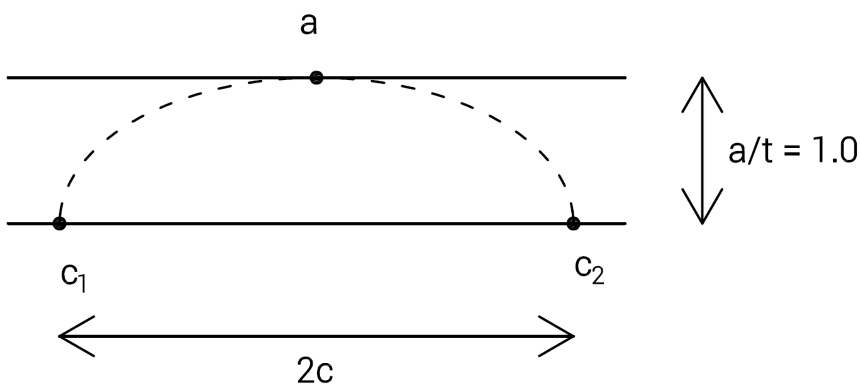

Figure 3.11. Semi-elliptical surface crack which has the ratio $\frac{a}{t} = 1.0$.

Considering figure 3.11 point a, c_1 and c_2 are all positioned at a free surface. Thus, it makes sense that the normalized stress intensity factors, seen in figure 3.10, are almost equal. Hence, surface cracks of constant shape becomes more critical as they approach through cracks.

3.3.4 Summary

From analytical considerations it is concluded that cracks criticality depends on distance to free surfaces, crack shape and how deep the crack is.

3.3.5 Superposition principles for stress intensity factors

As illustrated in figure 3.5, a crack-tip can suffer from three different fracture modes. A solution for a fracture mechanical problem should depend on stress intensity factors for all activated fracture modes. Dealing with linear-elastic material superposition of equal-mode stress intensity factors is valid as:

$$K_I = K_{I,tension} + K_{I,bending} \tag{3.6}$$

Hence, one focused on mathematical efficiency could erroneously think that superposition of stress components would still valid.

$$K_I \neq (\sigma_{tension} + \sigma_{bending}) \cdot \sqrt{\pi a} \cdot \alpha \tag{3.7}$$

However, for (3.7) to be valid both of the stress components should be corrected by the same α-value. This is not the case.

3.3.6 Mixed mode loading

By considering the formulation in (3.1) by Griffith and the relation eqrefeq:enrel1 by Irwin, the energy release rate for mixed mode loading [Anderson 2005] can be expressed as:

$$G = G_I + G_{II} + G_{III} = \frac{{K_I}^2}{E'} + \frac{{K_{II}}^2}{E'} + \frac{(1+v) \cdot {K_{III}}^2}{E} \tag{3.8}$$

Where:

$$E' = \begin{cases} E \text{ (plane stress)} \\ \frac{E}{1-v^2} \text{ (plane strain)} \end{cases} \quad \text{Modulus of elasticity}$$

By means of isolation, an equivalent stress intensity factor can be expressed as:

$$K_{eq} = \left({K_I}^2 + {K_{II}}^2 + (1+v) \cdot {K_{III}}^2\right)^{1/2} \tag{3.9}$$

However, the expressions (3.8) and (3.9) assume self-similar crack growth[Anderson 2005] which is illustrated in figure 3.12.a.

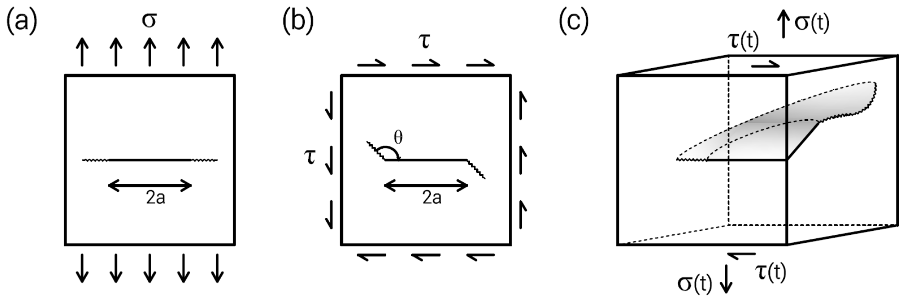

Figure 3.12. Graphical schematization of (a) self-similar, (b) biaxial and (c) multi-axial crack growth.

In reality not all cracks can be assumed to grow in a self-similar manner. Instead, biaxial and multi-axial crack growth is noticed. Therefore, an alternative approach to (3.9) is needed for simulation of cracks which do not tend to grow in a self-similar manner.

3.4 Experimental derivation and crack growth models

In fracture mechanics material parameters, obtained from experiments, are necessary. This section provides a brief introduction of the derivation of the material parameters used in linear-elastic fracture mechanic. The brief introduction is intended to substantiate the following presentation of three crack growth models. Lastly, important aspects of fracture toughness will be discussed.

In limit state analysis the yield stress is used as the material resistance parameter. In fracture mechanical analysis the material resistance parameter is thefracture toughness. The fracture toughness is a measure of a material's ability to resist fracture.

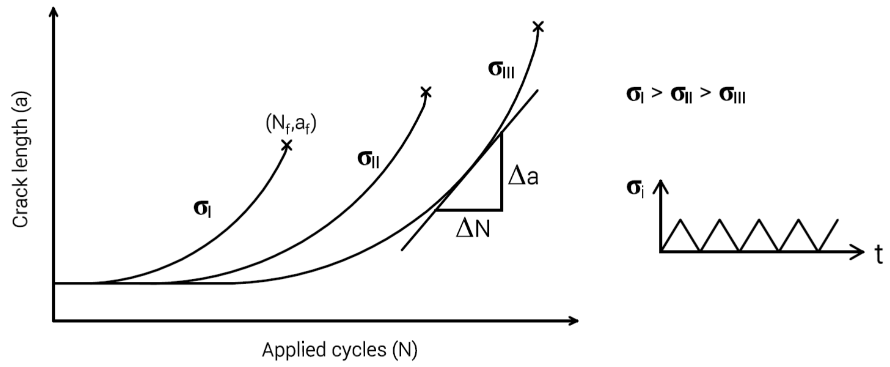

Figure 3.13. Graphical representation of crack growth life behavior.

Experiments as illustrated in figure 3.13 are carried out in order to predict the fracture toughness. Basically the experiments are done by measuring crack growth in relation to the number of applied load cycles. Loading is applied until failure and the graphical representation of the experiment is illustrated by the plot in figure 3.13.

In figure 3.14 a common used SEN(B) specimen illustrated.

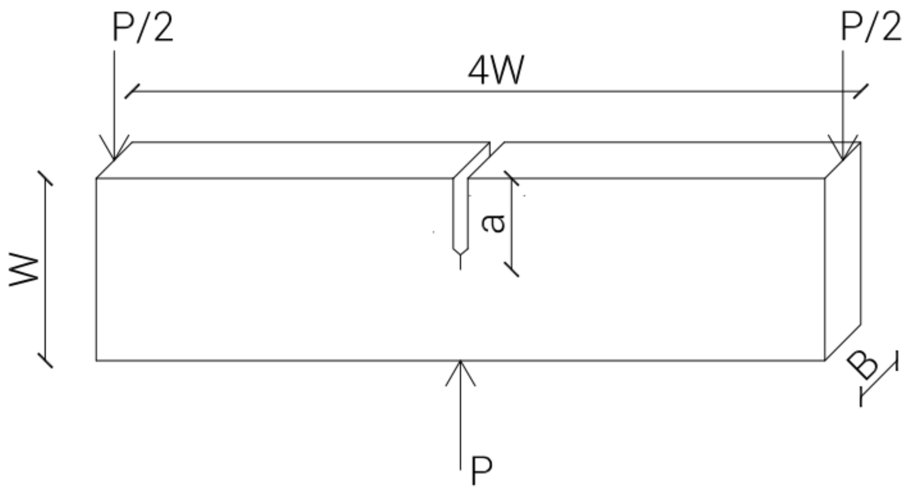

Figure 3.14. SEN(B) specimen used for fracture toughness testing.

The stress intensity for the SEN(B) specimen is given as:

$$K = \frac{4P}{B}\sqrt{\frac{\pi}{W}}[1.6(\frac{a}{W})^{\frac{1}{2}} - 2.6(\frac{a}{W})^{\frac{3}{2}} + 12.3(\frac{a}{W})^{\frac{5}{2}} - 21.2(\frac{a}{W})^{\frac{7}{2}} + 21.8(\frac{a}{W})^{\frac{9}{2}}] \tag{3.10}$$

The experiments are not only used for determination of the fracture toughness of certain materials but also to model the crack growth rate behavior. By means of the analytical expression (3.10) for the SENB specimen in figure 3.14, and the established data from experiments in figure 3.13, the crack growth rate behavior is illustrated in figure 3.15.

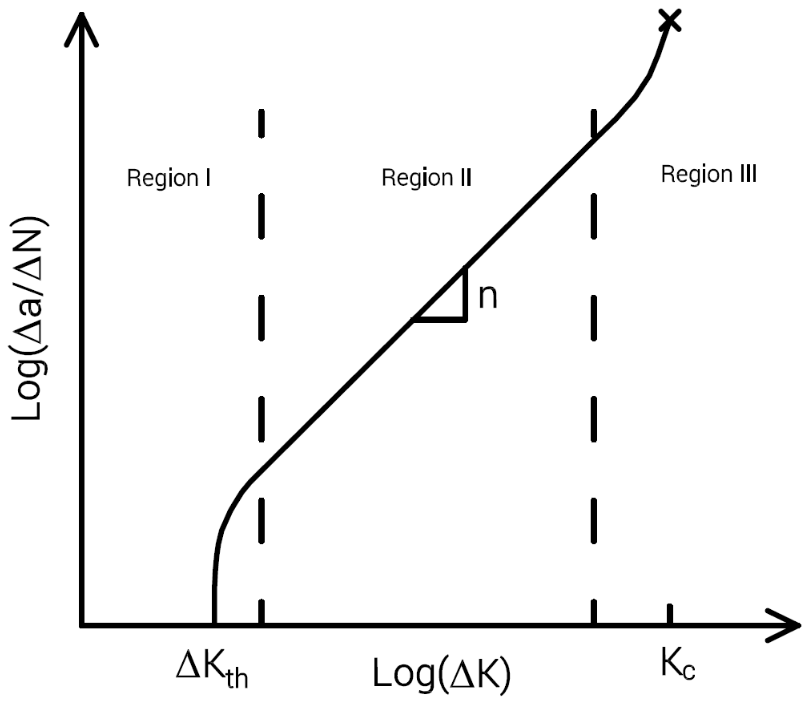

Figure 3.15. Schematized crack growth rate behavior. The threshold stress intensity factor K_{th} defines where the crack initiates. The critical stress intensity factor K_c defines where failure occurs, also known as a given materials fracture toughness.

Region 1 contains relatively small crack growth rates whereas region 3 contains a low number of cycles due to high crack growth rates. Region 2 shows a linear crack growth rate behavior, which was noticed by Paris. Paris [M.P.Gomez & E.Anderson 1961] proposed a simple crack growth model which only considers cycles contained in region 2, see (3.11).

By fitting a curve to the line in figure 3.15, an empirical formula for the given crack growth behavior is established in (3.11). Because the empirical formula is fitted to the crack growth rate behavior, the formula is in literature known as a crack growth model.

$$\frac{da}{dN} = C \cdot (\Delta K)^n \tag{3.11}$$

Where:

$\frac{da}{dN}$	Crack growth rate
C, n	Experimental material parameter for Paris' law
$\Delta K = \Delta\sigma \cdot \sqrt{\pi a} \cdot \alpha$	Stress intensity factor range

As different load cases were carried out, dependency of applied mean stress was realized. In figure 3.16 increasing crack growth rate behaviors is noticed as the applied mean stress increases.

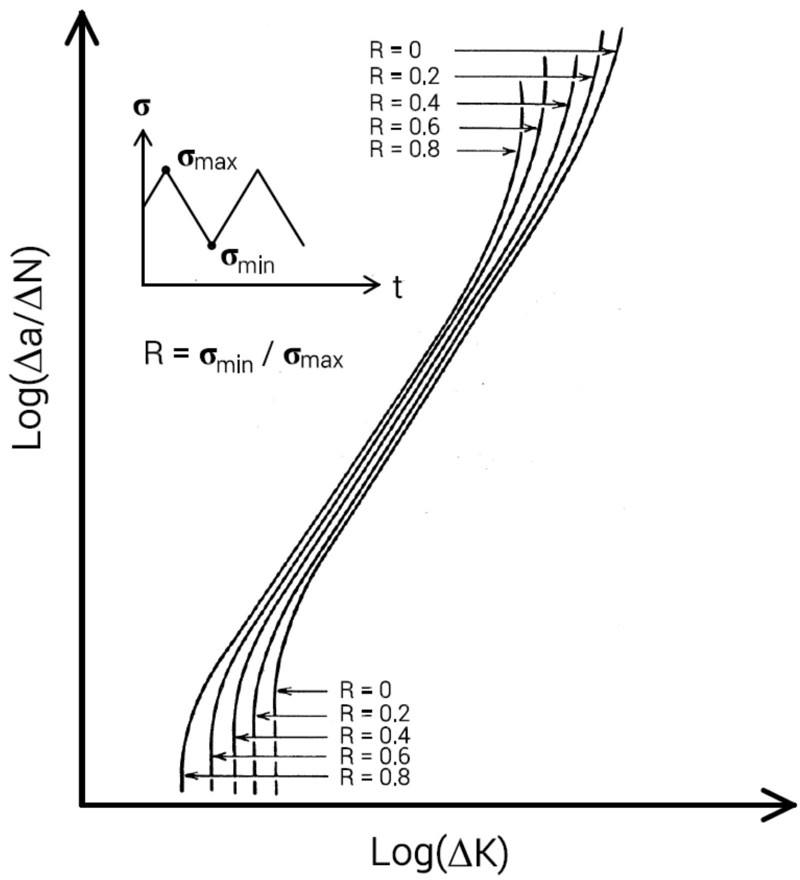

Figure 3.16. Crack growth rate dependency on mean stress.

By considering experimental results like those in figure 3.16, Forman [E.Kearney & Engle 1967] proposed an alternative crack growth model considering the dependency of the applied mean stress and region 3. The Forman equation is expressed as:

$$\frac{da}{dN} = \frac{C' \cdot (\Delta K)^{n'}}{(1-R) \cdot K_c - \Delta K} \tag{3.12}$$

Where:

C, n	Experimental material parameter for Forman equation
$R = \frac{\sigma_{\min}}{\sigma_{\max}}$	Stress ratio (ratio between minimum and maximum applied stress)
$K_c = \sigma_c \cdot \sqrt{\pi a_c} \cdot \alpha_c$	Fracture toughness
$K_{\max} = \sigma_{\max} \cdot \sqrt{\pi a} \cdot \alpha$	Maximum stress intensity factor in a cycle

Region 2 in figure 3.16 is only slightly shifted. However, when considering region 1 and 3 a larger difference is noticed. As seen in (3.12) Forman considered the importance of applied means stress, but he also tried to capture the behavior in region 3 by bringing the fracture toughness into the equation.

For a more general case, NASGRO (3.13) considers all three regions, applied mean stress and crack closure. The concept of crack closure is further explained and discussed in **??**. The Forman/Mettu equation is given as:

$$\frac{da}{dN} = C \cdot [(\frac{1-f}{1-R}) \cdot (\Delta K)]^n \cdot \frac{(1 - \frac{\Delta K_{th}}{\Delta K})^p}{(1 - \frac{K_{\max}}{\Delta K_c})^q} \tag{3.13}$$

Where:

C, n, p, q	Experimental material parameters for Forman/Mettu
$f = \frac{K_{op}}{K_{\max}}$	Crack opening function

By looking at (3.11), (3.12) and (3.13) it is noticed that the number of needed experimental parameters increases with the number of considered regions. In 3.4.1 the three crack growth models are evaluated with respect to crack growth modelling of cast metals.

3.4.1 Evaluation of crack growth models

In this section three different crack growth models are tested, namely Paris-Erdogan, Forman and NASGRO.

NASGRO can predict all three crack growth regions where Forman can predict Region II and III and Paris-Erdogan is restricted to region II. NASGRO and Forman also have the ability to consider load ratio. NAGRO being the most advanced growth model, requires the most crack growth parameters. It requires 9 parameters, where Forman requires 3 and Paris-Erdogan 2. These parameters are not always easily available, so for a given situation one must evaluate the cost/benefit relation of each model.

To evaluate the crack growth models, the crack growth models have been fitted to experimental results[NASA 1959], to investigate their accuracy and the impact of stress ratio. In the experiment, the test specimens were loaded uniaxially, corresponding to mode 1, and subjected to a wide range of load-ratios ranging from -1.0 to 0.8. The specimens where thin plates with centered through-cracks. The geometry and dimensions of the specimens are given on figure 3.17.

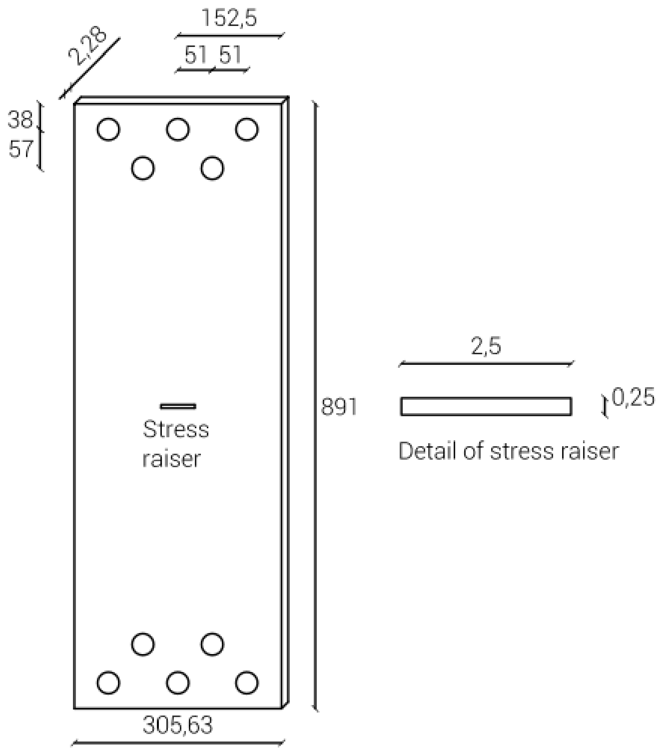

Figure 3.17. Test specimen of crack growth rate behavior experiments.

It should be noted that the material of the specimens is the aluminum alloy, 7075-T6, and not cast metals, which is the main focus in this thesis. The goal is to make some general remarks of crack growth models, and for this, the aluminum alloy serves the purpose.

The results from the experiment are illustrated as crack growth rate behavior on figure 3.18. The material parameters C and n has been determined by fitting the crack growth models to the case where the stress ratio is equal to zero. The remaining material parameters, necessary for Forman and NASGRO, have been found in the NASGRO material catalog. The material parameters, which have been used, are given in table 3.1.

Model	C	n	K_c	p	q	ΔK_1	C_{th}^{+}	C_{th}^{-}	α
Paris-Erdogan	$9.33 \cdot 10^{-12}$	3.21	-	-	-	-	-	-	
Forman	$9.07 \cdot 10^{-9}$	3.21	1460						
Nasgro	$2.24 \cdot 10^{-11}$	3.23	1460	0.5	1.0	26.06	2.5	0.1	2.0

Table 3.1. Crack growth parameters.

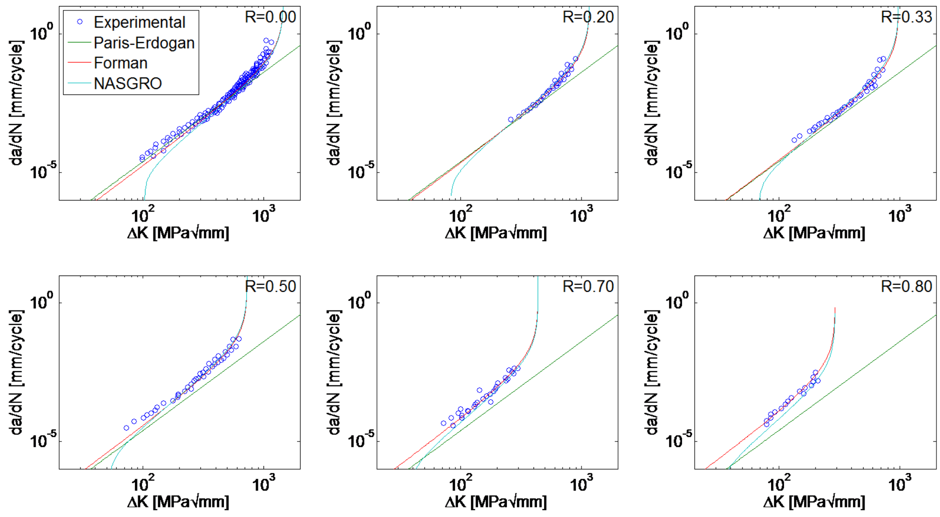

Figure 3.18. Crack growth rate behavior curves for load-ratio from 0.00-0.80.

From figure 3.18, is it evident that all three models are able to predict the crack growth with reasonable accuracy when the load ratio is zero. When the load ratio increases Forman and NASGRO are still able to predict the crack growth rate accurately, where Paris-Erdogan becomes increasingly inaccurate. This is expected since Forman and NASGRO takes the load ratio into account but Paris-Erdogan does not. This can make Paris-Erdogan impractical since it requires new material parameters for each load ratio. Forman and NASGRO seem to predict the results equally well and are very similar in region II and III. The difference between Forman and NASGRO becomes apparent in region I. Forman can not predict the crack growth rate region I and is quite similar to Paris-Erdogan in this region. NASGRO should be able predict crack growth in region I, but these results can not be used to verify the accuracy, since crack propagation in region I, was not recorded.

To determine if NASGRO accurate can describe region I, an experiment [Biermann 2007], were crack growth rates in region I was recorded, will be used to prove or disprove NASGRO's ability to describe region I. The specimen in the experiment is a single edge notch specimen(SENB), which is illustrated on figure 4.1. The specimen has the following measurements B=10mm, W=20mm. The specimen is made of a nodular cast iron, specifically EN-GJS-400-18LT. The crack growth parameters for NASGRO were given in the experiment, were the crack growth parameters for Forman has been determined by evaluating the best fit. The crack growth parameters are given in table 4.2.

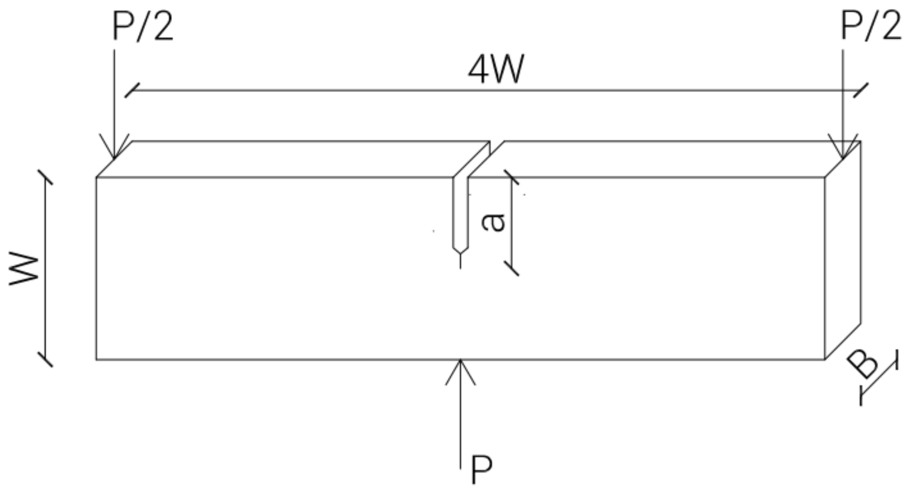

Figure 3.19. SENB specimen geometry.

Model	C	n	K_c	p	q	ΔK_1	C_{th}^{+}	C_{th}^{-}	α
Forman	$7.00 \cdot 10^{-12}$	2.49	1049.88						
Nasgro	$6.19 \cdot 10^{-15}$	3.80	1049.88	0.40	0.40	111.5	2.6	0.1	2.5

Table 3.2. Crack growth parameters.

The results from the comparison between Forman, NASGRO and the experiment is illustrated on figure 3.20.

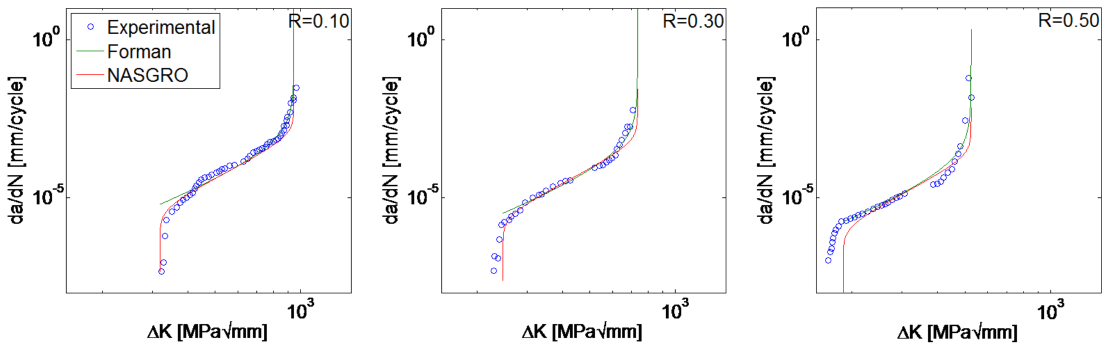

Figure 3.20. Crack growth rate behavior in all three regions.

From figure 3.20 can it be seen that NASGRO generally does a good job of describing the crack growth rates in all three regions. In region I is it clear Forman over estimates the crack growth which could lead to a conservative estimation of lifetime. To illustrate how Forman's overestimation of the crack growth influences the estimation of lifetime, an analytical example has been carried out. The test specimen is a SENB specimen with the following measurements $B = 10mm$, $W = 20mm$, $a_i = 5mm$. The crack growth parameters are given in table 4.2. The applied load is $\Delta P = 2750N$ with a load ratio of $R = 0.1$, this ensures that region I will be present, as illustrated on figure 3.21.

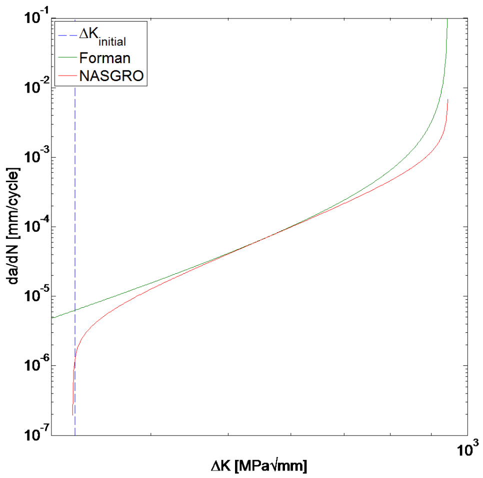

Figure 3.21. The presence of region I at the initial stress intensity.

The result from the analytical example is illustrated on figure 3.22.

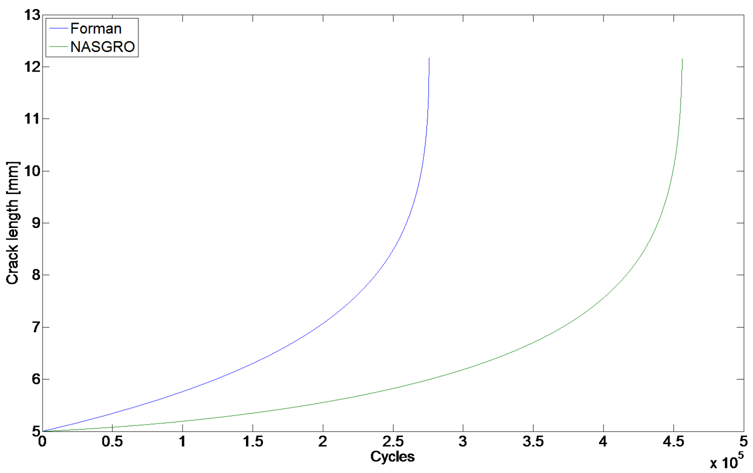

Figure 3.22. Difference in crack life behavior curves for Forman and NASGRO.

From figure 3.22 is clear that Forman's omission of region I has a significant influence of estimation on lifetime. Forman underestimates the lifetime by 39.6 % compared to NASGRO, making Forman very conservative when region I is present. However, in cast metals initial cracks may be large enough to already be in region II from birth.

3.4.2 Fracture toughness

Before any fracture mechanical analyses are carried out, a number of important aspects of the fracture toughness have to be considered. In the following temperature and thickness dependencies will be discussed.

In 1940's the catastrophic number of failing Liberty ships formed the basis of interest in brittle fracture of ductile materials. The ships were observed to fail in a brittle manner, although they were constructed from ductile steels. Additionally, the failures mainly occurred in the northern seas where temperatures were relatively low.

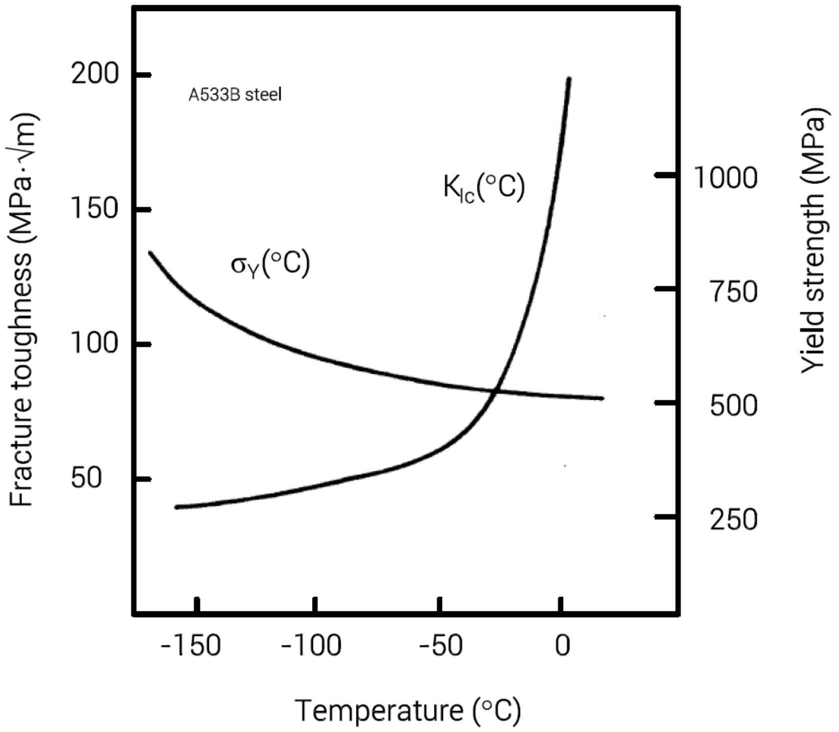

Figure 3.23. Yield strength and fracture toughness dependence on temperature.

It was later discovered that depending on the temperature, ductile materials exhibits brittle or ductile behavior. As illustrated in figure 3.23, the fracture toughness should not be considered proportional to the yield strength. Hence, it is important to determine the temperature range at which a given component is used. If structures/vessels are travelling around the world, brittle and ductile fracture could be a possibility. Therefore, both situations need to be taken into consideration in order to design appropriately.

Another important aspect is the fact that fracture toughness depends on the component thickness. A graphical representation of the dependency is seen in figure 3.24.

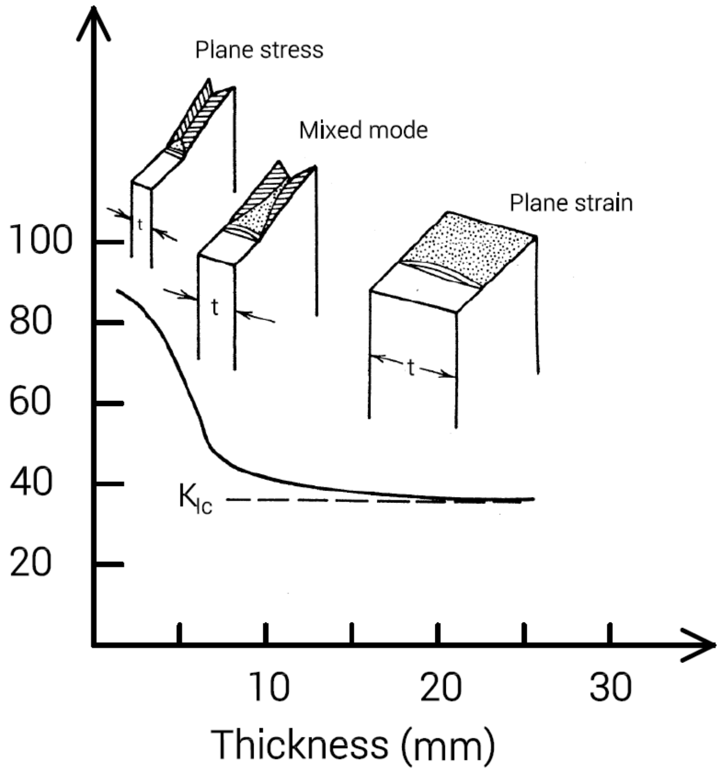

Figure 3.24. Fracture toughness dependence of component thickness for a ductile material for which the crack propagates in a ductile manner. The angled slip planes introduced, also referred to as shear lips, is caused by low triaxial stress state near the free surface in plane stress. [Anderson 2005]

The fracture toughness needs to be determined, not only as a function of temperature, but also component thickness. In figure 3.24 it is noticed that increasing thickness leads to decrease in fracture toughness. Eventually, the fracture becomes constant and is denotedK_{Ic}, which is the fracture toughness for plane strain components. In practice, the fracture toughness is often referred to as K_{Ic} for the sake of conservatism. Assuming the fracture toughness equal to K_{Ic}, many load cycles could be incorrectly excluded from an optimization point of view.

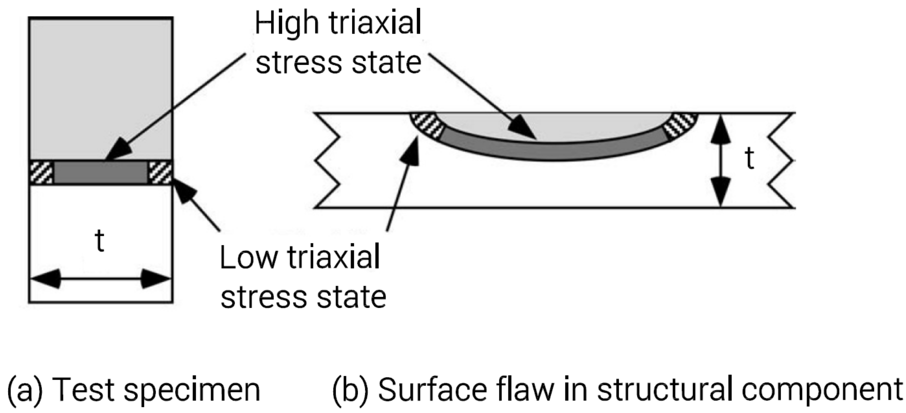

Figure 3.25. Tri-axial stress states in a (a) edge-cracked test specimen (b) surface cracked component. [Anderson 2005]

However, fracture toughness' from tests are not always applicable. The triaxial stress state in a through edge specimen depends on the thickness (figure 3.25.a). In contradiction to this, a surface crack's triaxial stress state depends on the crack front length which not necessarily depends on the thickness (figure 3.25.b). Hence, equal fracture morphology is not guaranteed and the fracture toughness is not directly related to the same kind of situation.

Hence, the structural application has to be considered, when carrying out the fracture toughness testing, for the fracture toughness to be a valid material parameter.

3.5 Crack tip plasticity

The fracture toughness is, in linear-elastic fracture mechanics, supposed to be an applicable material parameter expressed as a critical stress intensity factor. Thus, it has to be independent of a cracked body's geometry and overall dimensions. In order for this to be true, the plastic zone size is for monotonic and cyclic loading suggested to be restricted to $r_y \leq \frac{a}{8}$ and $r_y \leq \frac{a}{4}$ respectively.

In the following section important aspects of the plastic zone are discussed.

3.5.1 Plastic zone size

The triaxial stress state is different in plane stress and plane strain, see figure 3.26. The out-of-plane compressive stress, σ_z, reduces the plastic zone size in plane strain situations. However, due to low triaxial stress states near the surface (see figure 3.25), the plastic zone size near the surface will always be approximately the plane stress plastic zone size.

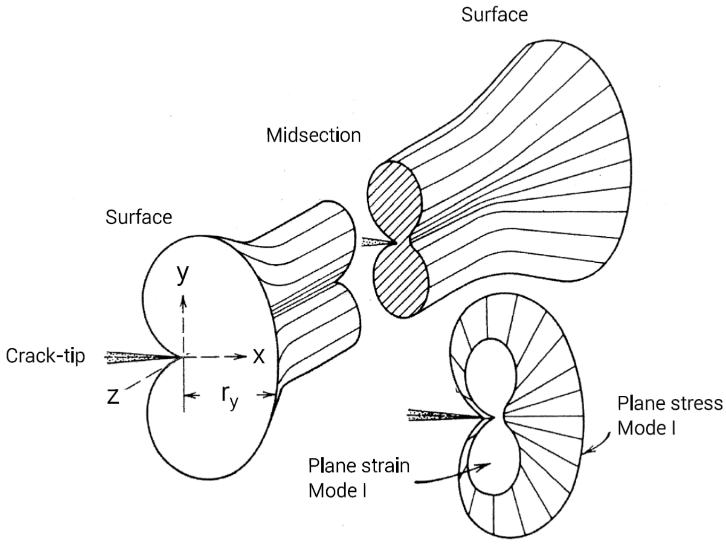

Figure 3.26. Plastic zone size at the crack-tip of a through crack. [Anderson 2005]

A first-order estimate of the plastic zone size is for plane stress conditions given as:

$$\sigma_{yy} = \sigma_Y = \frac{K_I}{\sqrt{2\pi r_y}} \rightarrow r_y = \frac{1}{2\pi}(\frac{K_I}{\sigma_Y})^2 \tag{3.14}$$

The plain strain plastic zone size is recommended to be taken as 1/3 of the plane stress plastic zone size in (3.14).

However, by reconsidering the elastic stress field solutions, corrections might be necessary due to the singular stresses at the crack-tip, predicted by the elastic solution.

3.5.2 Irwin's approach

Irwin stated that the plastic zone in 3.26 is too small, because the stresses above the yield limit are not considered. The problem is illustrated in figure 3.27. Stresses must be redistributed in order to satisfy equilibrium and still physically make sense. Every material fails before reaching an infinite state of stress, and even small loadings results in infinite stresses.

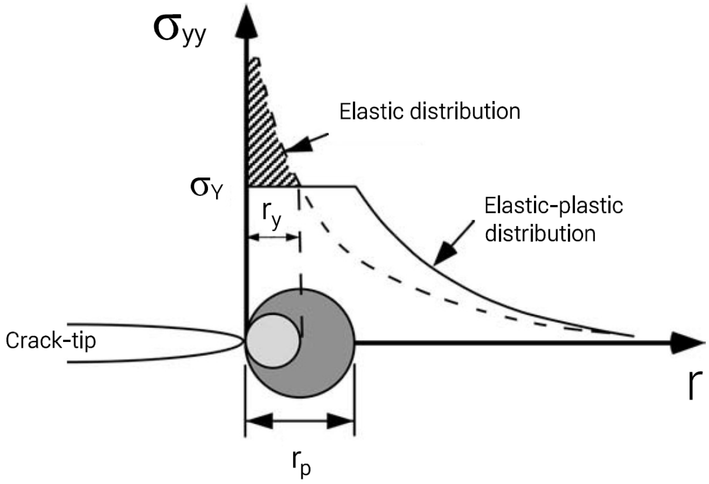

Figure 3.27. Graphical representation of Irwin's approach. The elastic stress field solutions introduce stresses above the material's yield limit, at a distance r_y from the origin. These stresses are in reality not possible, but indeed required to obtain equilibrium. Hence, the elastic stress region above σ_y are redistributed by increasing the plastic zone size from r_y to r_p. [Anderson 2005]

The redistribution of stresses introduces an increased plastic zone at the crack-tip. From this perspective Irwin came up with a second-order estimate of the plastic zone size expressed in (3.15) under plane stress conditions.

$$r_p = 2r_y = \frac{1}{\pi}(\frac{K_I}{\sigma_Y})^2 \tag{3.15}$$

Irwin proposed an effective crack length due to the relatively soft behavior of the plastic zone. The effective crack length is expressed as:

$$a_{eff} = a_i + r_y \tag{3.16}$$

Then the effective stress intensity factor is stated in (3.17) and requires iterations in order to converge.

$$K_{eff} = \sigma \cdot \sqrt{\pi a_{eff}} \cdot \alpha_{eff} \tag{3.17}$$

Where:

$\alpha_{eff} = f\,(a_{eff})$ Effective geometrical factor

3.5.3 Strip yield model by Dugdale

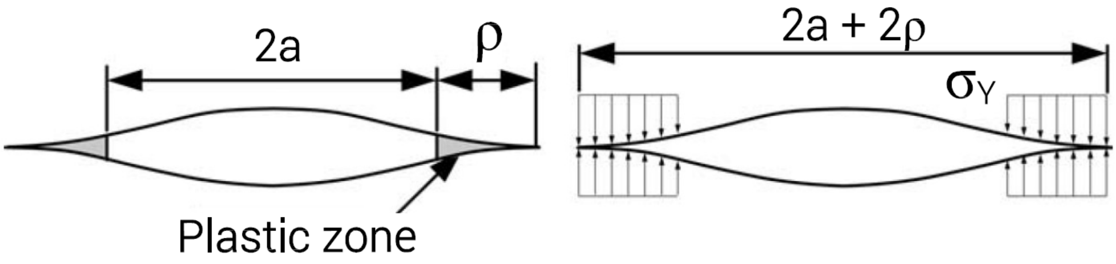

Figure 3.28. Strip yield model by Dugdale. The plastic zone is estimated by considering the required distance of yield magnitude compressive stresses at the crack-tips. [Anderson 2005]

Dugdale proposed the strip yield model, illustrated in figure 3.28. The plastic zone, under plane stress conditions, estimated by the strip yield model is expressed as:

$$\rho = \frac{\pi}{8}(\frac{K_I}{\sigma_Y})^2 \approx \frac{1.23}{\pi}(\frac{K_I}{\sigma_Y})^2 \tag{3.18}$$

Dugdale's strip yield model is relatively close to the plastic zone proposed by Irwin in (3.15). Burdekin and Stone [F.M. & Stone 1966] proposed a formulation of Dugdale's strip yield model as:

$$K_{eff} = \sigma_Y \cdot \sqrt{\pi a} \cdot [\frac{8}{\pi^2} \ln(\sec(\frac{\pi \sigma}{2\sigma_Y}))]^{1/2} \tag{3.19}$$

3.5.4 Plastic zone limitations

To illustrate how the stress intensity factor is corrected in relation to the applied stress, a graphical representation is given in figure 3.29.

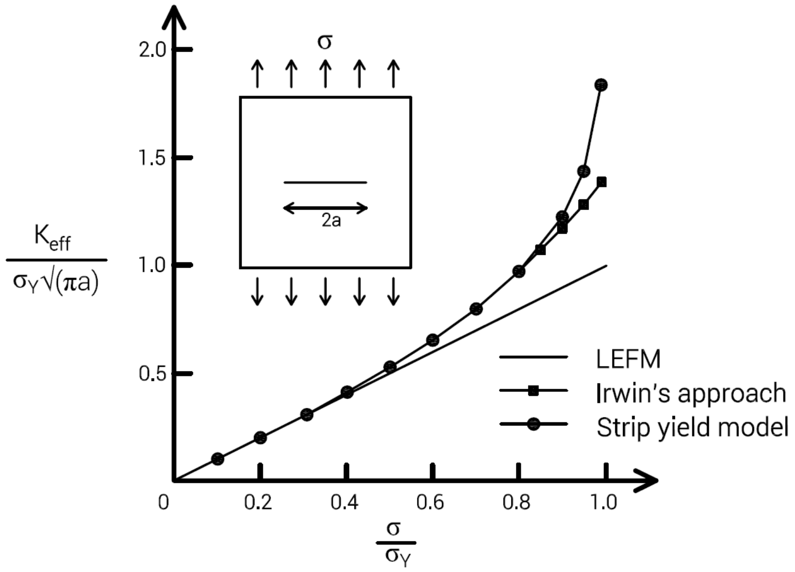

Figure 3.29. Example of plastic zone corrections for a through crack, in a mode I loaded plate, under plane stress conditions.

Looking at figure 3.29, linear-elastic fracture mechanics need corrections when $\sigma \approx 0.45\sigma_Y$. Thus, linear-elastic fracture mechanics is well suited while $\sigma << \sigma_Y$, but need corrections when $0.4\sigma_Y < \sigma < 0.8\sigma_Y$. [Anderson 2005]

Load-bearing offshore structures are considered to be loaded mainly in $\sigma << \sigma_Y$ because of the ultimate limit state requirement. Hence, are neglected in the algorithm proposed in this thesis.

For extensive yielding at the crack-tip, elastic-plastic fracture mechanics is available. However, only linear-elastic fracture mechanics is emphasized in this thesis.

3.5.5 Load interaction effects

3.5.5.1 Crack closure

During fatigue crack growth cracks exhibit what is known as crack closure. The crack closure mechanisms are introduced in order to account for a crack which tends to close before it is fully unloaded. A number of different crack closure mechanisms are illustrated in figure 3.30.

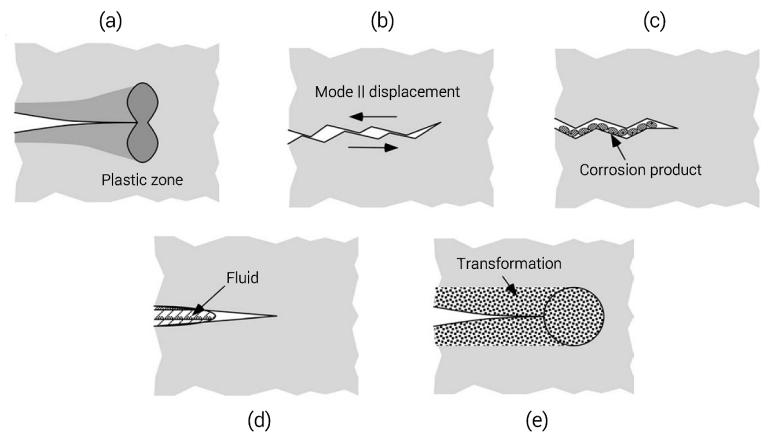

Figure 3.30. Illustrations of fatigue crack closure mechanisms which occur in metals, as well as cast metals. (a) Plasticity-induced closure (b) roughness-induced closure (c) oxide-induced closure (d) closure induced by a viscous fluid and (d) transformation-induced closure. [Suresh & Ritchie 1984]

By considering the crack closure concepts, less conservative crack growth behavior can be formulated, which leads to increased fatigue life. The crack closure concept was proposed by [Elber 1977] and after years of research, finally accepted. In figure 3.31 plasticity-induced closure is graphically explained.

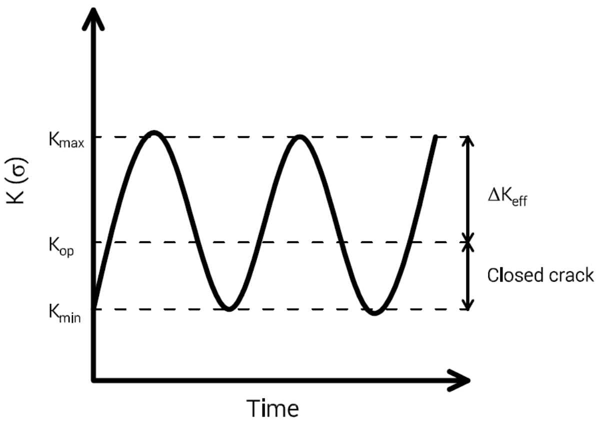

Figure 3.31. Definition of effective stress intensity range, closed crack region and load-displacement behavior for plasticity-induced closure.

The loaded crack-tip is exposed to plasticity in order to obtain equilibrium, as discussed previously. Therefore, the unloaded crack-tip contains compressive residual stresses near the crack-tip. Thus, the crack closes before the crack-tip is fully unloaded, as seen in figure 3.31.

To explain it more carefully, a test case (figure 3.32) of plasticity-induced closure is given in figure 3.33. An elastic-plastic analysis is carried out with the purpose of visualizing the residual compressive stresses which occurs near the crack-tip.

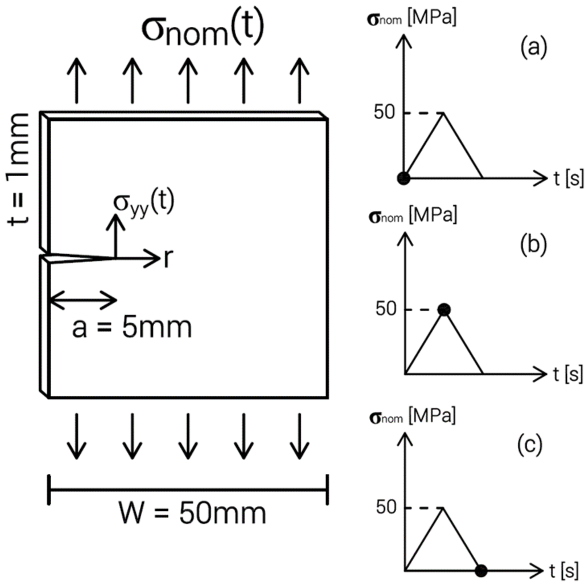

Figure 3.32. Through edge cracked test case carried out with elastic-plastic material with $E = 200GPa$ and $\sigma_Y = 235MPa$ (von mises yield criterion).

The result for each load step is plotted in figure 3.33 along with contour plots of y-direction normal stress.

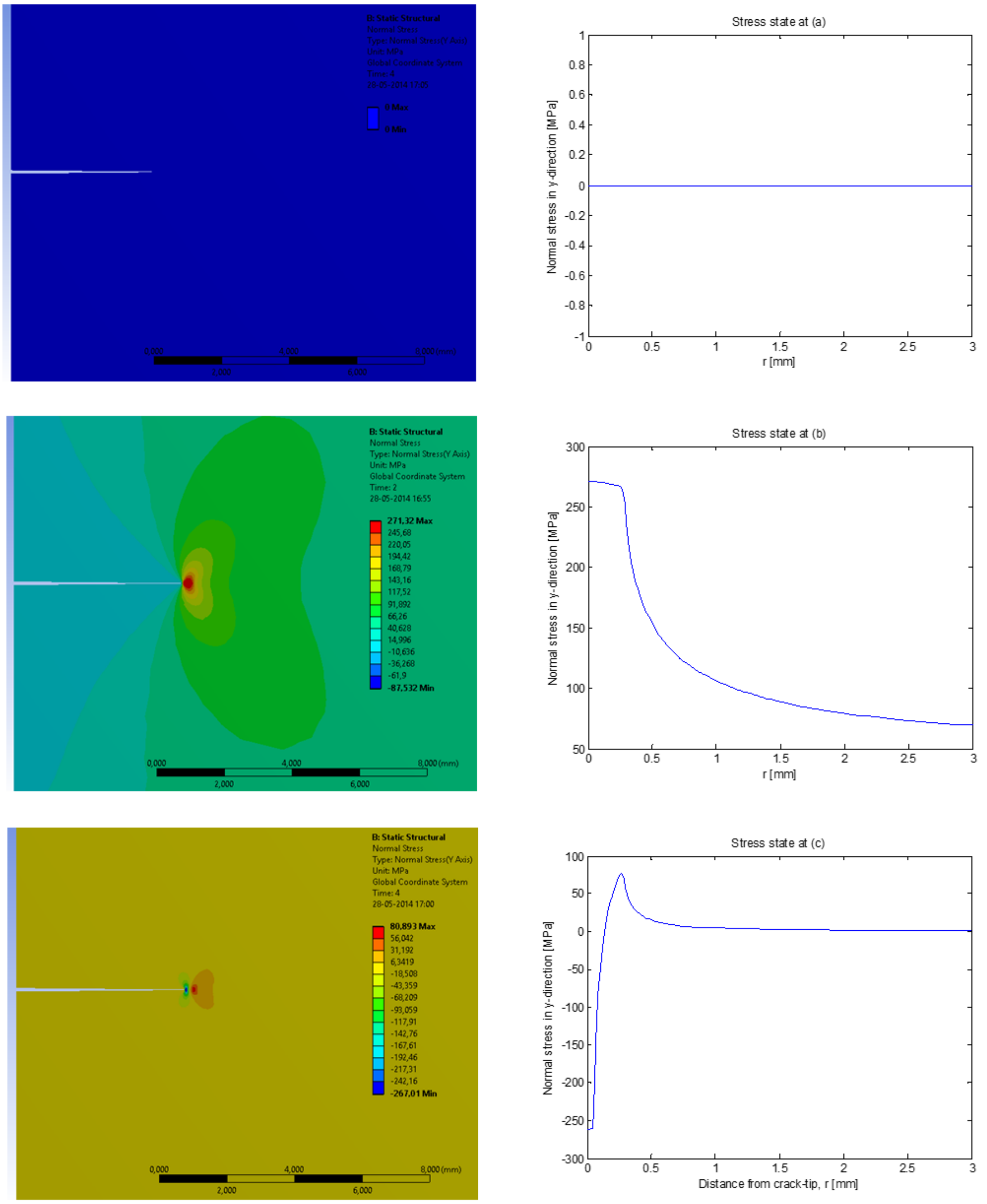

Figure 3.33. Elastic-plastic analysis (Ansys WB15.0) showing the compressive residual stresses around the crack-tip, which causes the crack to close before reaching minimum loading.

The crack closure concept is therefore used to determine an effective stress intensity factor which is less conservative. For variable loadings additional retardation is able to occur. These effects are related to overloads.

3.5.5.2 Crack growth retardation due to overloads

Fatigue loaded structures are not always perfectly cyclic loaded. In reality almost any fatigue loaded structure will be exposed to variable loading. Load history effects in homogeneous materials, like cast steel and aluminum, are graphically illustrated in figure 3.34.

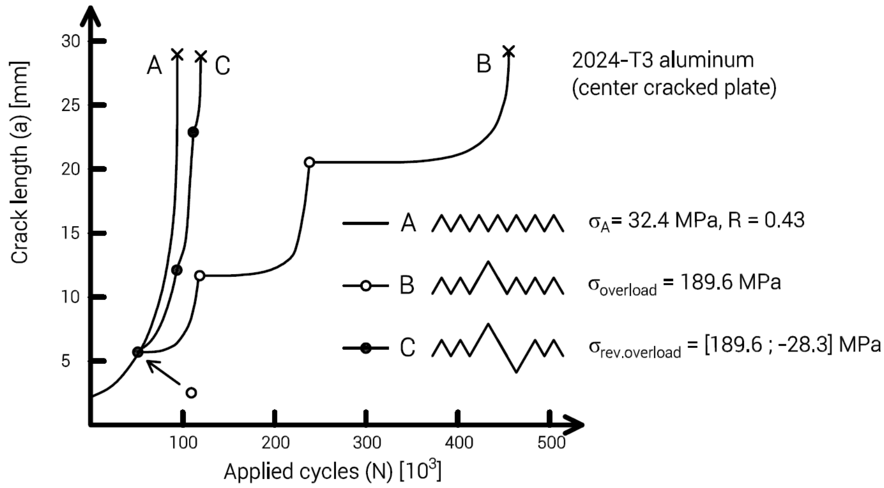

Figure 3.34. Crack growth life behavior of 2024-T3 aluminum for a (a) cyclic load, (b) cyclic load with reversed overload and (c) cyclic load with single overloading.

As discussed in the previous section, the crack closure concept affects the crack growth behavior. In figure 3.34 the single overloads retards the fatigue process, which could be rather unexpected if crack-tip plasticity was not considered. However, not all cast metals retards due to overloads. Crack growth retardation is not observed for ductile cast [Biermann 2007].

As mentioned in 3.4.1, the NASGRO equation offers the possibility of taking crack closure into consideration.

4 Numerical validation of stress intensity factors

The stress intensity factor is the governing input parameter in crack simulation algorithms. Crack propagation direction is determined based on ratios of the stress intensity factors for the three fracture modes. Additionally the incremental crack growth is also determined by the magnitude of the stress intensity factors. Thus, crack simulations are highly dependent on the accuracy of the numerical determined stress intensity factors.

In this thesis, the stress intensity factors are determined by use of a numerical method in the commercial software Ansys. The numerical method is tested against multiple theoretical problems, which serves the purpose of evaluating the solution accuracy of K_I, to ensure acceptable accuracy in crack simulation.

The following methods are used and presented individually from test case I-IV:

- Contour integral method (analytical)

  I SENB specimen

- Analytical solution [ASTM]

  I SENB specimen
  II Single edge notch tension specimen
  III Semi-circular surface crack
  IV Embedded circular crack

- Domain integral method (numerical)

  I SENB specimen
  II Single edge notch tension specimen
  III Semi-circular surface crack
  IV Embedded circular crack

The numerical method is first tested against a single edge notch bending (SENB) specimen, using three different methods. The individual calculation methods are briefly presented in the start of the corresponding sections.

4.1 Contour integral method

The contour integral method can be suitable for hand calculation and often employs certain assumptions to ease calculations. As stated previously, the J-integral can be used to compute stress intensity factors for pure mode I, II and III loadings. The J-integral is expressed as:

$$J = \int_{\Gamma} (W dy - T_i \frac{\partial u_i}{\partial x} ds) \tag{4.1}$$

Where:

W	is the strain energy density.
T_i	is the traction vector.
$\frac{\partial u_i}{\partial x}$	is the change in displacement.

The line integral is performed in a counter clockwise manner from one crack face to the other, as illustrated below:

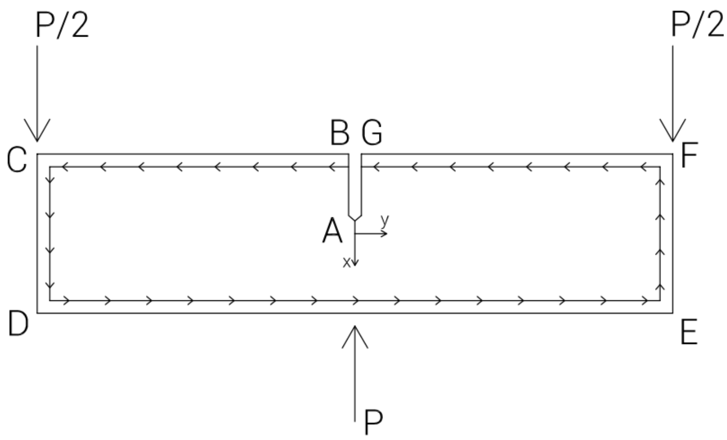

Figure 4.1. Contour path on SENB specimen.

The J-integral is a summation of the J-integrals of all the surfaces:

$$J = J_{BC} + J_{CD} + J_{DE} + J_{EF} + J_{FG} \tag{4.2}$$

The integration is path independent, which can be exploited to simplify calculations. By choosing the contour illustrated on figure 4.1, a number of assumptions can be made:

- The traction on surface BC and FG is zero because they are free surfaces.
- The traction on surface DE is negligible because the load is concentrated.
- The strain energy density on all surfaces is negligible.

These assumptions reduce the J-integral to $J = J_{CD} + J_{EF}$. Since the surfaces CD and EF are symmetric, both in terms of geometry and loading, the J-integral can further be reduced to $J = 2J_{CD}$. Explicitly written as:

$$J = 2\int_{C}^{D} (W dy - T\frac{\partial u_y}{\partial x} ds) \tag{4.3}$$

The strain energy density on surface CD is zero reducing (4.3), to:

$$J = -2\int_{C}^{D} T\frac{\partial u_y}{\partial x} ds \tag{4.4}$$

Both the traction and the slope is constant on surface CD leading to:

$$J = -2\int_{-a}^{(W-a)} T\frac{\partial u_y}{\partial x} ds = -2T\frac{\partial u_y}{\partial x} W \tag{4.5}$$

The displacement of surface CD is illustrated below:

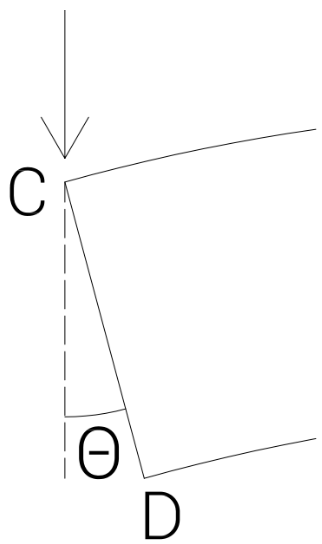

Figure 4.2. Displacement of surface CD.

As illustrated on figure 4.2, can it be seen that the displacement of surface CD has a constant slope. The specimen is regarded as a simply supported beam with a concentrated load applied at midspan. This leads to an expression of the slope on surface CD of $\theta = \frac{\partial u_y}{\partial x} = -\frac{1}{16}\frac{Pl^2}{EI} = -\frac{3}{4}\frac{Pl^2}{EB(W-a)^3}$. The traction on surface CD is $T = \frac{1}{2}\frac{P}{bh}$. These two expressions are substituted into expression (4.5), leading to the final expression of the J-integral for the specimen:

$$J = \frac{P}{bh}\frac{3}{4}\frac{Pl^2}{EB(W-a)^3}h = \frac{3}{4}\frac{P^2l^2}{EB^2(W-a)^3} \tag{4.6}$$

Recaptured from 3.2.2 the following relation is true for linear-elastic fracture mechanics:

$$\begin{aligned} J &= \frac{K^2}{E} \text{ for plane stress} \\ J &= \frac{K^2}{E}\left(1-\nu^2\right) \text{ for plane strain} \end{aligned}$$

Hence, geometry of $B = 10mm$, $W = 20mm$, $a = 5mm$ and $P = 1000N$ leads to a corresponding stress intensity of $K = \sqrt{JE} = 119.26MPa\sqrt{mm}$.

4.2 Analytical solution

For a SENB specimen the stress intensity can be determined using the following expression [Bower 2009]:

$$K = \frac{4P}{B}\sqrt{\frac{\pi}{W}}[1.6(\frac{a}{W})^{\frac{1}{2}} - 2.6(\frac{a}{W})^{\frac{3}{2}} + 12.3(\frac{a}{W})^{\frac{5}{2}} - 21.2(\frac{a}{W})^{\frac{7}{2}} + 21.8(\frac{a}{W})^{\frac{9}{2}}] \tag{4.7}$$

A geometry of $B = 10mm$, $W = 20mm$, $a = 5mm$ and $P = 1000N$ gives a corresponding stress intensity of $K = 116.73MPa\sqrt{mm}$.

4.3 Domain integral method

The stress intensity factors are calculated by means of a domain integral method, specifically the interaction integral formulation, in Ansys. The domain integral method uses area integrals for 2D problems and volume integrals for 3D problems. A typical domain definition is seen in figure 4.3.

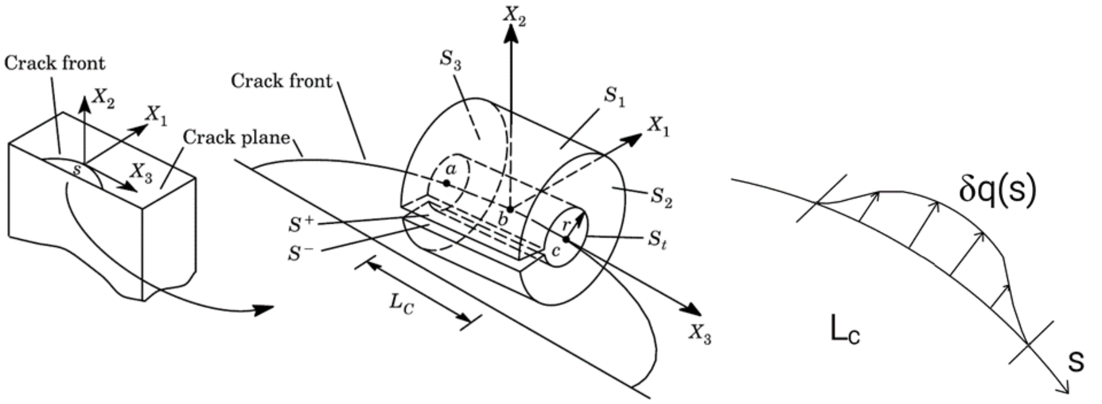

Figure 4.3. A segmental crack-front domain for computing area and volume integrals at point $s = b$ along the crack-front. The domain extends from point $s = a$ to point $s = c$ equal to the length L_c.

The idea of the interaction integral is to superimpose two equilibrium states near the crack-tip, an actual and auxiliary field. Equilibrium of the two superimposed equilibrium states leads to an interaction between the two states, which can be determined by the interaction integral as:

$$J(s)^{(act+aux)} = J(s)^{(act)} + J(s)^{(aux)} + I(s) \tag{4.8}$$

where by assuming slowly varying energy release rates within the crack front segment L_c, the same constitutive tensor couples the actual and auxiliary stress and strain components, leads to the following expressions (omitting thermal strains and crack face surface tractions):

J-integral in domain form:

$$J(s) = \frac{\overline{J}(s)}{\int_s \delta q(s) ds} = \frac{\int_V (\sigma_{ij} u_{j,1} - W\delta_{1i}) q_{,i} dV}{\int_s \delta q(s) ds} \tag{4.9}$$

Interaction integral in domain form:

$$I(s) = \frac{\overline{I}(s)}{\int_s \delta q(s) ds} = \frac{\int_V \left(\sigma_{ij} u^{aux}_{j,1} + \sigma^{aux}_{ij} u_{j,1} - \sigma_{jk} \varepsilon^{aux}_{jk} \delta_{1i}\right) q_{,i} dV}{\int_s \delta q(s) ds} \tag{4.10}$$

Where:

$\sigma_{ij}, \varepsilon_{ij}, u_i$	stress, strain and displacement components in the actual configuration
$\overline{J}(s)$	Energy released per unit advance of crack front domain L_c
$\frac{\partial u_i}{\partial x}$	is the traction vector.
$\sigma_{ij}^{aux}, \varepsilon_{ij}^{aux}, u_i^{aux}$	Stress, strain and displacement components in the auxiliary configuration
$q_{,i}$	Weight function
$\delta q(s)$	Virtual crack advance along crack front (see figure 4.3)
s	Crack front

By introducing an auxiliary solution (e.g. the near crack-tip solutions by William, the mixed mode stress intensity factors can be extracted from the following relation:

$$I(s) = \frac{2}{E'}\left(K_I K_I^{aux} + K_{II} K_{II}^{aux}\right) + \frac{1}{\mu} K_{III} K_{III}^{aux} \tag{4.11}$$

by activating the auxiliary stress intensity factors once at the time, e.g.:

$$K_I^{aux} = 1, K_{II}^{aux} = 0, K_{III}^{aux} = 0 \tag{4.12}$$

the individual activation leads to solutions of the activated mode as (4.11) simplifies to:

$$K_I(s) = \frac{E'}{2} I(s) \tag{4.13}$$

By this approach the individual stress intensity factors can be calculated by solving (4.10) using the input from (4.12) and inputting the solution into (4.13) for which:

$$E' = \begin{cases} E \text{ (plane stress)} \\ \frac{E}{1-v^2} \text{ (plane strain)} \end{cases} \tag{4.14}$$

Numerical implementation

In numerical calculations the same procedure, as just explained, is used. However, the interaction integral is evaluated numerically at each gauss point p, of every element volume V, in the considered domain segment L_c along s (illustrated in figure 4.4) by:

$$\overline{I}(s) = \sum_{V}^{elems} \sum_{p}^{gpts} \left[\left(\sigma_{ij} u_{j,1}^{aux} + \sigma_{ij}^{aux} u_{j,1} - \sigma_{jk} \varepsilon_{jk}^{aux} \delta_{1i}\right) q_{,i} \det(\mathsf{J})\right]_p w_p \tag{4.15}$$

Where:

elems	Elements within the considered domain
gpts	Gauss points within the elements of the considered domain
J	Coordinate Jacobian matrix
w_p	Gauss integration weight factor for point p

The first calculated domain, which Ansys names contour 1, is within the elements connected to the crack-tip node(s), see figure 4.4. The second domain, or contour 2, is within the elements adjacent to the elements within contour 1. This principle proceeds until the requested number of contours are reached.

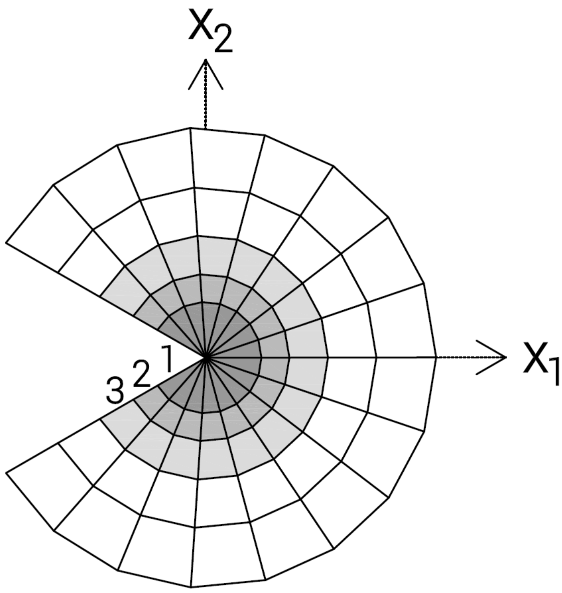

Figure 4.4. The first three contours related to the crack-tip node.

Using the near crack-tip 2D solution by Williams, as the auxiliary equilibrium state may lead to incorrect solutions. For curved crack fronts these solutions do not hold, as they are determined for a straight crack front. However, calculating the interaction integral in small enough segments L_c along the crack front s, the solutions are acceptable.

The complex nature of high stress gradients, near the crack-tip, requires considerations regarding the crack-tip mesh, which are discussed in the following.

4.3.1 Mesh considerations

Adaptive meshing, offered by many commercial codes, may lead to problems near discontinuities. Hence, considerations regarding crack-tip mesh configurations are to some extent needed. A refined adaptive mesh yields acceptable solutions, but two other mesh configurations are tested in order to lower the total amount of elements used.

4.3.1.1 Crack-tip singularity

The crack-tip singularity may be well described by using modified quadratic elements, also known as singularity elements or quarter point elements (QPEs). See figure 4.5.

To obtain an improved solution of the first contour, the singularity elements are introduced. In plane problems straight sided quadratic triangles with skewed midside nodes and element edge length $L < \frac{a}{8}$ are recommended [FERNANDO C. M. MENANDRO & LIEBOWITZ]. The rest part of the specimen is recommended to be meshed by quadratic triangles.

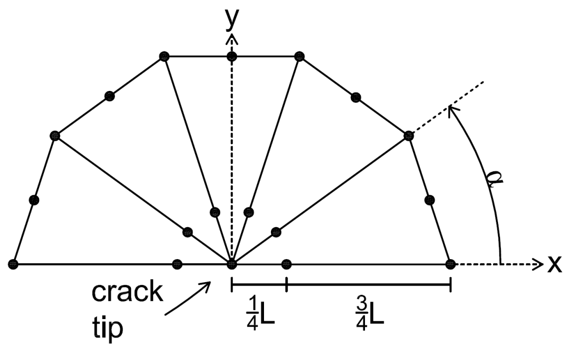

Figure 4.5. Geometrical description of the singularity elements.

By skewing the midside nodes of the quadratic isoparametric elements to a distance of $x = l/4$ from the crack-tip, the stress and strain field varies with $\frac{1}{\sqrt{x}}$. This is equal to the $\frac{1}{\sqrt{r}}$singularity predicted by the near crack-tip stress field solutions (3.5).

Using QPEs the K solution is at the first contour is improved. The impact of using singularity elements are tested in combination with a validation of a standardized crack-tip mesh configuration, proposed for the crack simulation algorithm.

4.3.2 Numerical validation of mode I stress intensity factors

A brief evaluation of three different crack-tip mesh configurations are presented in this section. The objective is to test the accuracy of the proposed crack-tip mesh configurations. The SENB specimen, seen in figure 4.6, is used again for comparison reasons.

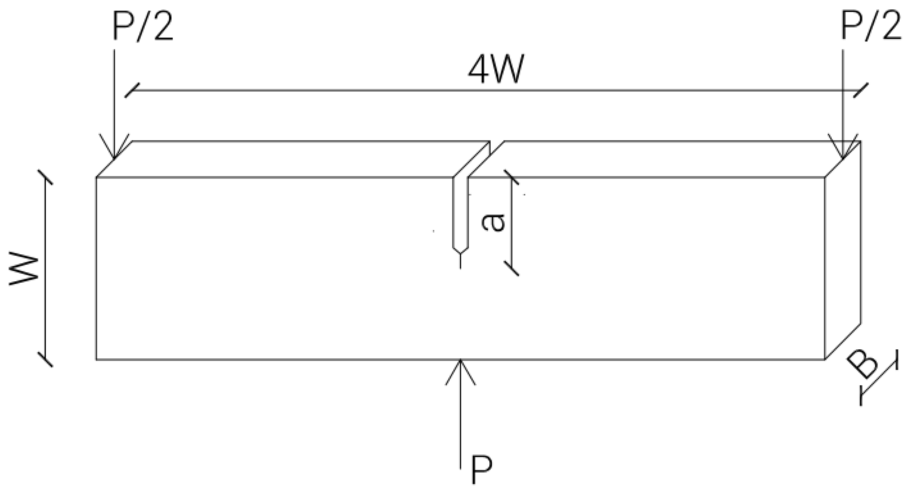

Figure 4.6. SENB specimen where$W = 20mm$, $B = 10mm$, and $a = 5mm$ $P = 1000N$.

The mode I stress intensity factor is determined by means of domain integral method, executed by CINT in Ansys MAPDL. Results are plotted at six contours around the crack-tip. Before discussing the results, the different mesh configurations are illustrated in figure 4.7 and 4.8.

4.3.2.1 Refined mesh configuration

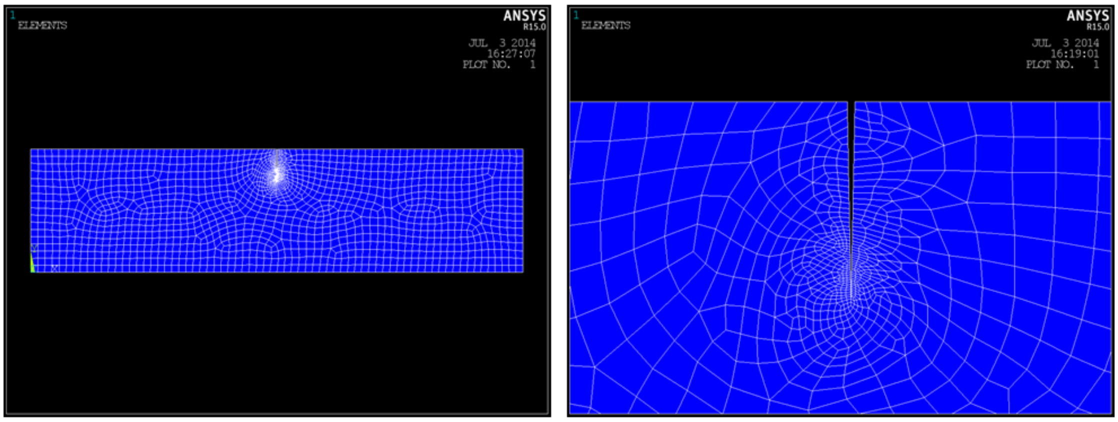

Figure 4.7. SENB specimen meshed by AMESH and then refined by SMRT in Ansys MAPDL.

A great number of quadratic quadrilaterals are used in the refined mesh configuration in figure 4.7, which is expected be able to predict the singular behaviour rather accurate. The stress intensity factors determined with the refined mesh is plotted in figure 4.7.

4.3.2.2 Modified mesh configuration

The base mesh of the modified mesh configuration is seen in 4.8.

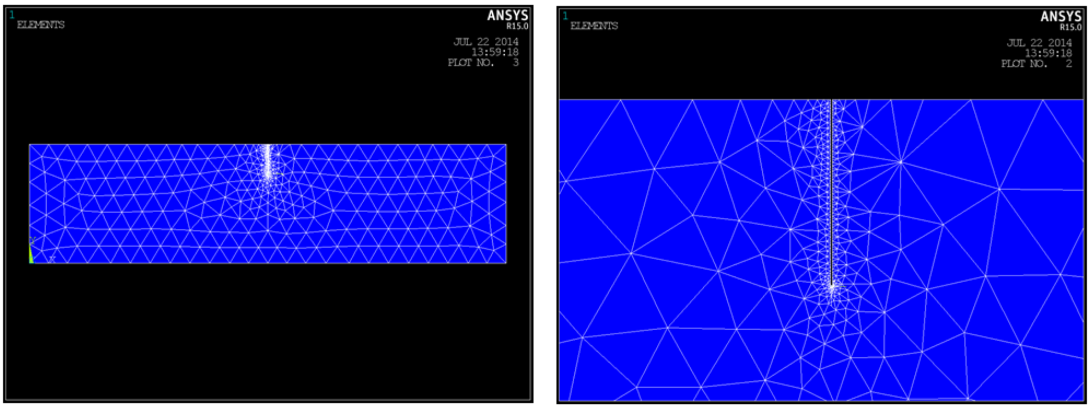

Figure 4.8. SENB specimen meshed with singularity elements by KSCON and adaptive meshing AMESH with quadratic triangles.

As noticed in figure 4.8 the amount of elements are decreased significantly compared to the refined base mesh in figure 4.7.

The modified crack-tip mesh is geometrically schematized in figure 4.9.

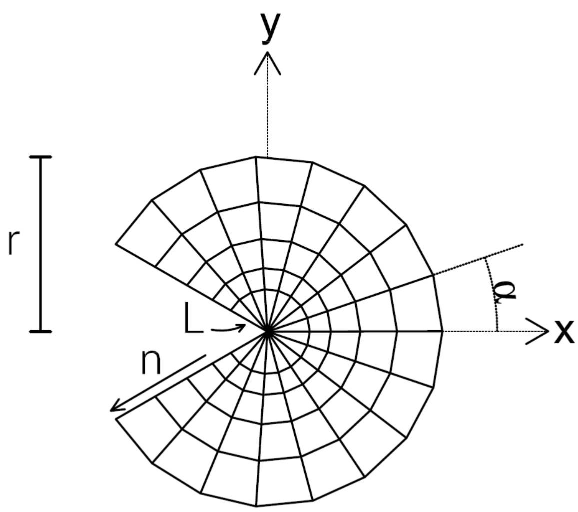

Figure 4.9. Geometrical schematization of the modified crack-tip mesh pattern, where L is the triangular element edge length, r is the crack-tip mesh pattern radius, is the spacing ratio and n is the total number of radial element layers.

In this test the crack-tip mesh, which is schematized in figure 4.9, have the following geometrical layout:

- $L = 0.0075mm$
- $r = 0.03mm$
- $\alpha = 18.75°(16 \text{ divisions})$
- $n = 5$

The layout of the crack-tip mesh, illustrated in figure 4.10 and 4.11, is generated on basis of recommended crack-tip mesh design [FERNANDO C. M. MENANDRO & LIEBOWITZ].

With quarter point elements

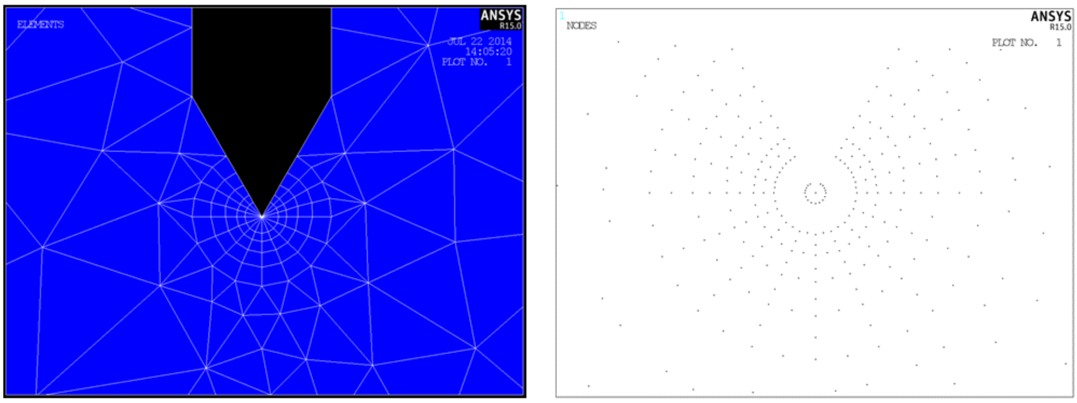

Figure 4.10. The crack-tip mesh for the modified mesh configuration and corresponding nodal points for the mesh with quarter point elements.

Noticing the inner midside nodes are shifted towards the crack-tip.

Without quarter point elements

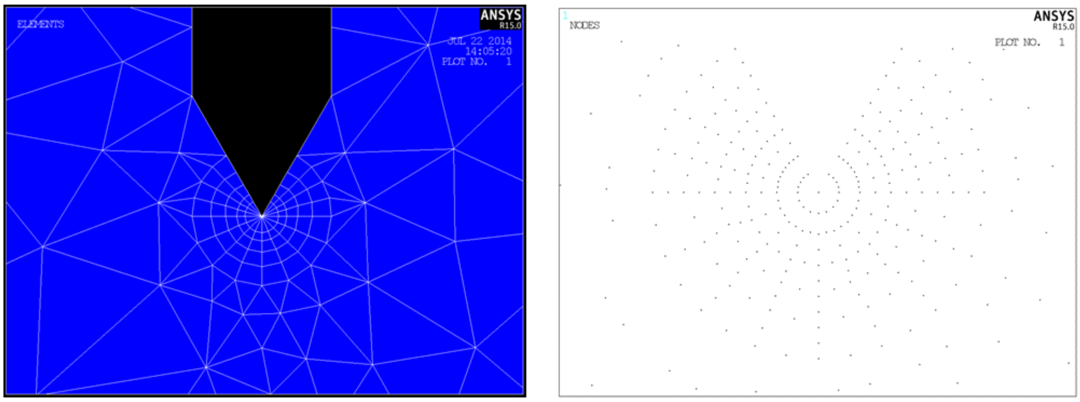

Figure 4.11. The crack-tip mesh for the modified mesh configuration and corresponding nodal points for the mesh without quarter point elements.

Here the midside nodes of the inner triangles are kept in the middle.

The mode I stress intensity factors for the SENB specimen are plotted in figure 4.12.

4.3.2.3 Discussion

The results are plotted in figure 4.12 and the deviation of the averaged stress intensity factors (neglecting the first contour) are listed in table 4.1.

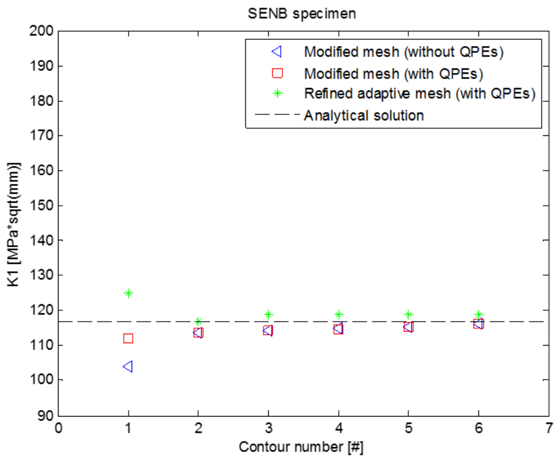

Figure 4.12. Numerical K_I solutions for the SENB specimen in relation to the analytical solution.

Noticing the first contour in figure 4.12 is the most inaccurate solution for all three mesh configurations. Expectedly the mesh configuration with quarter point elements are closest to the analytical solution at the first contour.

The inaccurate solution occur due to crack-tip singularity. Hence, the solutions of first contour is neglected.

Mesh configuration	Deviation from analytical solution [%]	Number of elements
Refined adaptive mesh	1.39	1769
Modified mesh (with QPEs)	-1.64	1098
Modified mesh (without QPEs)	-1.56	1098

Table 4.1. Comparison of averaged (contour two to six) K_I results for the SENB specimen.

All three mesh configurations show solutions within 2% of the analytical solution as seen in table 4.1, which validates the numerical solutions of all three mesh configurations. Next to this, the result obtained with the refined adaptive mesh configuration utilizes 60% more elements. Hence, in the following numerical models the modified mesh without QPEs are used and the first contour is neglected.

Numerical validation of 2D problem solved by a numerical 3D model

In the present section, a theoretical 2D problem is solved by means of a finite element model in 3D. The purpose is to test if the numerical solution, in 3D, results in reasonable magnitudes of K_I. The evaluated problem is illustrated in figure 4.13.

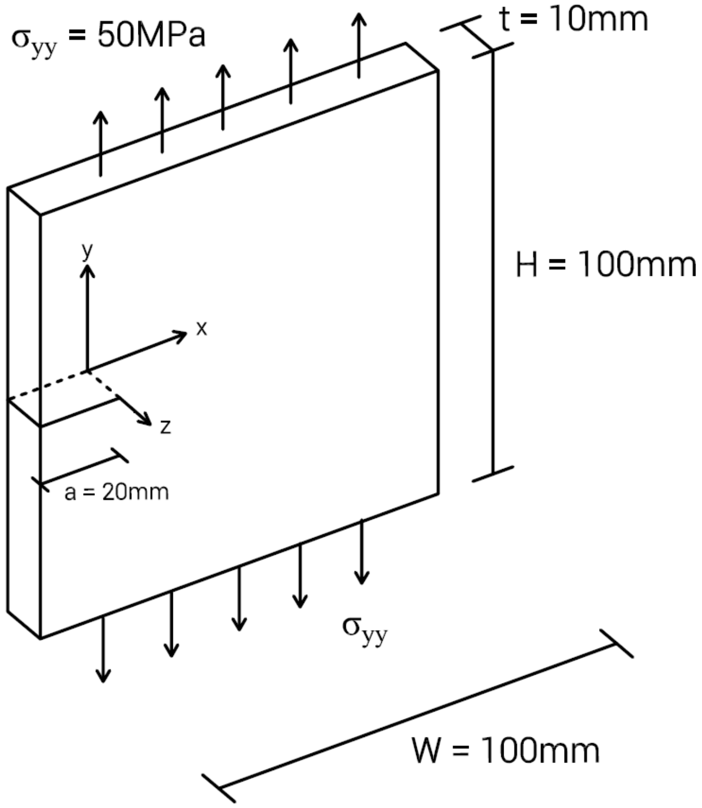

Figure 4.13. Single edge notch specimen with $E = 2.1 \cdot 10^5 MPa$ and $\nu = 0.3$.

Mode I stress intensity factor is determined through thickness by the domain integral method in ANSYS Mechanical APDL and compared to the analytical solution. The base mesh is illustrated in figure 5.5 and the local crack-tip mesh in figure 5.14.

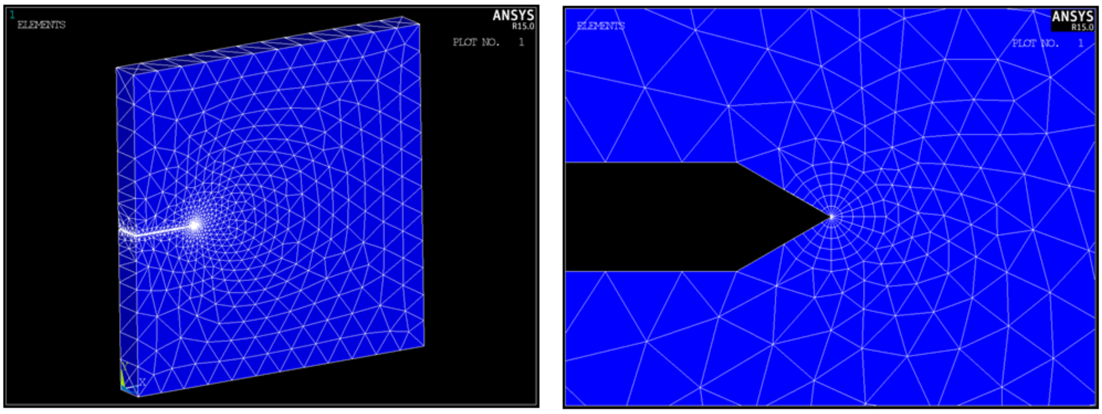

Figure 4.14. Base mesh and closeup of the crack-tip mesh connected to the base mesh. Quadratic tetrahedrons are used for the base mesh.

The crack-tip mesh configuration, presented in the previous chapter, is extruded and tested for different number of element divisions through specimen thickness.

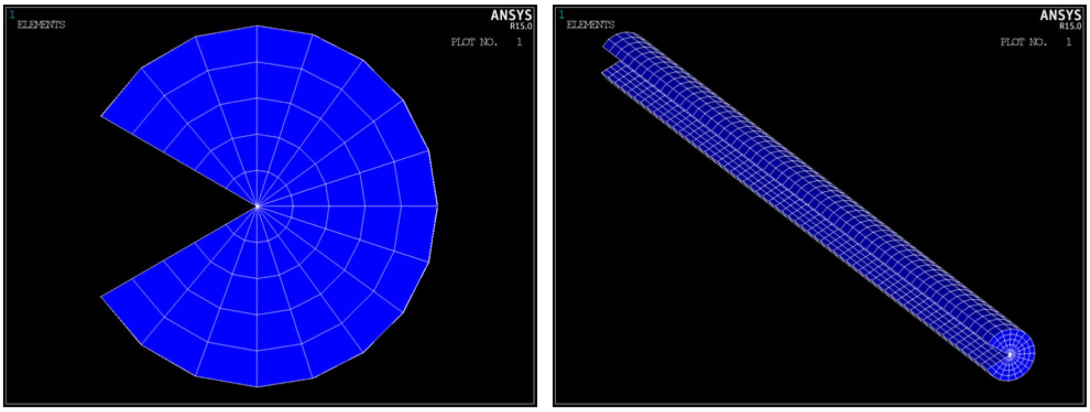

Figure 4.15. Crack-tip mesh configuration with $r = 0.25mm$, $n = 5$, $\alpha = 18.75°$ and L is automatically determined by the VSWEEP command. The discretized crack-tip volume, to the right, is with 60 element divisions in the thickness direction.

The solutions of K_I are plotted in figure 4.16.

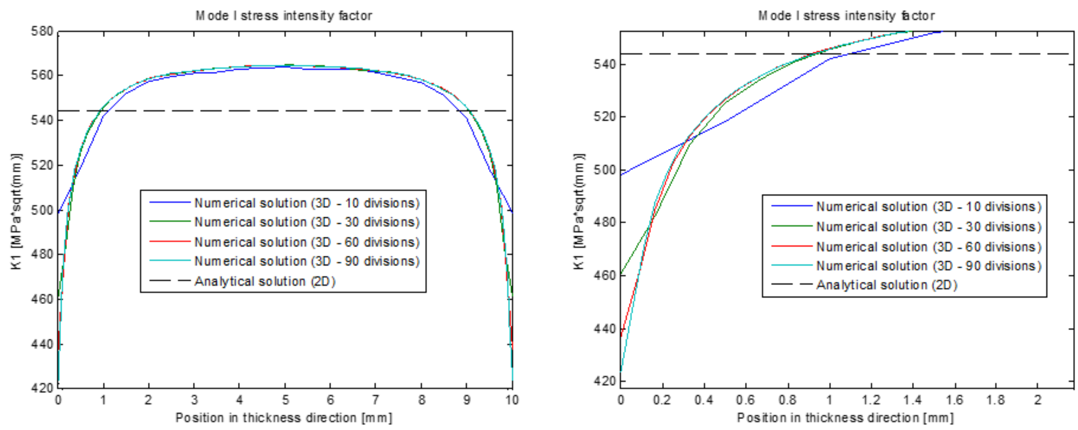

Figure 4.16. Analytical solution versus numerical solutions with different element divisions in the thickness direction (z) and close up of the near edge results of the single edge notch specimen.

The numerical solutions of K_I is converged at 60 element divisions through thickness and has magnitudes of reasonsable level comparatived to the analytical solution in 2D.

Numerical validation of semi-circular surface crack

A semi-circular surface crack problem is tested with the finite element method and compared to an analytical solution proposed by Newman and Raju[appendix 1]xx. The problem is illustrated in figure 4.17.

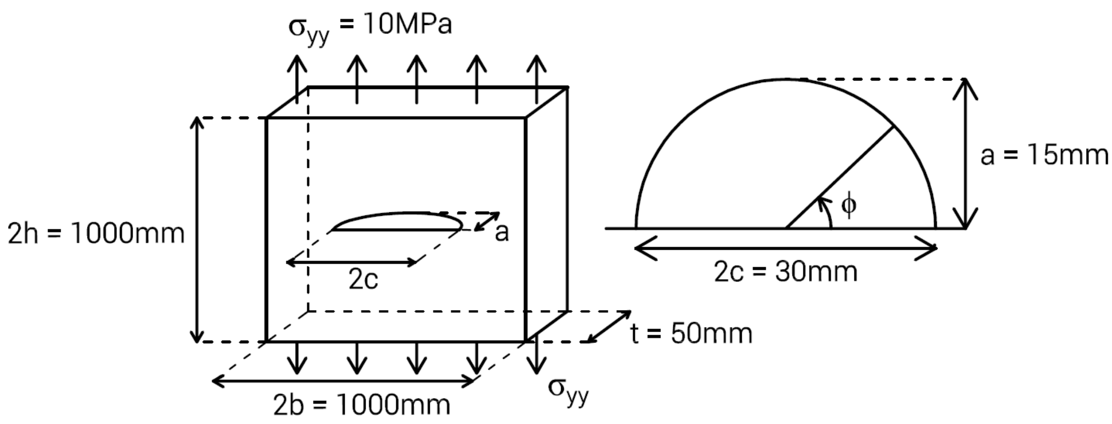

Figure 4.17. Semi-circular surface crack in a body with geometrical parameters $\frac{a}{c} = 1$,$\frac{a}{t} = 0.3$ and $\frac{c}{b} = 0.03$. The material parameters are assumed to be $E = 2.1 \cdot 10^5 MPa$ and $\nu = 0.3$.

The body is meshed with quadratic tetrahedrons, whereas the crack-tip mesh is a combination of quadratic hexa- and tetrahedrons. Base mesh is illustrated in figure 4.18.

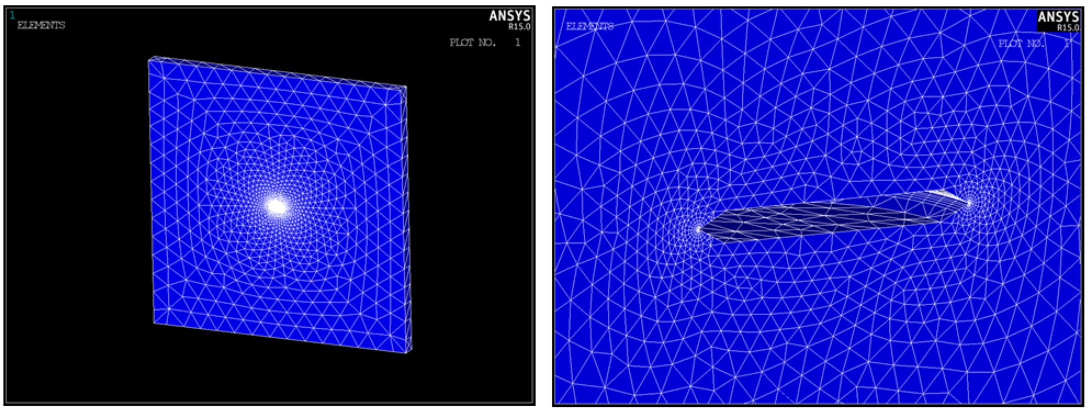

Figure 4.18. Base mesh of semi-circular crack problem and implemented semi-circular crack geometry.

A close up of the crack-tip mesh is shown in figure 4.19. Different number of element divisions are tested along the crack front.

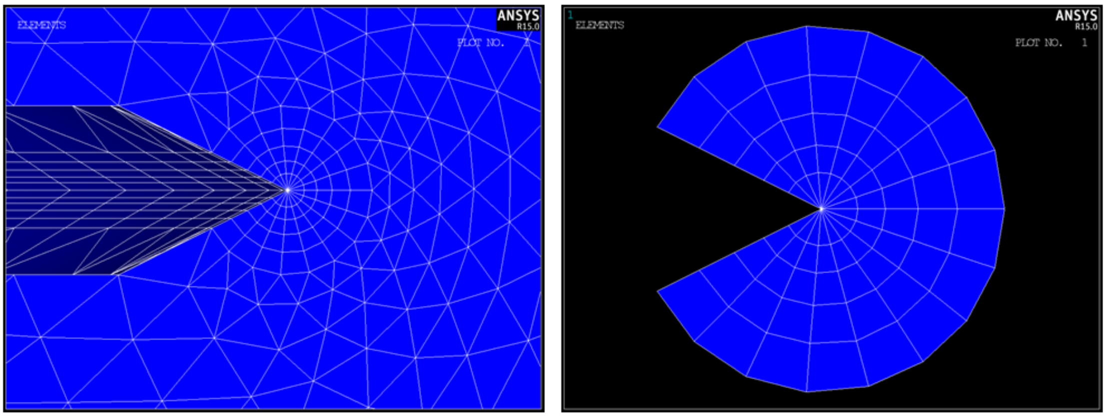

Figure 4.19. Crack-tip mesh configuration with r=1.5mm, n=5, $\alpha = 18.75°$ and L=0.3mm.

The tested crack-tip mesh configurations are illustrated in figure 4.20.

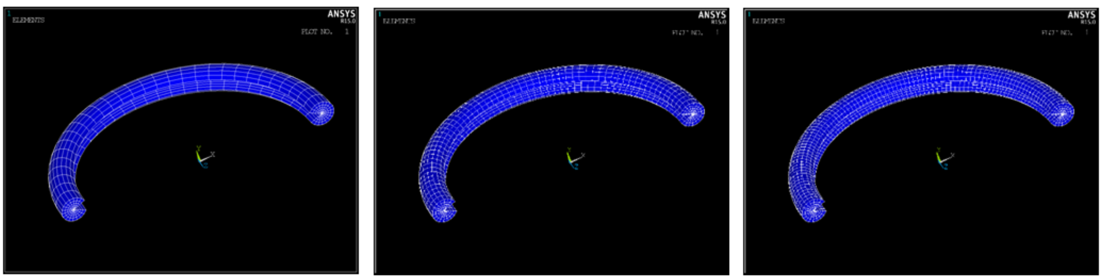

Figure 4.20. Different number of element divisions around the circumference of the semi-circular surface crack. The three tested number of element divisions are 30, 60 and 90, which is shown from left to right.

The mode I stress intensity factor is numerically solved for the different crack-tip mesh layouts in figure 4.20 and plotted in figure 4.21 in relation to the analytical solution.

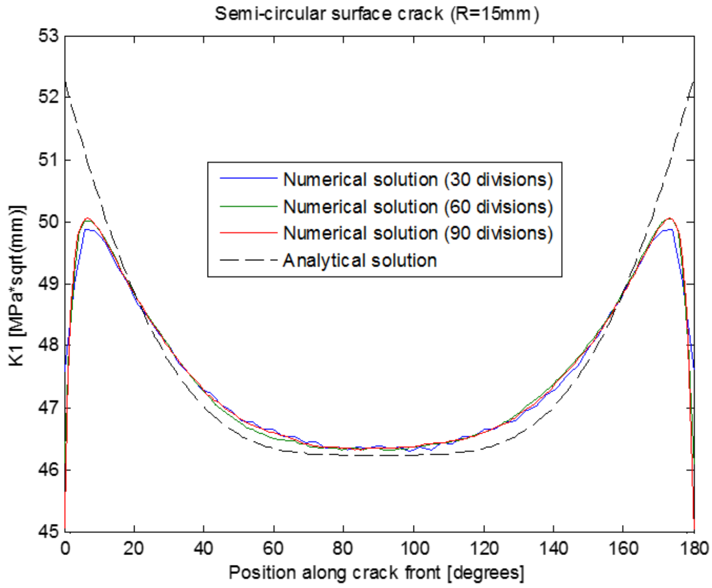

Figure 4.21. Analytical solution of K_I compared to numerical solutions.

The numerical solution is converged at 60 element divisions around the semi-circular crack front. By plotting the K_I solution close to the free surface, in figure 4.22, a drift is noticed towards the free surface.

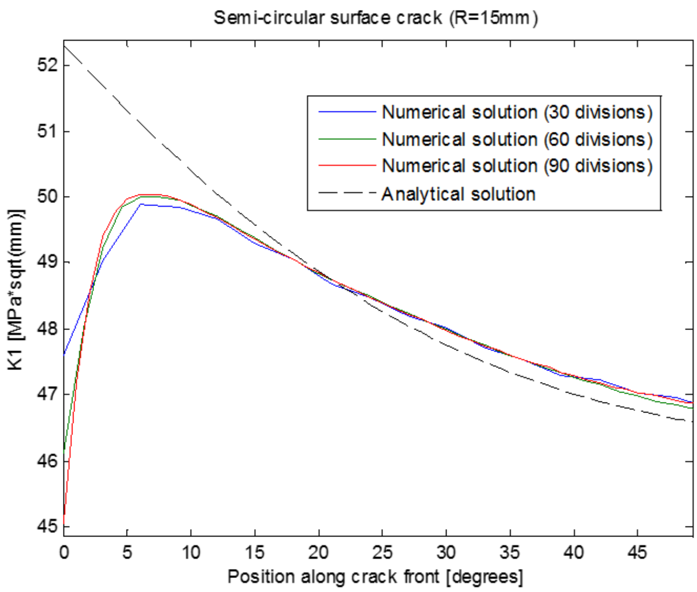

Figure 4.22. The numerical solution drifts away from the analytical solution near the free surface.

Linear extrapolation can be introduced in order to obtain more accurate solutions near the free edges, in order to use the results in a crack propagation simulation.

An example is given in figure 4.23, where the numerical solution(90 divisions) from figure 4.22 is extrapolated.

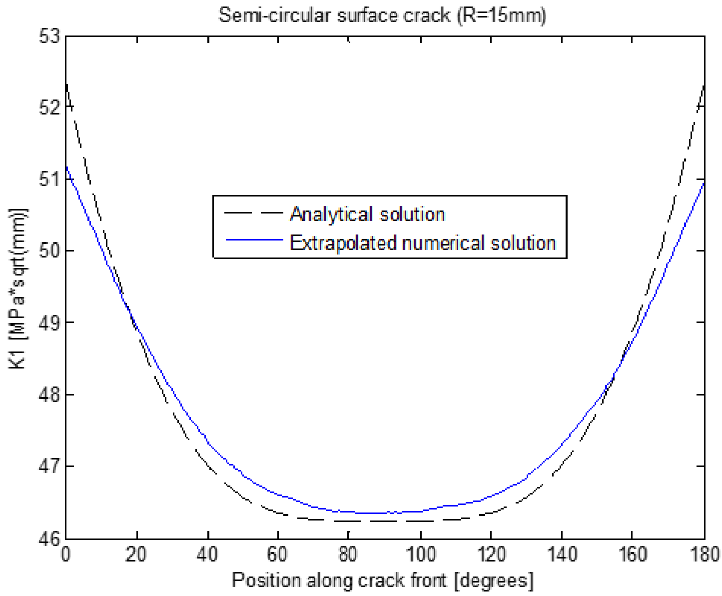

Figure 4.23. Linear extrapolation of the numerical solution.

As noticed in figure 4.23, the extrapolated numerical solution is close to the analytical. The deviation is graphically illustrated in figure 4.24.

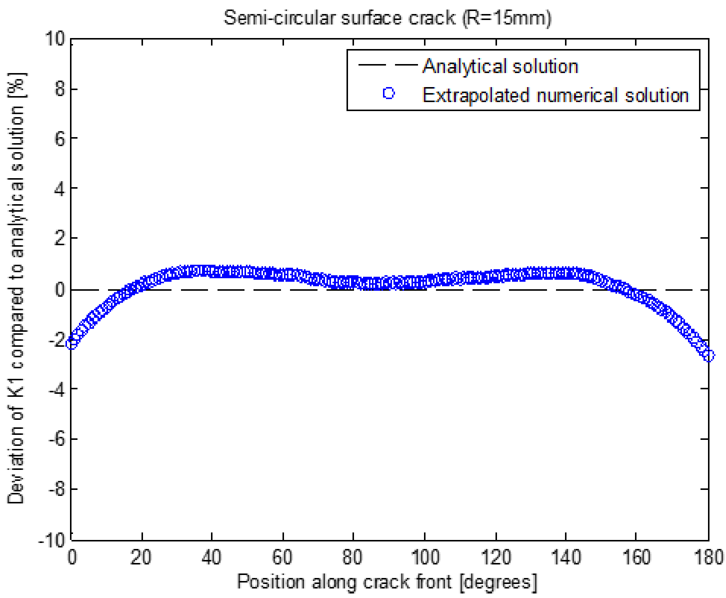

Figure 4.24. Deviation of extrapolated numerical solution in relation to the analytical solution.

The extrapolated numerical solution is within 3% of the analytical solution. Hence, mode I stress intensity factors for a semi-circular crack, is acceptably determined by the domain integral method used in this thesis.

For simulation of surface cracks with the domain integral method used in this thesis, linear extrapolation is recommended.

Numerical validation of embedded circular crack

The mode I stress intensity factors of a embedded circular crack are determined numerically and compared to the analytical solution proposed by Irwin[REF APPENDIX 1]xx. The evaluated problem is illustrated in figure 4.25.

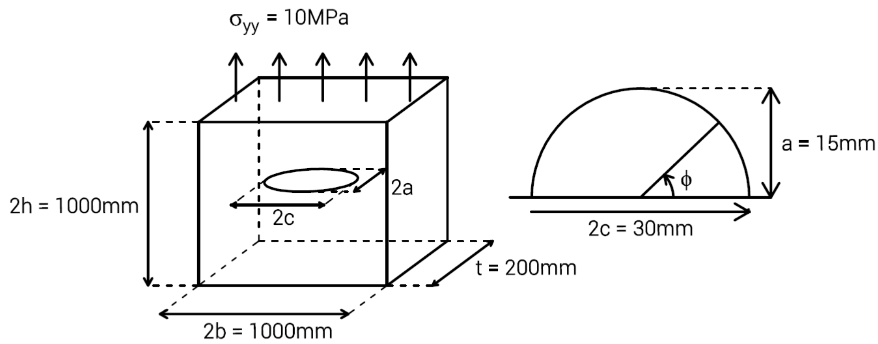

Figure 4.25. Embedded circular crack in a body with geometrical parameters $a, c \ll t, h, b$ and $\frac{a}{c} < 1$. The material parameters are assumed to be $E = 2.1 \cdot 10^5 MPa$ and $\nu = 0.3$.

The numerical model is illustrated in figure 4.26, which shows the base mesh and the embedded circular crack by a wireframe plot of the volumes.

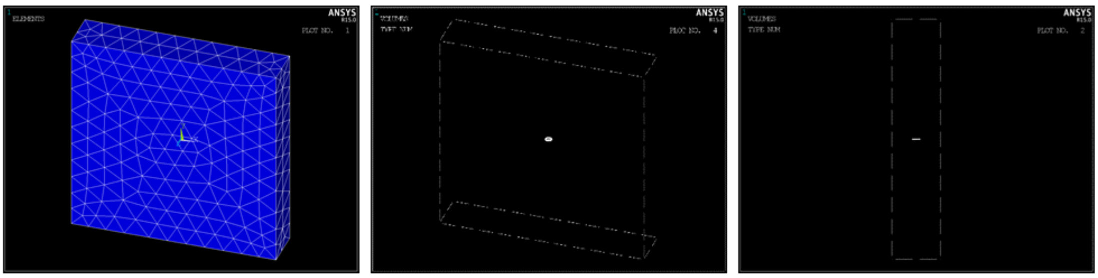

Figure 4.26. Base mesh and wireframe plot of volumes used to model the embedded circular crack problem.

As in the previous three-dimensional numerical models, a crack-tip mesh configuration was introduced and extruded around the crack front. This is illustrated in figure 4.27.

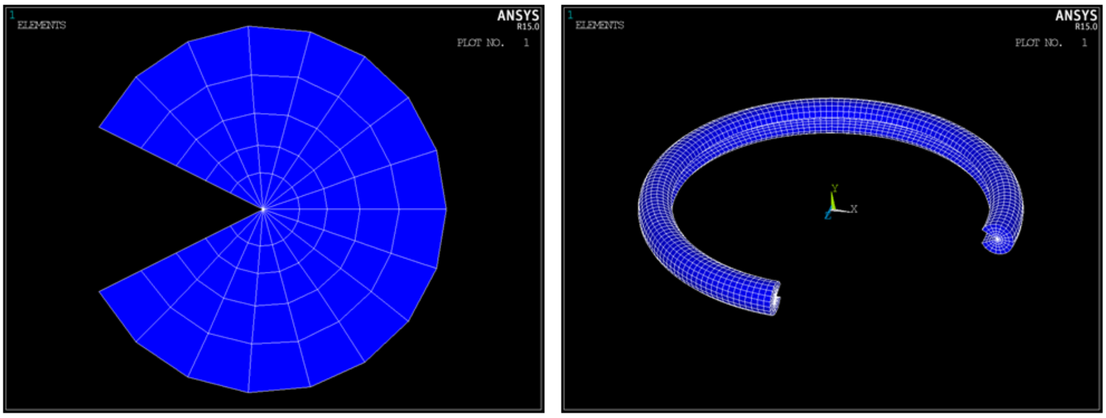

Figure 4.27. Crack-tip mesh configuration with r=1.5mm, n=5, $\alpha = 18.75°$, L=0.3mm and 90 element divisions along the crack front (illustrated from $\phi = 0° \rightarrow 270°$).

The stress intensity factors for mode I are plotted in figure 4.28. The numerical solutions seams reasonable, but has spikes at each end node of the evaluated crack front path. This tendency was shown no matter if K_I was calculated along 90° , 180° or 270°, always at the end nodes of the evaluated crack front path.

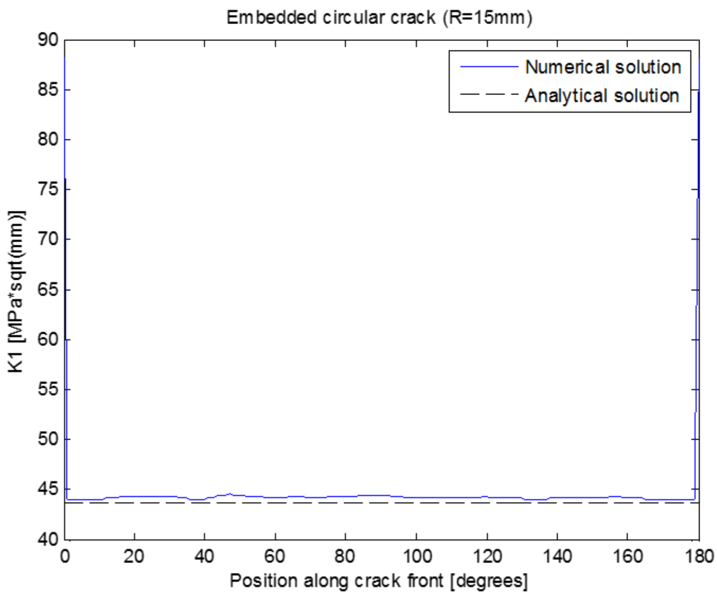

Figure 4.28. Analytical solution of K_I compared to numerical solution.

These spikes makes no physical sense, and therefore the numerical solution can be extrapolated in order to obtain realistic results. The first and last node is extrapolated on basis of the solution gradient of the adjacent node. The extrapolated solution is plotted in figure 4.29.

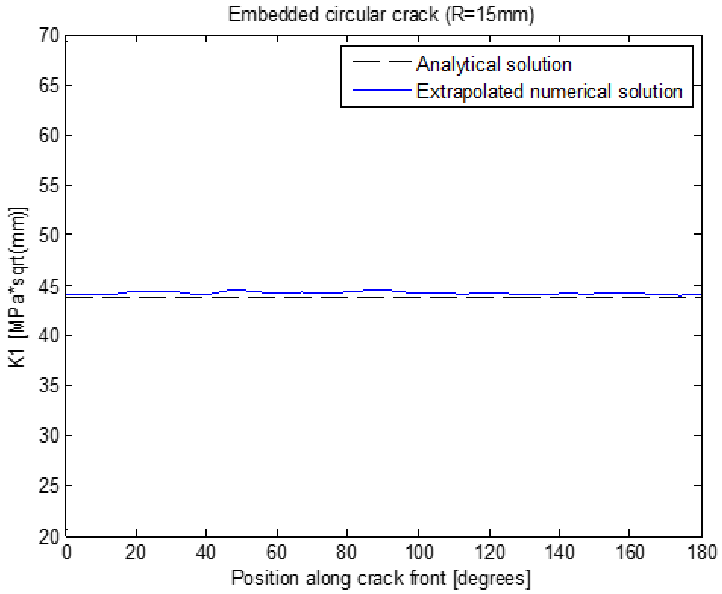

Figure 4.29. Linear extrapolation of the numerical solution.

The extrapolated numerical solution is evaluated in percentage against the analytical solution in figure 4.30.

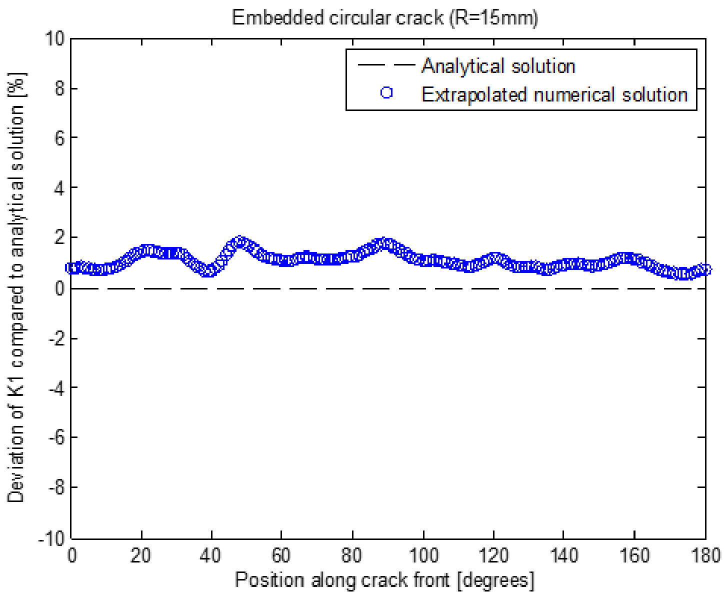

Figure 4.30. Deviation of extrapolated numerical solution in relation to the analytical solution.

The extrapolated numerical solution is, as expected, almost constant and within 2% of the analytical solution. Hence, mode I stress intensity factors for an embedded circular crack, is acceptably determined by the interaction integral used in this thesis.

4.3.2.4 Discussion of numerically determined stress intensities

Errors in calculation of stress intensity factors have the potential of making lifetime estimations imprecise.

In figure 4.31 is the impact of numerical calculation errors on a lifetime prediction illustrated. A numerical model is tested against an analytical solution on a problem, for which the crack is assumed to grow in a self-similar manner. [Biermann 2007]. The the tested specimen is a SENB specimen with the following measurements $B = 10mm$, $W = 20mm$, $a_i = 5mm$. The crack growth parameters are given in table 4.2.

Model	C	n	K_c	p	q	ΔK_1	C_{th}^+	C_{th}^-	α
Forman	$7.00 \cdot 10^{-12}$	2.49	1049.88						
Nasgro	$6.19 \cdot 10^{-15}$	3.80	1049.88	0.40	0.40	111.5	2.6	0.1	2.5

Table 4.2. Crack growth parameters.

The applied load is $\Delta P = 1719N$with a load ratio of $R = \frac{3089}{4808} = 0.6425$. The results are illustrated on figure 4.31.

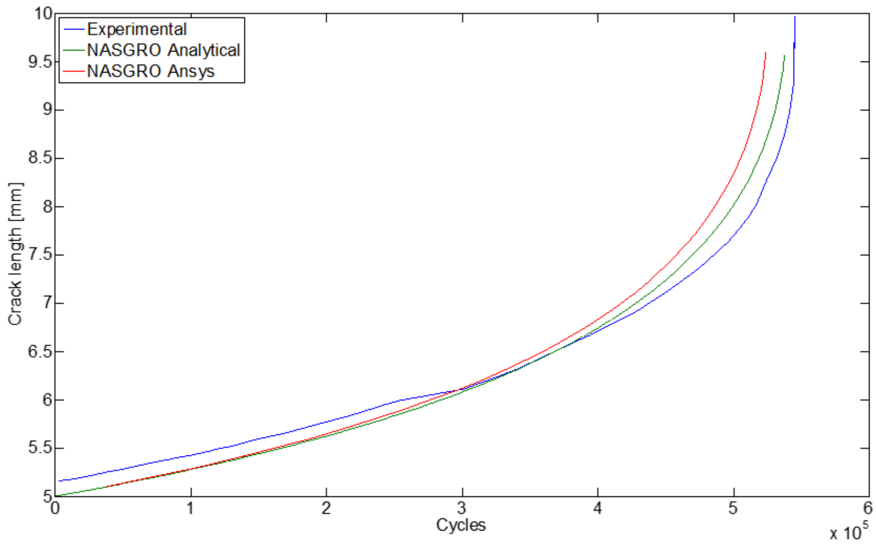

Figure 4.31. Comparison of experimental crack growth against analytical and numerical determined crack growth. [Biermann 2007]

From figure 4.31 is it clear that the lifetime simulations from the analytical and numerical model, are very close to the experimental result, with a deviation from the experimental result of 1.4% and 3.9% respectively. The numerical prediction is slightly more conservative than the analytical, which is expected since the stress intensities, produced by the numerical model, is higher than the analytical solution.

The results emphasize that the domain integral method, in Ansys, is a reasonable method for determining stress intensities.

Crack propagation direction 5

In this section crack direction models are reviewed on basis of experiments.

5.1 Crack propagation criterions

The crack direction models in focus, is the maximum tangential stress(MTS) [F. Erdogan 1963] criterion and Richard's criterion [H.A. Richard M. Fulland 2005]. MTS is a well-established criterion for mode I + II, where Richards's criterion is a relatively new criterion, which is able to take all three modes into account and is easy to implement in numerical solutions.

5.1.1 Maximum tangential stress criterion

The MTS criterion is derived from observations of the complex stress situation near the crack-tip. The near-field stress situation is illustrated on figure 5.1.

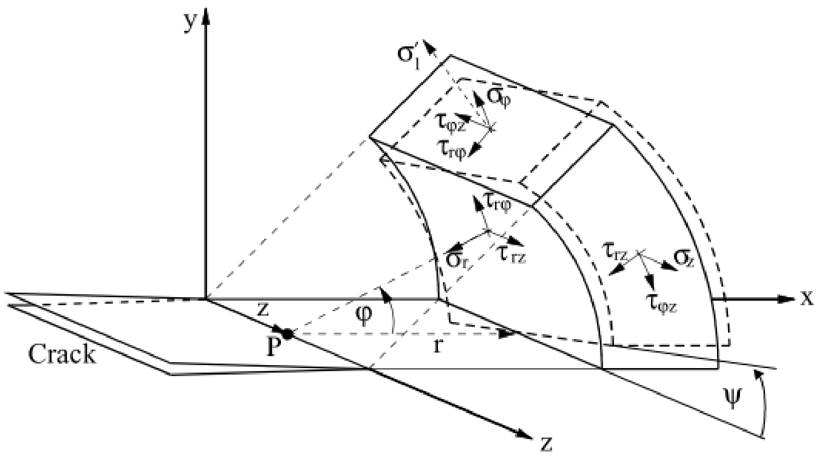

Figure 5.1. Near-field stress situation.

The near-field stresses are given as:

$$\sigma_r = \frac{K_I}{\sqrt{2\pi r}} {f_r}^{I}(\varphi) - \frac{K_{II}}{\sqrt{2\pi r}} {f_r}^{II}(\varphi) \tag{5.1}$$

$$\sigma_\varphi = \frac{K_I}{\sqrt{2\pi r}} {f_\varphi}^{I}(\varphi) - \frac{K_{II}}{\sqrt{2\pi r}} {f_\varphi}^{II}(\varphi) \tag{5.2}$$

The MTS criterion is based on the assumption that the crack will propagate in the direction perpendicular to the maximum tangential stress. By maximizing (5.2) as:

$$\frac{\partial \sigma_\varphi}{\partial \varphi} = 0 \ \frac{\partial^2 \sigma_\varphi}{\partial \varphi^2} < 0 \tag{5.3}$$

The crack propagation angle can be determined by isolation of ϕ :

$$\varphi = -\arccos\left(\frac{3K_{II}^2 + K_I\sqrt{K_I^2 + 8K_{II}^2}}{K_I^2 + 9K_{II}^2}\right) \tag{5.4}$$

Where $\varphi > 0$ for $K_{II} < 0$ and $\varphi < 0$ for $K_{II} > 0$.

5.1.2 Richard's criterion

Richard's criterion

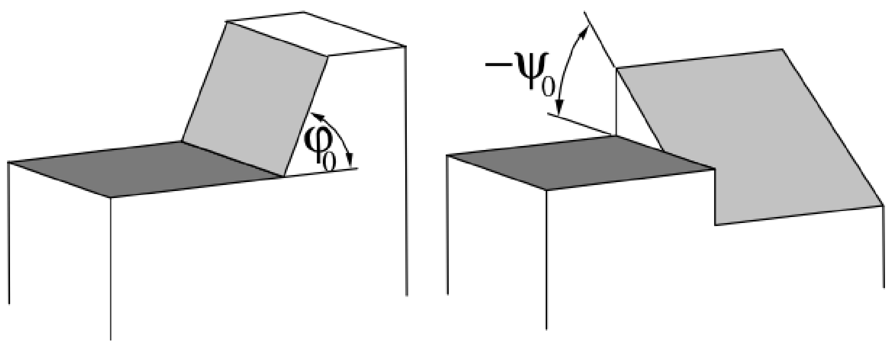

Figure 5.2. Angles predicted by Richard's criterion.

The angles from Richard's criterion are given as:

$$\varphi = \left[140^\circ \frac{|K_{II}|}{K_I + |K_{II}| + |K_{III}|} - 70^\circ\left(\frac{|K_{II}|}{K_I + |K_{II}| + |K_{III}|}\right)^2\right] \tag{5.5}$$

Where $\varphi > 0$ for $K_{II} < 0$ and $\varphi < 0$ for $K_{II} > 0$.

$$\psi = \left[78^\circ \frac{|K_{III}|}{K_I + |K_{II}| + |K_{III}|} - 33^\circ\left(\frac{|K_{III}|}{K_I + |K_{II}| + |K_{III}|}\right)^2\right] \tag{5.6}$$

Where $\psi > 0$ for $K_{III} < 0$ and $\psi < 0$ for $K_{III} > 0$.

5.2 Case study: Mode I and II

The purpose of this experiment is to test the usage of MTS and Richard's criterion for a mode I + II situation. The main area of focus is to compare Richard's criterion with MTS, and validate the usage of Richard's criterion.

Three specimens have been tested, they are illustrated on figure 6.1. The overall dimensions and boundary conditions are identical but the position and length of the initial crack is varying. The crack has a width of 0.05 in. The cracks are offset from the centerline, which causes both mode I + II be activated. The crack growth path is influenced by the holes in the plate, as the decreased stiffness act as an attractor for the cracks propagation.

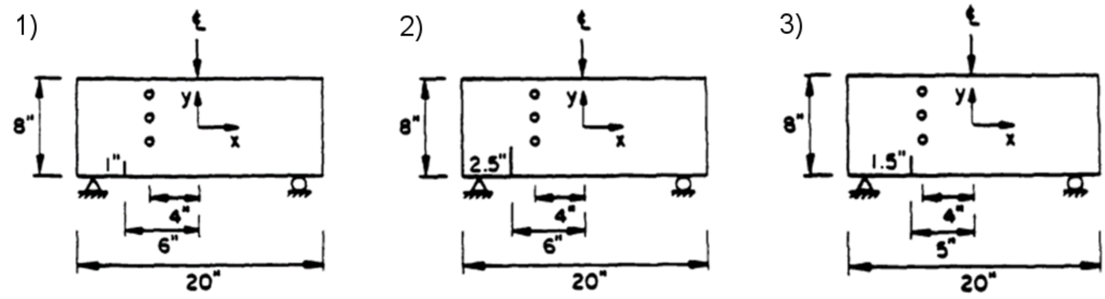

Figure 5.3. Dimensions of specimens. t=0.5 in.

The material data of the specimens are given in table 5.1.

Material type	Plexiglas Poly(methyl methacrylate)
Young's modulus	$473.000psi$
Poisson's ratio	0.3
Fracture toughness	$944lbf \cdot in^{3/2}$

Table 5.1. Material data.

The specimens were loaded monotonically with crack mouth opening displacement(CMOD) control using very small increments.

To describe the behavior of the three specimens, 2D and 3D FEM models have been set up in Ansys. The 2D model employ the MTS criterion where the 3D model employs Richard's criterion.

The boundary conditions have been setup to emulate the experiments as close as possible. To avoid stress singularities at the supports influencing the stresses at the crack tip, the boundary conditions have been applied on the entire height of the specimen. The boundary conditions are illustrated on figure 5.4.

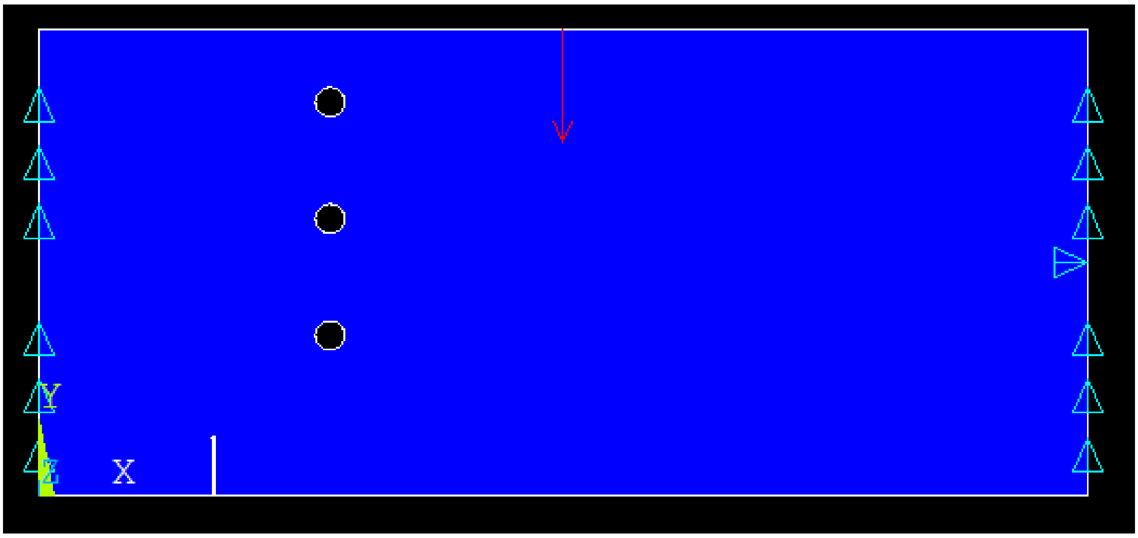

Figure 5.4. Boundary conditions of specimens.

The models have been subjected to a unit load, as the analysis is linear elastic and only the relation between K_I and K_{II} is of interest.

The models are discretized in accordance with section 4.3.1 and the mesh is illustrated on figure 5.5.

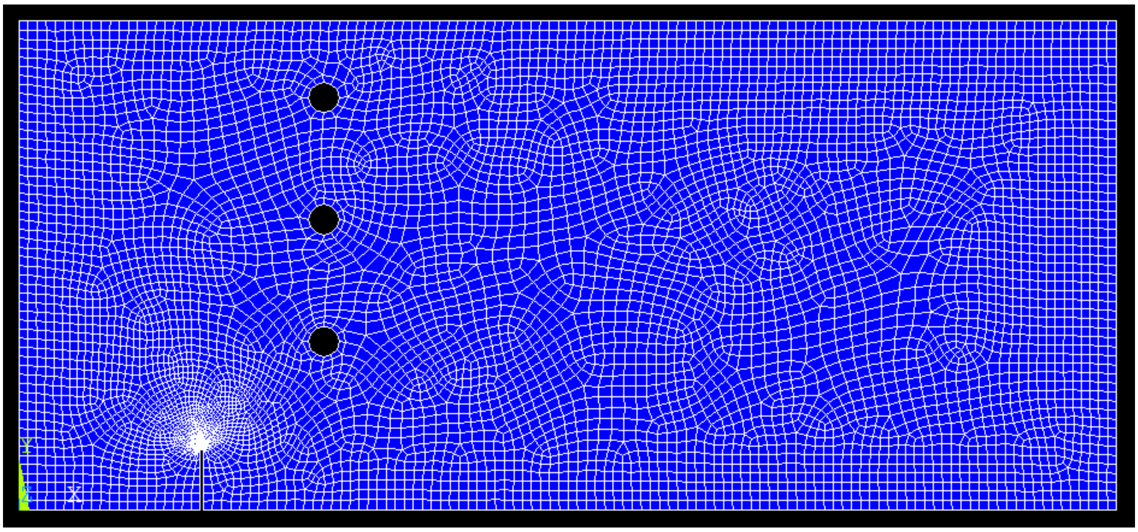

Figure 5.5. Example of mesh.

The crack path has been simulated, with increments of 0.1 in. The results from the simulations are illustrated on figure 5.6, 5.7 and 5.8.

5.2.1 Test results

Specimen 1

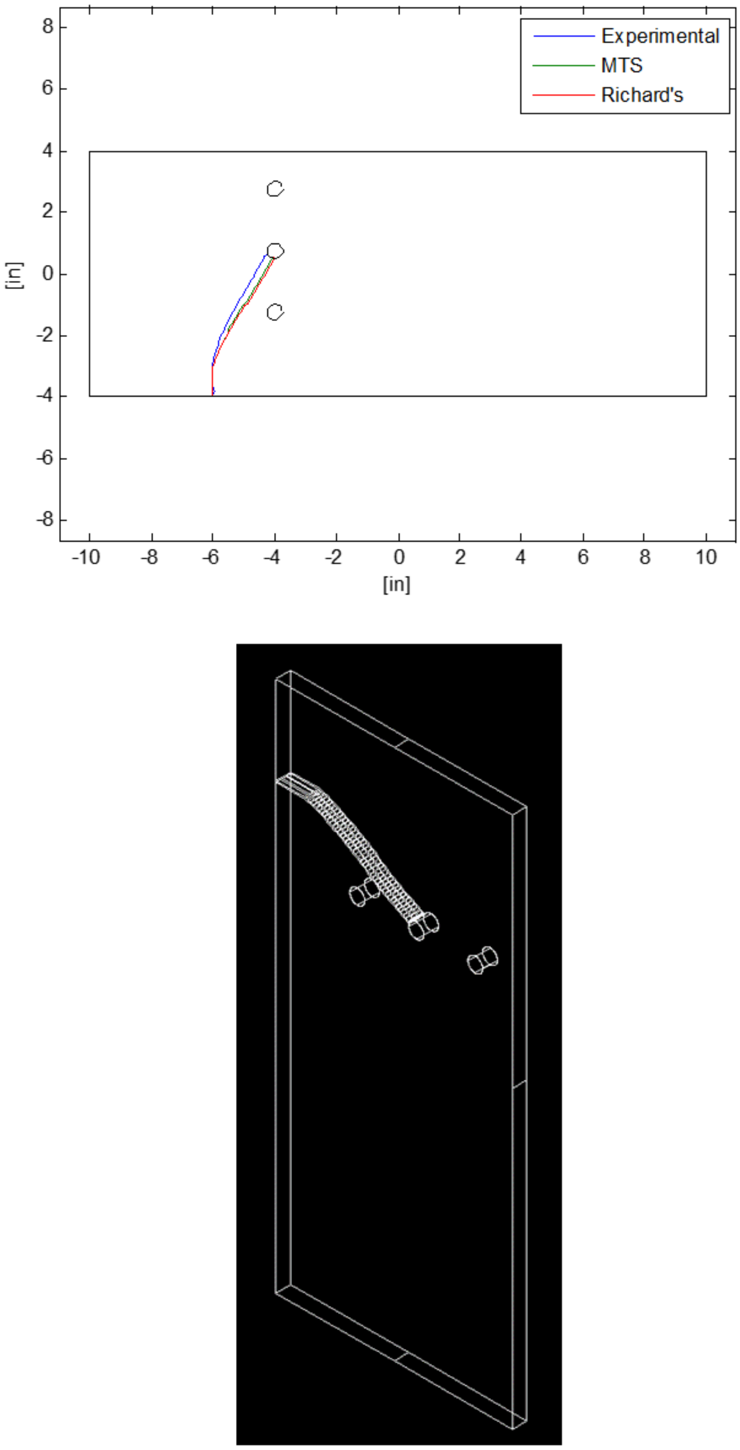

Figure 5.6. Crack path for experimental, MTS and Richard's criterion.

Specimen 2

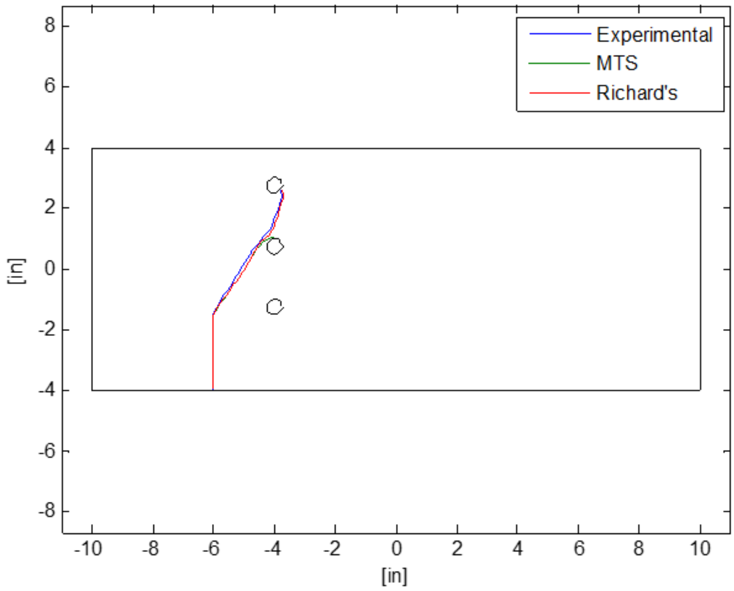

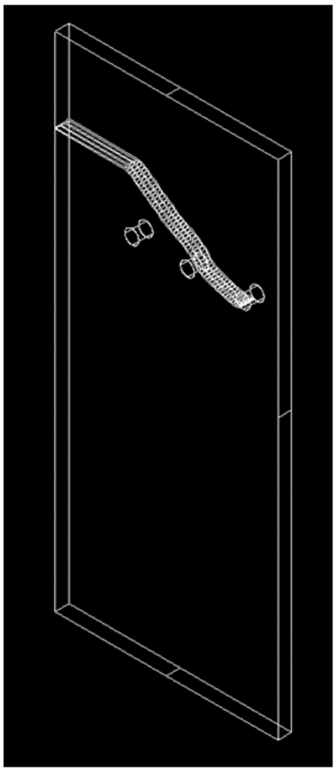

Figure 5.7. Crack path for experimental, MTS and Richard's criterion.

Specimen 3

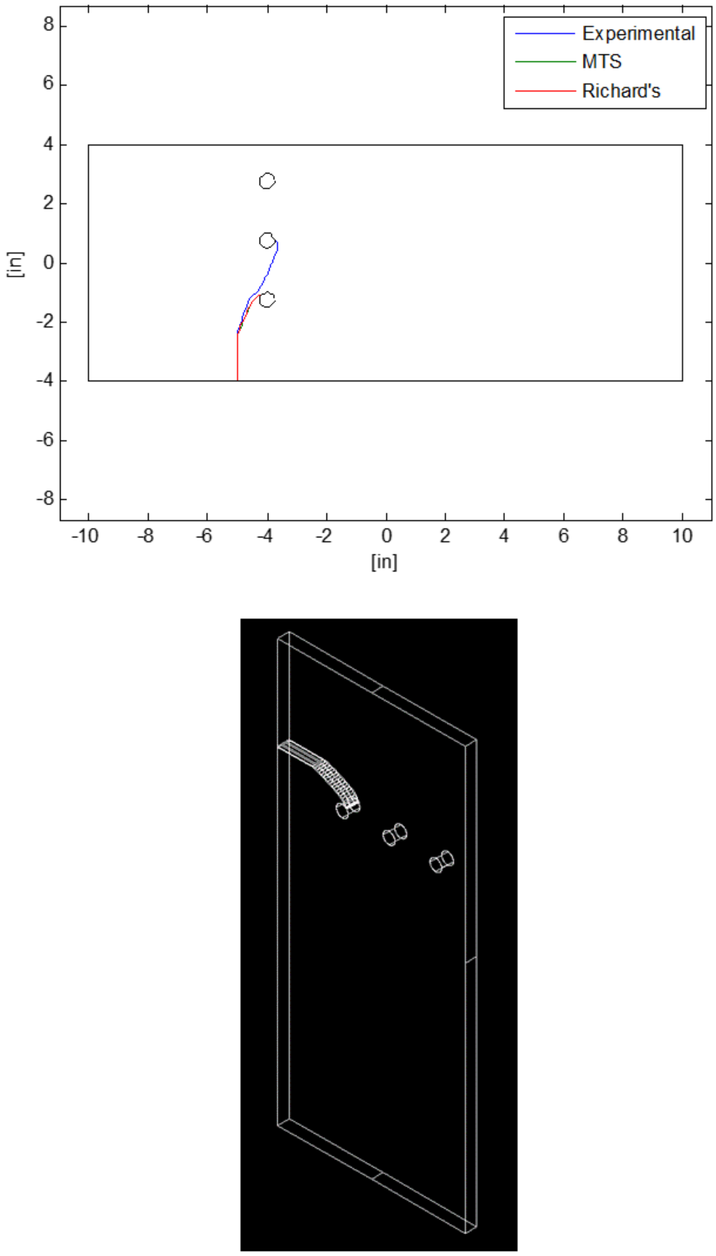

Figure 5.8. Crack path for experimental, MTS and Richard's criterion.

5.2.2 Discussion of results

From the three simulations is it clear that the 2D and 3D analyses are very similar, which implies that MTS and Richard's criterion are practically identical.

It is also evident that the numerical results have a tendency to drift to the right, compared to the experiments. The deviation is the almost the same for the two independent crack propagation criterions and is therefore probably caused by the stress intensities. The deviation is explained by observing the stress intensities on figure 5.9.

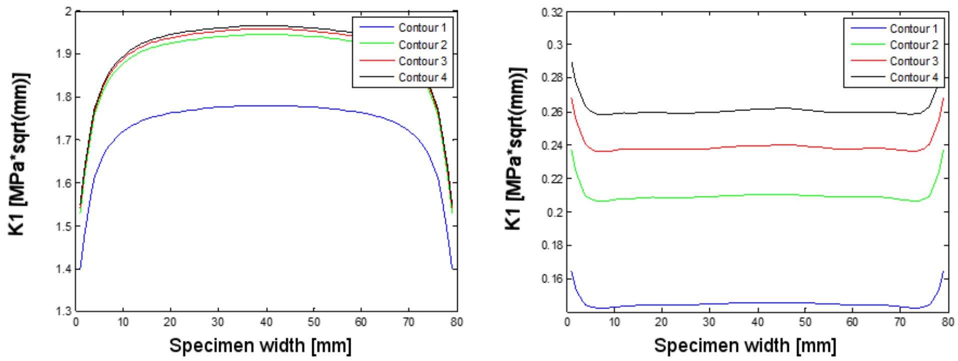

Figure 5.9. K_I(left) and K_{II}(right).

The contours related to K_I are acceptable equal, neglecting contour 1. For $K_{II}$the contours have a relative wide scatter, which indicates lack of accuracy in the numerical prediction of K_{II}.

The accuracy of K_{II} is not satisfactory and further work should be directed towards improving the numerical model or exploration of other methods to determine the stress intensities. Even though it has not been possible to determine K_{II} with satisfactory accuracy, the main purpose of the test has been fulfilled. MTS and Richard's criterion produces almost identical results. MTS is a well-established and trusted criterion and therefore has Richard's criterion been validated by producing almost identical results.

5.3 Case study: Mode I and III

The purpose of this experiment[Omidvar 2013] is to act as an extension of the previous experiment. In the previous experiment Richard's criterion where validated for a mode I+II situation. This experiment will test the validity of Richard's criterion in a mainly mode I+III situation, to further examine the capabilities of Richard's criterion as a crack direction criterion for all three modes.

Richard's criterion will as for the previous experiment, be validated using three different specimens. All three specimen have the same overall dimensions, which are illustrated on figure 5.10.

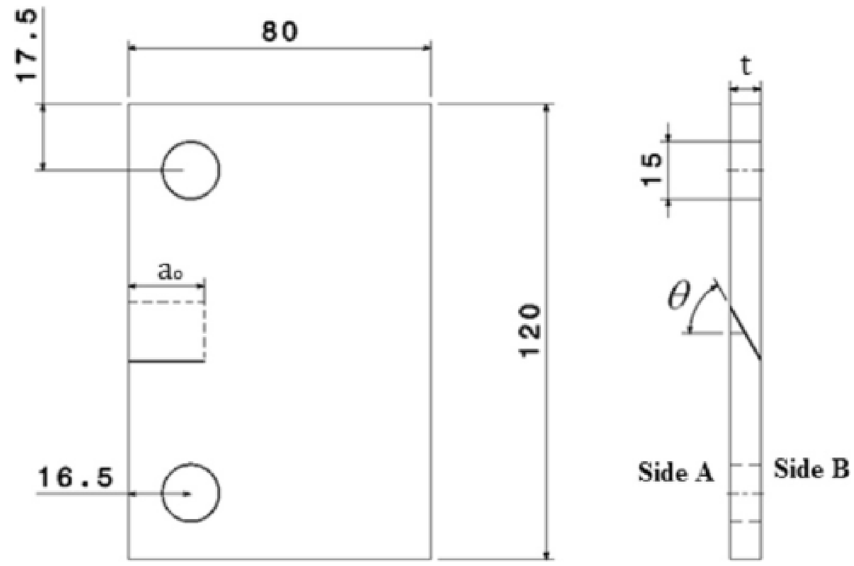

Figure 5.10. Specimen dimensions in mm. t=8.

The variation of the three specimens is the initial slope of the crack front. The tested specimens have slopes of 30°, 45° and 60°, which is illustrated on figure 5.11.

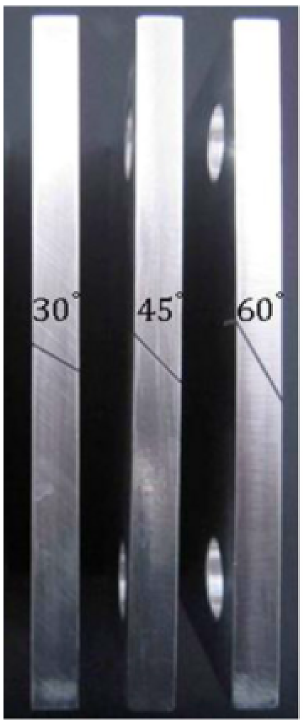

Figure 5.11. Initial twist angles of crack front.

All specimens consists of the aluminum alloy Al-7017. The material data are given in table 5.2.

Material type	Aluminum Al-7017
Young's modulus	$70.0GPa$
Poisson's ratio	0.32
Fracture toughness	$34MPa \cdot \sqrt{m}$

Table 5.2. Material data.

The specimens were, in the experiments , subjected to a cyclic load of 5 Hz with maximum tension of 10 kN and a load ratio of R = 0.2. The load situation causes the crack to grow and the slope of the crack front to diminish, going from a mode I+III situation to a pure mode I situation. This is illustrated on figure 5.12.

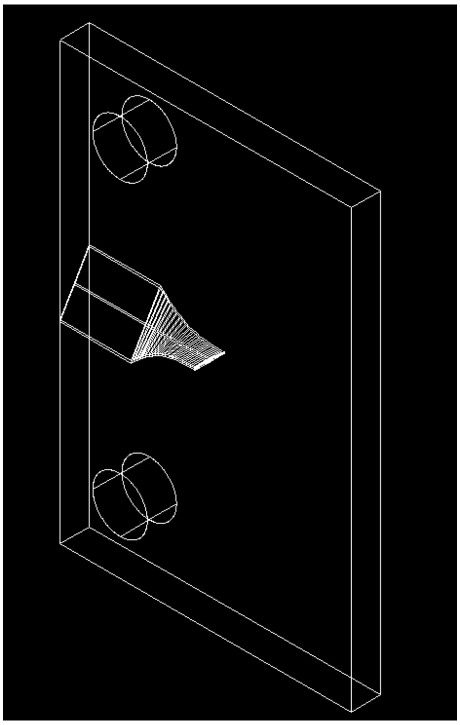

Figure 5.12. Development of crack.

The boundary conditions, in the FEM models, are setup to emulate the boundary conditions of the experiment as close as possible. The boundary conditions are illustrated on figure 5.13.

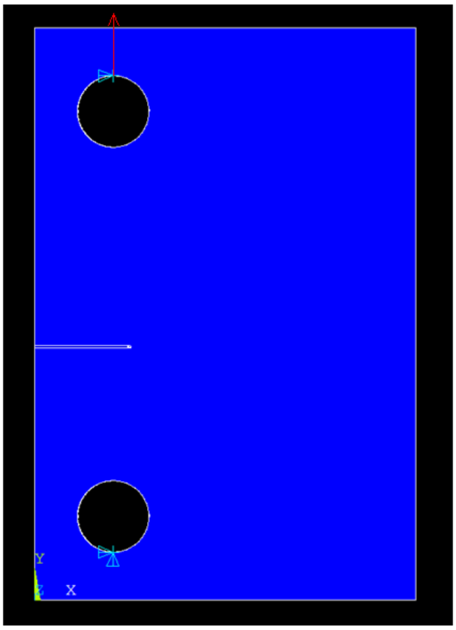

Figure 5.13. Boundary conditions.

The loads are applied as line loads and will inevitably lead stress singularities, but their distance to the crack is large enough for them not to influence the crack propagation.

The FEM models have been discretized in accordance with section 4.3.1. The mesh is illustrated on figure 5.14.

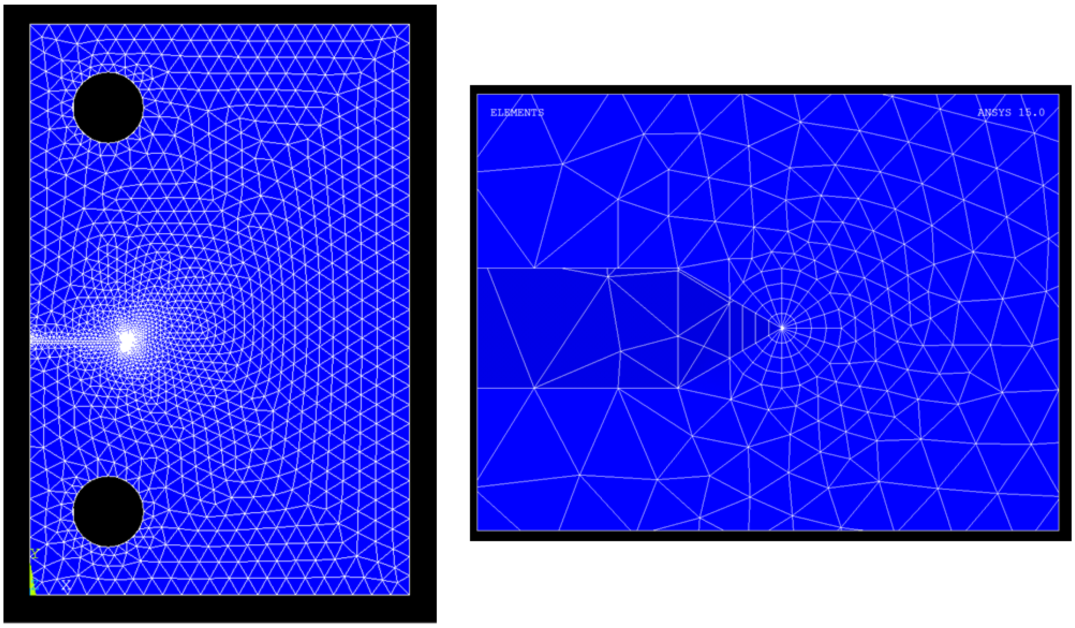

Figure 5.14. Discretized model.

The crack path has been simulated using, increments of 1 mm. The results from the numerical analysis and experiments are illustrated on figure 5.16, 5.17 and 5.18. The experimental results have been obtained by digitizing the crack growth path from pictures similar to figure 5.15.

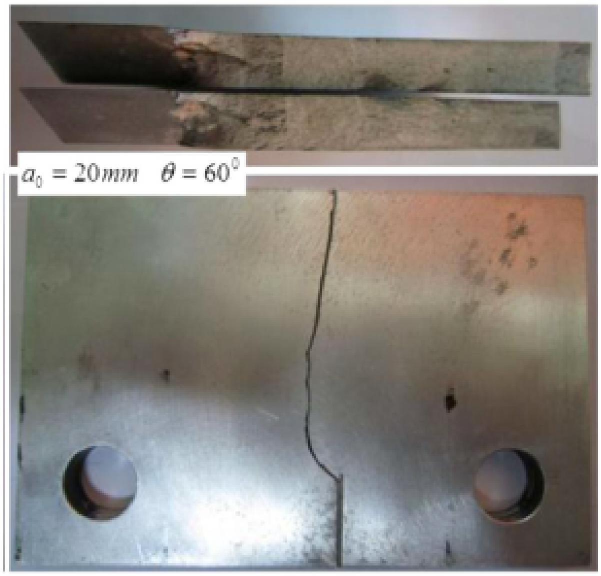

Figure 5.15. Fractured specimen.

When digitizing results from a picture certain sources of error arise. The picture should ideally be 100 % level but from figure 5.15, it is evident that the picture is skewed. Before digitization, the pictures were processed to avoid as much skewing as possible. Direct measurements would have been preferred, but the digitization should be sufficiently accurate, as 100% compliance is not expected between the numerical models and the experiments. The numerical and experimental results in figure 5.16, 5.17 and 5.18 have been overlayed using the initial crack as reference.

Specimen 1

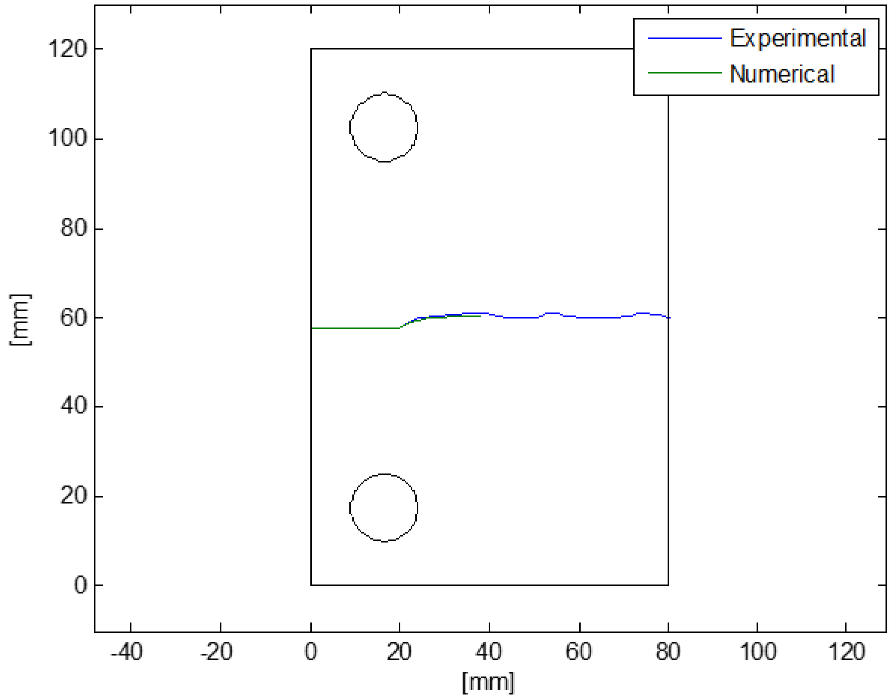

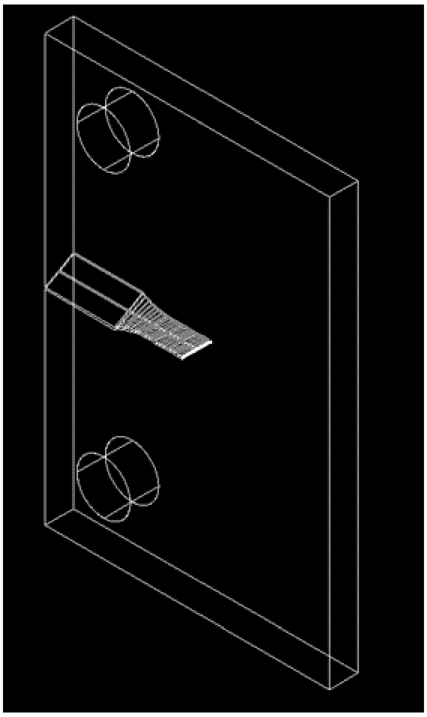

Figure 5.16. Experimental and numerical crack growth path. $\Theta = 30°$.

Specimen 2

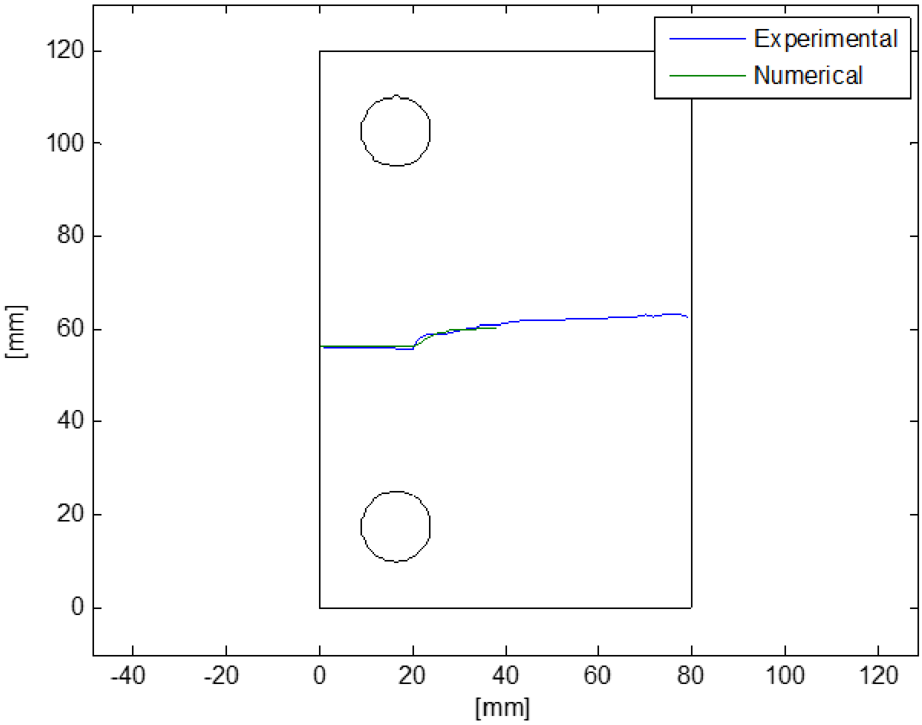

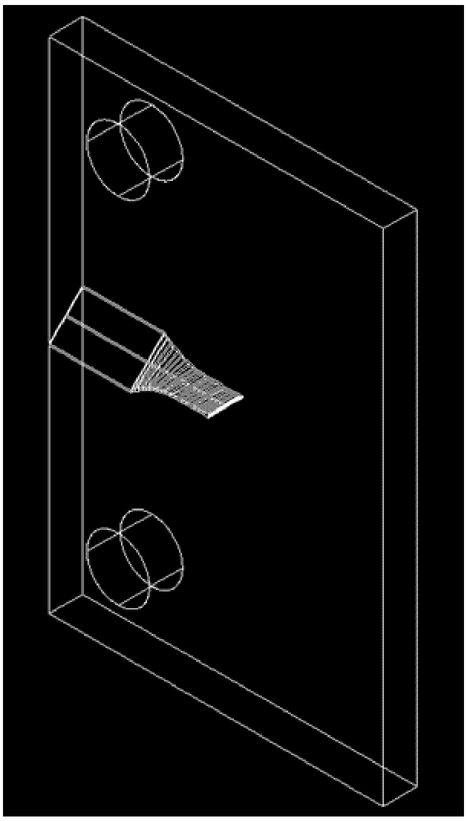

Figure 5.17. Experimental and numerical crack growth path. $\Theta = 45°$.

Specimen 3

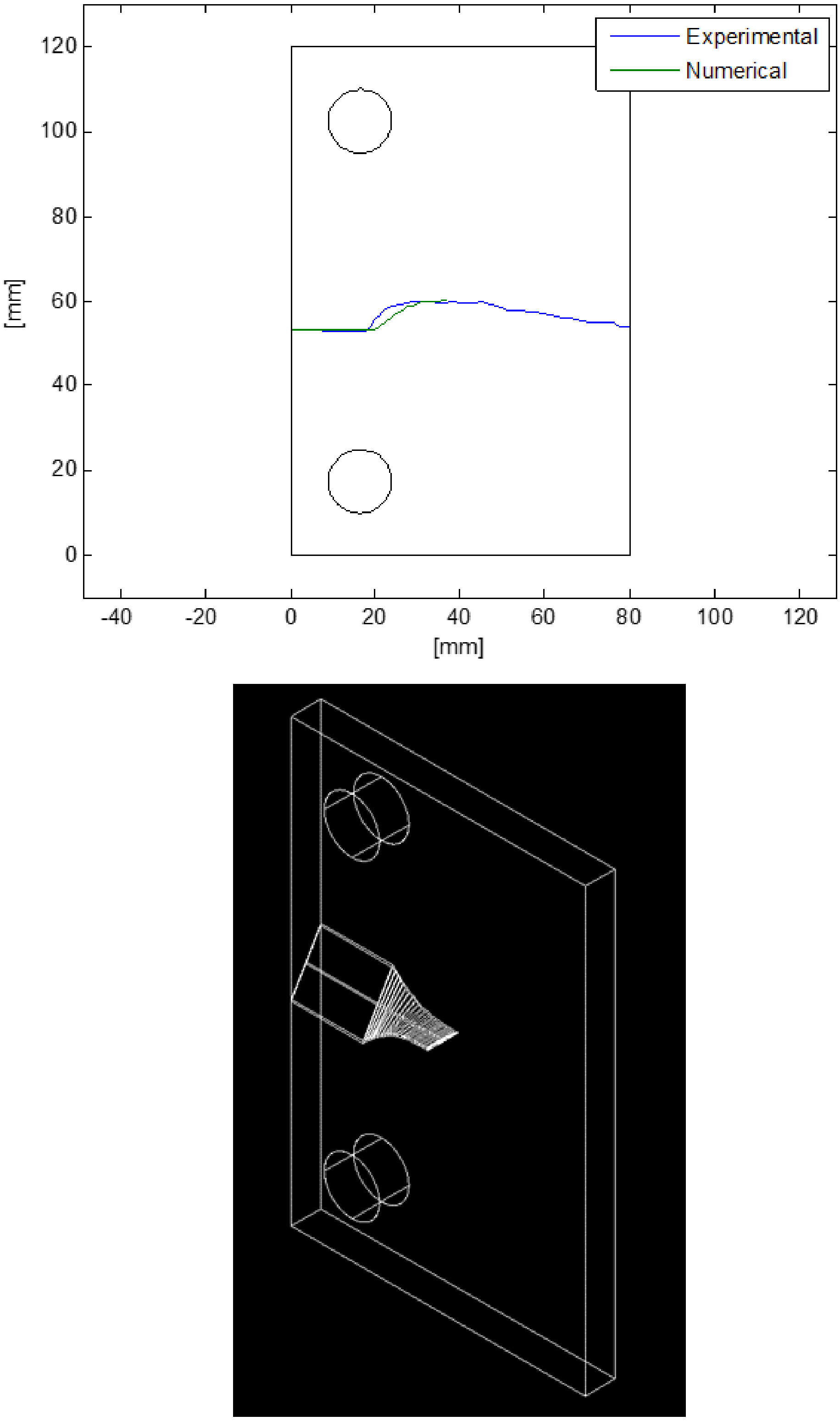

Figure 5.18. Experimental and numerical crack growth path. $\Theta = 60°$.

From figure 5.16, 5.17 and 5.18 is it evident that the numerical and experimental results are very close. The results seem identical, but this can not finally be concluded, because of the sources of error in the digitization process. A clear deviation between experiment and the numerical solution for specimen 3 is noticed. The deviation is caused by an abnormal crack path in the experiment. This is clearly seen in figure 5.15.

The results illustrated on figure 5.16, 5.17 and 5.18 show that Richard's criterion is capable of describing a mode I+III situation.

5.4 Conclusion

From the experiments it can be concluded that Richard's criterion is capable of describing mode I+II and mode I+III situations. A mixed-mode situation where all three modes are dominating have not been tested. The performance of Richard's criterion in the two experiments gives confidence to the use of Richard's criterion in a mode I+II+III situation.

From the first experiment concern about the accuracy of K_{II} have arisen. The source of the inaccuracies have not been determined, but possibly stems from K_{II} calculation in the numerical model.

Further investigation of the accuracy of K_{II} should be carried out and other SIF calculation methods could be tested as well.

Lifetime estimation 6

In this section all the algorithm components are tested in order to make lifetime predictions of the mode I+III test specimens in the previous section. The numerical determined stress intensities and crack propagation direction, and thereby the relation between stress intensities, have been tested in previous sections. Now the combined effect of stress intensity factor magnitude and ratio is tested and evaluated.

6.1 Test case

The SEN specimens, and the experimental results, from the previous section is tested once more. A brief recap of the specimen geometry and material parameters, are specified in figure 6.1 and table 6.1. The specimen is subjected to cyclic loading at $f = 5Hz$ with maximum load $P_{\max} = 10kN$ and load ratio $R = 0.2$.

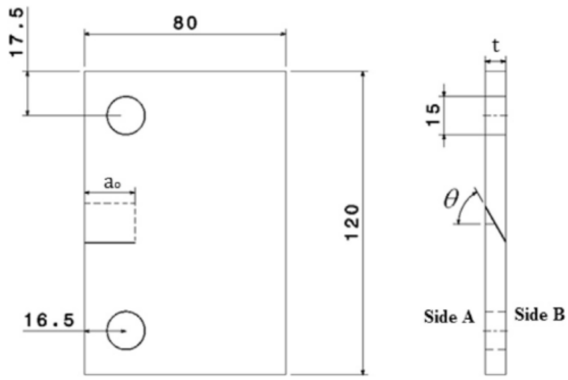

Figure 6.1. Geometry of the tested SEN specimen in mm, where$t = 8mm$, $a_0 = 20mm$ and$\theta = 30°, 45°, 60°$

Material type	Aluminum Al-7017
Young's modulus	$70.0GPa$
Poisson's ratio	0.32
Fracture toughness	$34MPa \cdot \sqrt{m}$
C	$6.8 \cdot 10^{-11}$
n	4

Table 6.1. Material parameters for the tested SEN specimen.

As relative high CPU time is required per every crack growth increment, only simulations of first 20mm crack growth are carried out, for the three different specimens. The simulations are finally compared to the experimental results until 20mm of crack growth.

6.2 Application of crack growth model and mixed mode fracture criterion

The crack growth model of Paris' was chosen, based on the concepts discussed in section 3.4. The justification of choice is outlined below:

- Region II primarily of interest.
  In these tests the crack has already been initiated and therefore is region I irrelevant. The crack will only briefly be in region III and therefore is region II primarily of interest.

- Constant amplitude loading
  The test specimens are subjected to constant amplitude loading, which leads to constant load ratio. Paris' law do not take changing load ratios into account, without updating the material parameters C and n. The test specimens are subjected to constant amplitude loading, which leads to constant load ratio. Paris' law do not take changing load ratios into account, without updating the material parameters C and n.

- Available material parameters
  The material parameters for Paris' law are given in the experimental paper [Omidvar 2013]. By using Paris' law a minimum of variations, between the experiment and this thesis, is ensured.

Crack growth is simulated in incremental steps $da = 1mm$ in which, the actual crack length a and geometrical factor α are assumed to be constant. The number of applied cycles dN is determined by post-processing, using Paris' law as:

$$\frac{da}{dN} = C \cdot \Delta K_{eq}{}^{n} \leftrightarrow dN = \frac{da}{C \cdot \Delta K_{eq}{}^{n}} \tag{6.1}$$

Where:

$\Delta K_{eq} = f(\Delta K_I, \Delta K_{II}, \Delta K_{III})$	Equivalent mode I stress intensity
$da = 1mm$	Number of required cycles to obtain a crack growth of 1mm

The equivalent mode I stress intensity is a combination of mode I, II and III stress intensities, expressing a fracture limit surface as illustrated in figure 6.2.

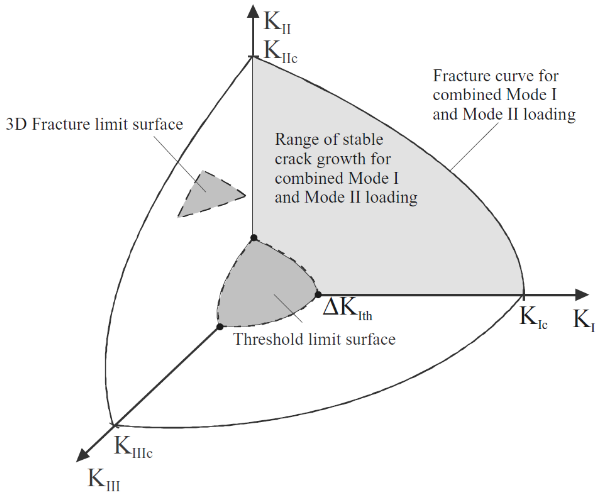

Figure 6.2. Concept of equivalent mode I fracture criterions.

A set of stress intensities positions a point in space at figure 6.2 by using (6.2). Related to crack growth, stable fracture occurs when the point is in between the threshold limit surface and the fracture limit surface. For problems where only one or two modes are activated, the fracture surfaces change to a line or plane respectively.

Several equivalent mode I fracture criterions have been proposed. As explained in **??**, the criterion of Richard is an empirical formulation based on developed approximation functions [H.A. Richard M. Fulland 2005].

The equivalent mode I fracture criterion of Richard is expressed as:

$$\Delta K_{eq} = \frac{\Delta K_I}{2} + \frac{1}{2}\sqrt{\Delta K_I^2 + 4(\alpha_1 \Delta K_{II})^2 + 4(\alpha_2 \Delta K_{III})^2} \tag{6.2}$$

Where:

$\alpha_1 = \frac{K_{Ic}}{K_{IIc}}$ Material parameter depending on mode I+II fracture toughness ratio

$\alpha_2 = \frac{K_{Ic}}{K_{IIIc}}$ Material parameter depending on mode I+III fracture toughness ratio

By using $\alpha_1 = 1.155$ and $\alpha_2 = 1.0$, the criterion of Richard equals the fracture criterion of Schöllmann. The fracture criterion of Schöllmann is based on the assumption of crack growth along the special maximum principal stress $\sigma_{1'}$, defined on figure 6.3.

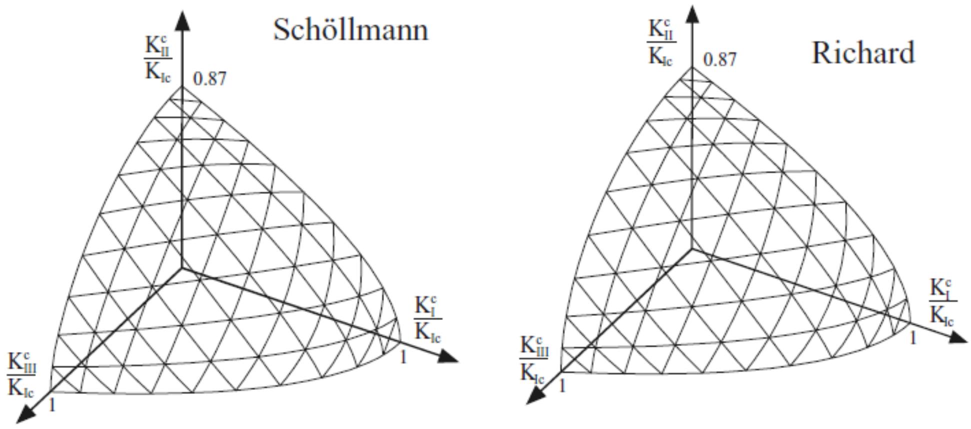

Figure 6.3. Fracture criterions of Schöllmann and Richard, where $\alpha_1 = 1.155$ and $\alpha_2 = 1.0$.

In figure 6.3 the equivalent fracture surface of the criterion of Schöllmann and Richard is illustrated. Due to the solution equivalence, and high numerical applicability, the fracture criterion of Richard is preferred.

6.3 Test results

The results from the experiment and the numerical simulations are illustrated on figure 6.4.

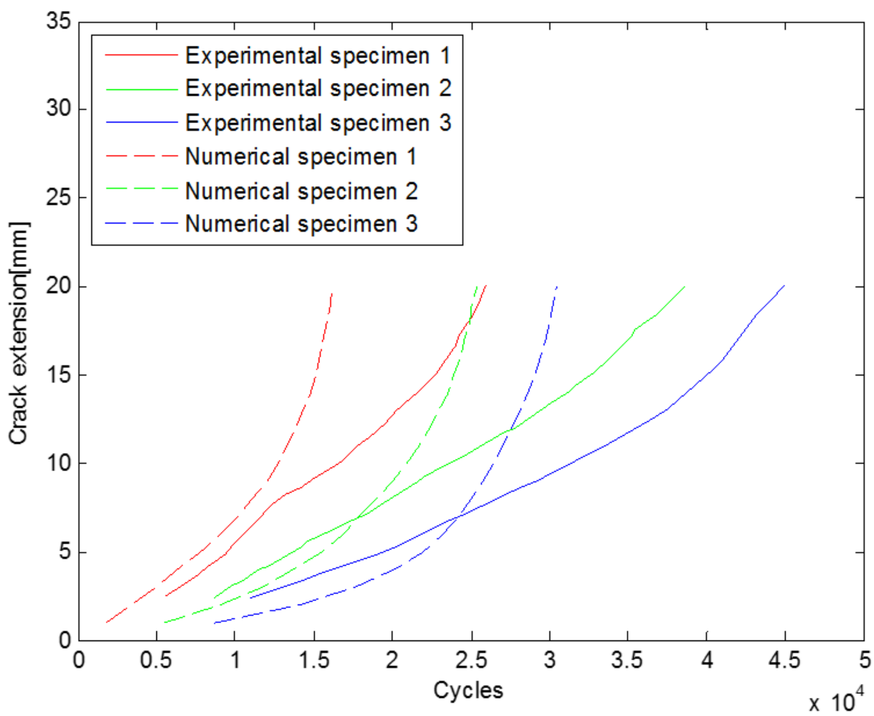

Figure 6.4. Crack growth behavior of the numerical simulations in relation to the experimental results. (Only compared for a crack extension until 20mm)

From figure 6.4 an evident deviation is noticed between the numerical and experimental results. The numerical results show too conservative results with deviations between 32.3-37.8%, as listed in table 6.2.

Specimen	Numerical result [N]	Experimental result [N]	Deviation [%]
1	16,194	26,035	-37.8
2	25,346	38,699	-34.5
3	30,469	45,034	-32.3

Table 6.2. Comparison of numerical and experimental lifetime predictions for 20mm of crack extension.

No clear tendencies in deviation is noticed at the initial crack growth life in figure 6.4, as specimen 1 shows conservative estimation, whereas specimen 2 and 3 show non-conservative estimations.

The crack growth rates are equal for a short amount of cycles, but as the cracks extend, a great difference in crack growth rates are noticed between the numerical and experimental results.

Method	$N_{1,20mm}/N_{3,20mm}$	$N_{2,20mm}/N_{3,20mm}$	$N_{3,20mm}/N_{3,20mm}$
Numerical simulation	0.53	0.83	1.0
Experiment	0.58	0.86	1.0

Table 6.3. Relation between the individual results.

At a crack extension of 20mm the deviations are significant, but a similitude between the numerical and experimental results is noticed. The relations between results at a crack extend of 20mm, normalized by the specimen 3 result of the respective analysis method, is listed in table 6.3.

6.4 Discussion of results

It should be noted that predicted number of cycles may deviate by magnitudes, due to scatter in crack growth life behavior. However, the ratios in table 6.3 are very similar for the numerical and experimental results, indicating a scaling deviation.

In relation to the test results, the topics outlined below, are discussed:

- Magnitude of stress intensities
  A similar crack growth rate is noticed between the numerical and experimental results, in the start of the crack growth, which may confirm a reasonable magnitude of the stress intensities. However, explicit analyses validating the magnitudes of K_{II} and K_{III} have not been carried out. These validations are suggested in further work. Additionally accuracy testing benchmarked against other calculation methods for mixed mode stress intensity factors may lead to optimized accuracy.

- Factory roof phenomenon

  In situations where K_I and K_{III} are dominating, the factory roof phenomenon may occur. A factory roof has been observed, in early stages of the crack growth, for all the specimens [Omidvar 2013]. The factory roofs on specimen 2 are illustrated noticed on figure 6.5.

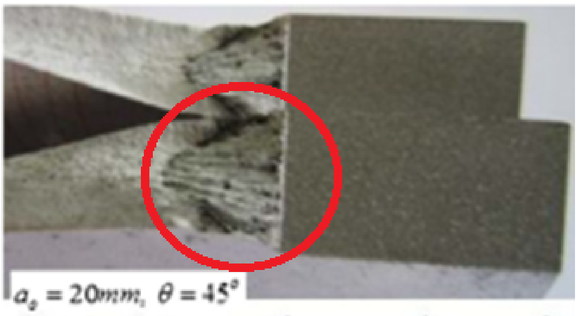

Figure 6.5. Factory roof occurrence on specimen 2.

  According to experiments [Masanori Kikuchi & Suga], the presence of K_{III} lowers the equivalent stress intensity, when factory roofs are present. The equivalent stress intenstiy by Richard [keq], increase with the presence of K_{III} and do not consider the effect of factory roofs. A modified criterion of Richard have been proposed [Masanori Kikuchi & Suga], in order to take the effect of factory roofs into account.

  The implementation of the modified criterion of Richard effect the may effect the crack growth shortly, as the factory roofs are only present in the beginning of the crack growth. The influence of the modified criterion of Richard is positive for specimen 1 and negative for specimen 2 and 3.

- Plasticity induced crack closure

  Because of crack-tip yielding a residual compressive stress is introduced at the crack-tip, when unloading. The load is applied again and has to overcome the residual pressure before the crack surfaces displaces and cause crack growth. Therefore, the residual pressure acts retarding on the crack growth this is called plasticity induced crack closure. If the effect of plasticity induced crack closure is not taken into account, it may lead to conservative numerical results.

  The effect of plasticity induced crack closure increase as the crack grows. Since the effect becomes increasingly larger, which is similar to the result deviations, the crack closure may be origin of the deviations.

7 Discussion

An overall discussion regarding findings within the thesis work. Furthermore, a number of proposed algorithm improvements are highlighted.

7.1 Findings

7.1.1 Numerical accuracy of the mixed mode stress intensity factors

For both of the experimental benchmark tests the mixed mode stress intensities showed a lack of accuracy. The inaccuracy of K_{II} may have caused the inconsistent crack propagation directions in the I+II benchmark test. Also the lifetime prediction results, may improve with more accurate K_I and K_{III} magnitudes.

7.1.2 Assumption of constant crack length a and geometrical factor α

In the lifetime prediction test, the actual crack length a and geometrical factor $\alpha$was assumed constant within every crack growth increment $da = 1mm$. Expressed by the number of cycles post-processed as:

$$\frac{da}{dN} = C \cdot \Delta K_{eq}{}^{n} \leftrightarrow dN = \frac{da}{C \cdot \Delta K_{eq}{}^{n}} \tag{7.1}$$

where $\Delta K_{eq} = f(\Delta K_I, \Delta K_{II}, \Delta K_{III})$ and $\Delta K_i = \sigma_{ii} \cdot \sqrt{\pi a} \cdot \alpha$.

The impact of this assumption has not been explicitly tested and potentially could lead to non-conservative lifetime predictions. However, the tested geometries had initial cracks of several millimeters. Thus, updating the crack length and geometry is expected not to result in any significant increase of the crack growth rates, as the geometry is relatively unchanged and $da \ll a \rightarrow a_i \approx a_{i+1}$.

7.1.3 Effect of plasticity induced crack closure

In the lifetime prediction test, significant differences was noticed between the crack growth rates of the numerical simulation and the benchmark experiment. The effect of plasticity induced crack closure is suspected to be the origin of deviations, based on the similiraties between crack growth deviation and the expected decrease of crack growth rates due to plasticity induced crack closure.

7.1.4 The relation between cast metals and the tested materials

None of the benchmark tests was carried out with cast metals, which is not really what would have been aspected in accordance with the thesis description. However, in order to ensure similitude, experiments with materials showing approximately same material behavior, as cast metals, was used. The used materials was plexiglass and aluminum alloy.

7.2 Proposals for improvements and future/further work

Based on the findings in the thesis work, a number of proposals for further work is highligted and briefly described.

7.2.1 Validation of numerically determined mode II + III stress intensity factors and comparison with other numerical methods to ensure accuracy

An explicit evaluation and validation of K_{II} and K_{III}, in order to confirm or refute their accuracy, and thereby evaluate their impact on the crack growth simulation.

Other numerical methods for determination of the stress intensities may lead to improved accuracy and thereby optimization of the crack growth algorithm.

7.2.2 Plasticity induced crack closure

The effect of plasticity induced crack closure can be implemented by various proposed methods. The crack growth model NASGRO, may include plasticity induced crack closure, by a crack opening function by Newman.

Also numerical methods have been proposed with acceptable results [Maitireyimu 2009]. By means of elastic-plastic analyses the effect of plasticity induced crack closure effect can be approximated.

The concept of both methods is to define an effective stress intensity for each mode, e.g. expressed as:

$$\Delta K_{i,eff} = U_i \Delta K_i \tag{7.2}$$

where the plasticity induced crack closure effect U is defined as the fraction of relative displacement between two adjacent crack face points. The adjacent displacements may be found as e.g. nodal displacements, making it very applicable to the already made computational framework. The accuracy of the crack closure effect should be tested and validated after implementation.

7.2.3 Factory roof effects by use of the modified criterion of Richard

The effect of factory roofs is easily implemented by using the modified criterion of Richard in [Masanori Kikuchi & Suga]. The modified criterion of Richard is, in 3D, expressed as:

$$\Delta K_{eq(I,II,III)} = \frac{\Delta K_{eq(I,III)}}{2} + \frac{1}{2}\sqrt{\Delta K_{eq(I,III)}{}^2 + 4(1.155\Delta K_{II})^2} \tag{7.3}$$

Where:

$$\Delta K_{eq(I,III)} = \frac{\sqrt{\left(\Delta K_I - \sqrt{2}|\,\Delta K_{III}|\right)^2 + \Delta K_I{}^2}}{\sqrt{2}}$$

As noticed, the expression for the equivalent mode I fracture criterion is more lengthy, but still very applicable in numerical solutions. The robustness and applicability of the modified criterion of Richard should be tested and validated after implementation.

7.2.4 Variable amplitude loading and load proportionality

By means of cycle post-processed cycle counting, tests of variable amplitude loading needs to be carried out. Instead of just isolating dN in (7.1) each individual cycle should be considered, and weightedly influence the direction of propagation. Based on cyclic equivalent mode I stress intensities $\Delta K_{eq,i}$and load ratios R_i, a variable amplitude crack growth increment da could be determined by summarizing cyclic crack growth increments until the maximum allowable value:

$$da = \sum_{i=1}^{n} a_i = \sum_{i=1}^{n} dN_i \cdot f\left(\Delta K_{eq,i}, R_i\right) \tag{7.4}$$

and crack propagation directions as:

$$d\varphi = \sum_{i}^{n} d\varphi_i = \sum_{i=1}^{n} f(\Delta K_{I,i}, \Delta K_{II,i}, \Delta K_{III,i}) \tag{7.5}$$

$$d\psi = \sum_{i}^{n} d\psi_i = \sum_{i=1}^{n} f(\Delta K_{I,i}, \Delta K_{II,i}, \Delta K_{III,i}) \tag{7.6}$$

A Matlab code was generated in order to evaluate these cyclic values, but due to time constraints, the code has not been tested yet.

Attention should be paid to the effect of non-proportional loading, which may influence the results of variable amplitude loading[P. Zerres 2014]. In relation to non-proportional loading, shortcomings of equivalent mode I criterions have been found.

7.2.5 Additional testing of various three-dimensional crack shapes

As the numerical is improved, a further validation is suggested. This validation should include other 3D cracks with curved crack fronts, e.g. surface cracks and embedded cracks.

7.2.6 Automatic identification of maximum allowed crack increment

An automaticly determined maximum crack growth increment, still leading to acceptable accuracy, would optimize the crack growth simulations in relation to CPU time. The simulation time of the lifetime prediction tests was around 5 hours per 20mm of crack extension.

7.2.7 Experiments of cast metals and find material parameters

As mentioned, the available experimental data for cast metals are rather poor. Hence, fracture toughness testing of cast metals and experimental crack growth is of major interest in computational crack growth simulations of cast metals.

8 Conclusion

Great effort was spend automating a fatigue crack growth algorithm, which was successfully obtained by the developed computational framework in Matlab and Ansys APDL. Implemented crack growth models, crack propagation direction and fracture criterions were individually tested, and evaluated against relevant case studies. Numerical solutions was obtained, by successful implementation of the aforementioned fracture mechanics. The numerical simulation led to promising, but also sometimes, deviating results in comparison to the experimental case studies. Based on the deviations a number of tests and improvements for further work have been proposed.

A number of concluding remarks, in relation to the outlined thesis objectives, are highlighted below:

- Considerations regarding acceptable casting defects, and thereby initial crack definitions in casted components/members, have been presented in section 2.1.
- Important theoretical aspects of linear-elastic fracture mechanics was presented and discussed in 3.1
- The influence of mean stress level was tested in section **??** by comparison of Paris' law, Forman equation and NASGRO. Significant influence in crack growth rates was noticed in region I and III, but only moderate in region II.
- Mixed mode stress intensity factors were calculated numerically by a domain integral method, specifically the interaction integral, in section 4.
- The magnitude K_I was tested and evaluated against various analytical solutions in 4. The accuracy of K_I was acceptable in relation to the analytical solutions.
- Based on K_I and K_{II} ratios, the similarity between maximum tangential stress criterion and the criterion of Richard was proven in 5.1.
- Deviations between numerical and experimental crack propagation directions was noticed in the mode I+II test, in section 5.1. These may have been caused by inaccuracy of the numerically calculated K_{II} values.
- Acceptable crack propagation directions was found in the mode I+III test in section 5.1., as the numerical and experimental crack propagation directions were very similar.

- Incremental fatigue crack growth was tested in section 6, applying the crack growth model of Paris' along with equivalent mode I and crack propagation direction of Richard. A similarity between conservative numerical deviation in crack growth rates and the retarding effect of plasticity induced crack closure was noticed. Hence, this may be origin of deviations between numerical and experimental fatigue crack growth predictions.

- Based on findings throughout the thesis work, several improvements have been suggested for further work in section 7. In addition to these, the performance of the computational framework may also be highly optimized.

Bibliography

T. Anderson (2005). Fracture Mechanics. Taylor and Francis.

ASTM (????). 'E1290-08' .

P. H. H. S. G. P. H. Biermann (2007). 'Load history effects in ductile cast iron for wind turbine components'. International Journal of Fatigue **2**9.

A. F. Bower (2009). Applied mechanics of solids. CRC Press.

DNV-RP-C203 (????). 'DNV-RP-C203 - Fatigue design of offshore steel structures' .

L. W. H. J. H. Dong & J. Li (2013). 'Balance Fatigue Design of Cast Steel Nodes in Tubular Steel Structures'. The Scientific World Journal **2**013.

R. G. V. E.Kearney & R. M. Engle (1967). 'Numerical Analysis of Crack Propagation in Cyclic-LoadeStructures'. Trans. ASME, J.BasicEng. **8**9:459.

W. Elber (1977). 'Fatigue crack closure under cyclic tension'. Engineering Fracture Mechancis .

G. S. F. Erdogan (1963). 'On the crack extension in plates under plane loading and transverse shear'. J. Basic Eng p. 519.

J. FERNANDO C. M. MENANDRO, E. T. MOYER & H. LIEBOWITZ (????) .

B. F.M. & Stone (1966). 'The Crack Opening Displacement Approach to Fracture Mechanics in Yielding Materials.'. Journal of Strain Analysis **1**.

F. R. G. & M. S. R. (1992). 'Behavior of Surface and Corner Cracks Subjected to Tensile and Bending Loads in Ti-6Al-4V Alloy'. Twentysecond Symposium **1**:519.

M. S. H.A. Richard M. Fulland (2005). 'Theoretical crack path prediction'. Fatigue Fract Engng Mater Struct **2**8:3–12.

A. International (2009). Casting Design and Performance.

I. A. G. M (1990). 'Probabilistic fracture mechanics: a validation of predictive capability' .

C. V. C. J. E. Maahn (2009). Metallurgi for ingeniÃ¸rer. Polyteknisk forlag.

M. Maitireyimu (2009). 'Comoarison of Experimental and Numerically Simulated Fatigue Crack Propagtion'. Journal of Solid Mechanics and Materials Engineering **3**.

Y. W. Masanori Kikuchi & K. Suga (????) .

P. M.P.Gomez & W. E.Anderson (1961). 'A Rational Analytical Theory of Fatigue'. Trend Eng. **1**3:9.

NASA (1959). 'THE RATE O F FATIGUE-CRACK PROPAGATION FOR TWO ALUMINUM ALLOYS UNDER COMPLETELY REVERSED LOADING' .

R. S. N. Omidvar (2013). 'Fatigue crack growth under mixed mode I + III loading'. Marine Structures **3**4:1–15.

M. V. P. Zerres (2014). 'Review of fatigue crack growth under non-proportional mixed-mode Loading'. International Journal of Fatigue **5**8.

S. Suresh & R. Ritchie (1984). 'Propagation of short fatigue cracks'. International metallurgical reviews **2**9.

M. Williams (1956). 'On the stress distribution at the base of a stationary crack'. Jour. applied mechanics .

Appendix A

A.1 Analytical solutions for stress intensity factors

This appendix serves the purpose of presenting analytical crack problem solutions used for validation of the numerical models proposed in the algorithm.

Flaws arising from casting can be considered equal to a crack. Hence, the expression â€œcrackâ€ is consistently used in the following.

A.1.1 Stress intensity - two-dimensional cracks

A general formulation of the stress intensity factor, under plane conditions, is expressed as:

$$K = \sigma \cdot \sqrt{\pi a} \cdot \alpha \tag{A.1}$$

Where:

σ	Nominal stress
a	Crack length
α	Geometrical factor

A modification of the geometrical factor adjusts the stress intensity factor to fit for any plane problem with an equally sized crack which is loaded similar. This is illustrated below for two plane crack problems.

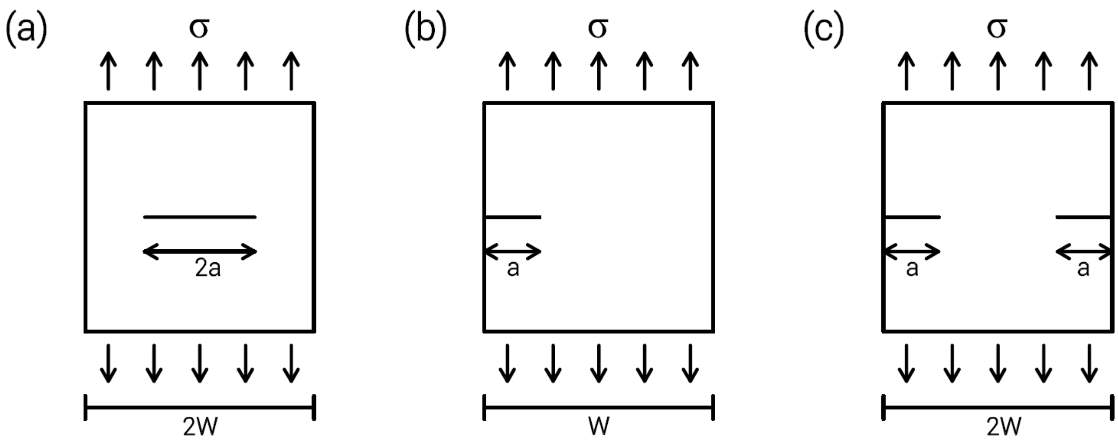

Figure A.1. (a) Two dimensional crack problems; center cracked plate, (b) single through edge crack and (c) double edge cracked plate.

The analytical solutions for the two dimensional crack problems, illustrated in figure **??**, are expressed as:

$$K_I = \sigma \cdot \sqrt{\pi a} \cdot \frac{1 - a/2W + 0.326a^2/W^2}{\sqrt{1 - a/W}} \text{ for all } \frac{a}{W} \tag{A.2}$$

$$K_I = \sigma \cdot \sqrt{\pi a} \cdot \left(1.12 - 0.23\frac{a}{W} + 10.6\frac{a^2}{W^2} - 21.7\frac{a^3}{W^3} + 30.4\frac{a^4}{W^4}\right) \text{ for } \frac{a}{W} < 0.7 \tag{A.3}$$

$$K_I = \sigma \cdot \sqrt{\pi a} \cdot \frac{1.12 - 0.61a/W + 0.13a^3/W^3}{\sqrt{1 - a/W}} \text{ for all } \frac{a}{W} \tag{A.4}$$

The crack problems above, are considered to be plane problems and geometrical variation in the depth is not accounted for. Considering reality more complex geometry exists and therefore three-dimensional formulation of the cracks has to be considered in order to capture important fracture mechanical aspects.

A.1.2 Stress intensity - three-dimensional cracks

A.1.2.1 Embedded cracks

Cracks are now considered in the three-dimensional space. An exact solution for an embedded penny-shape crack, as seen in figure **??**a, was developed by Sneddon.

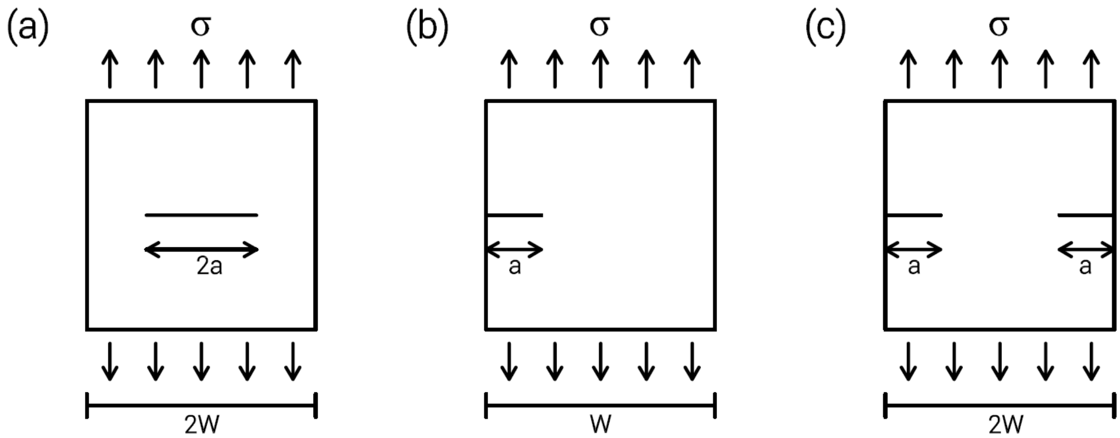

Figure A.2. Embedded cracks in an infinite body; (a) circular crack (b) elliptical crack (c) angular coordinates.

Hence, for practical purpose, Irwin introduced a solution for an embedded elliptical crack as seen in figure **??**.b. Irwin's solution for a small embedded elliptical crack compared to plate dimensions and$a \leq c$, is expressed as:

$$K_I = \sigma \cdot \sqrt{\frac{\pi a}{Q}} \cdot f(\phi) \tag{A.5}$$

Where:

K_I	Mode I stress intensity factor
$Q = 1 + 1.464\left(\frac{a}{c}\right)^{1.65}$	Flaw shape parameter
$f_\phi = \left(\sin^2(\phi) + \left(\frac{a}{c}\right)^2 \cdot \cos^2(\phi)\right)^{1/4}$	Angular function of location
a	Major crack radius
ϕ	Parametric angle
$Q = 1 + 1.464\left(\frac{a}{c}\right)^{1.65}$	Flaw shape parameter

Because the stress intensity assumes the crack small comparatively to plate dimensions, boundary corrections for external boundaries is negligible. Therefore, another solution is needed in order to approximate stress intensity factors for cracks near the surface.

A.1.2.2 Surface cracks

Newman and Raju introduced an solution for a semi-elliptical surface cracks in a finite plate under tension and bending loads.

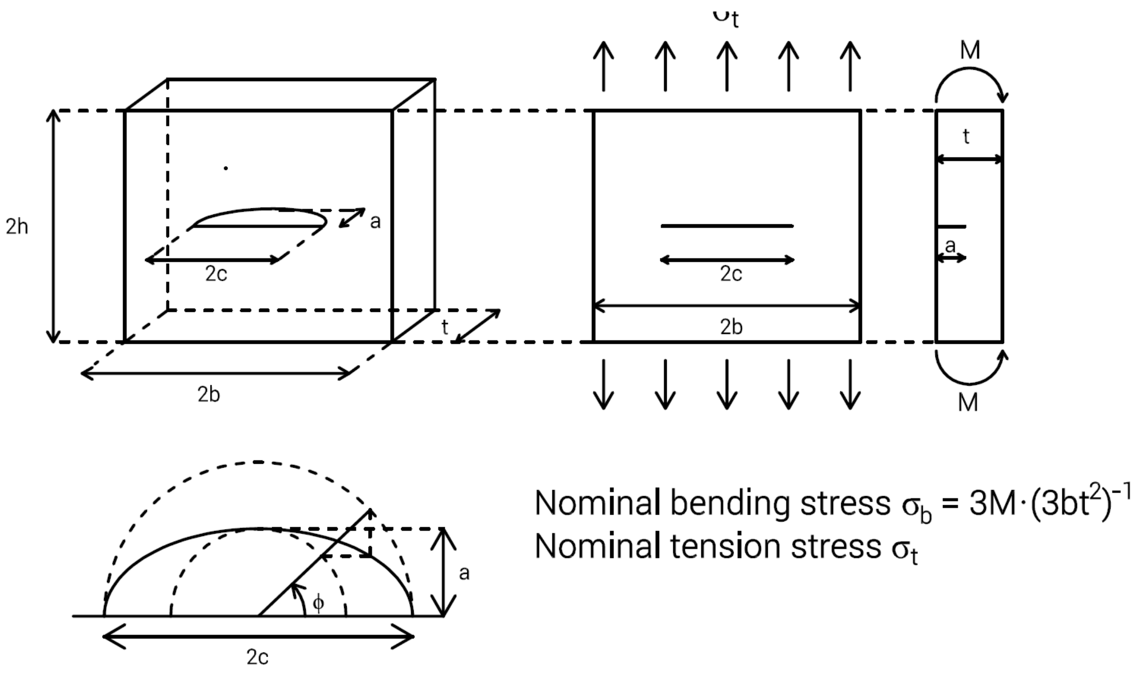

Figure A.3. Loading and geometry definitions for a semi-elliptical surface crack in a plate. $S_t$and $S_b$corresponds to remote uniform tension stress and outer fiber bending stress respectively.

The empirical equation proposed by Newman and Raju for stress intensity factor K_I is an extended version of Irwin. Newman and Raju proposed the following solution:

$$K_I = (\sigma_t + H \cdot \sigma_b) \cdot \sqrt{\frac{\pi a}{Q}} \cdot F \tag{A.6}$$

for crack shape$0 < \frac{a}{c} \leq 1$, crack size $0 \leq \frac{a}{t} < 1$, plate width$\frac{c}{b} < 0.5$ and $0 \leq \phi \leq \pi$.

Where:

$F = \left[M_1 + M_2\left(\frac{a}{t}\right)^2 + M_3\left(\frac{a}{t}\right)^4\right] \cdot f_\phi \cdot g \cdot f_w$ Boundary correction factor
$H = H_1 + (H_2 - H_1) \cdot \sin^p(\phi)$ Parametric angle
$Q = 1 + 1.464\left(\frac{a}{c}\right)^{1.65}$ Additional boundary correction factor for bending

The extended solution includes bending stress S_b and also boundary correction factors. The boundary correction factor for tension is equal to F expressed by the additional parameters: $M_1 = 1.13 - 0.09\left(\frac{a}{c}\right)$ $M_2 = -0.54 + \frac{0.89}{0.2+\frac{a}{c}}$ $M_3 = 0.5 - \frac{1}{0.65+\frac{a}{c}} + 14 \cdot \left(1 - \frac{a}{c}\right)^{24}$

$$g = 1 + \left[0.1 + 0.35\left(\frac{a}{t}\right)^2\right] \cdot (1 - \sin(\phi))^2$$

$f_w = \left[\sec\left(\frac{\pi c}{2b}\sqrt{\frac{a}{t}}\right)\right]^{1/2}$ Finite width correction factor

The boundary correction factor for bending is equal to $H \cdot F$ for which the additional parameters of H are expressed as: $p = 0.2 + \frac{a}{c} + 0.6\frac{a}{t}$

$$H_1 = 1 - 0.34\frac{a}{t} - 0.11\frac{a}{c}\left(\frac{a}{t}\right)$$

$$H_2 = 1 + G_1\left(\frac{a}{t}\right) + G_2\left(\frac{a}{t}\right)^2$$

$$G_1 = -1.22 - 0.12\frac{a}{c}$$

$$G_2 = 0.55 - 1.05\left(\frac{a}{c}\right)^{3/4} + 0.47\left(\frac{a}{c}\right)^{2/1}$$

For a given three-dimensional case, the stress intensity factors will vary with

$$\phi$$

and the maximum stress intensity factor is located at $\phi = 90°$ and minimum at $\phi = \begin{cases} 0° \\ 180° \end{cases}$.

The solution of surface cracks] provides acceptable solutions for cylinders with large radius to thickness ratios.